

TECHNISCHE
UNIVERSITÄT
DRESDEN

Holographic QCD Phase Diagram and Entanglement Entropy

Masterarbeit
zur Erlangung des Hochschulgrades
Master of Science
im Master-Studiengang Physik

vorgelegt von

JOHANNES KNAUTE
geboren am 22.11.1991 in Dresden

Institut für Theoretische Physik
Fakultät Physik
Bereich Mathematik und Naturwissenschaften
Technische Universität Dresden
2017

Eingereicht am 15. Dezember 2017

1. Gutachter: Prof. Dr. Burkhard Kämpfer
2. Gutachter: Prof. Dr. Dominik Stöckinger

Abstract

We study a holographic Einstein-Maxwell-dilaton model, which is adjusted to lattice QCD data for 2+1 flavors and physical quark masses for the equation of state and quark number susceptibilities at zero baryo-chemical potential, to explore the resulting phase diagram over the temperature-chemical potential plane. A first-order phase transition sets in at a temperature of about 112 MeV and a baryo-chemical potential of 612 MeV. We estimate the accuracy of the critical point position in the order of approximately 5-8 % by taking lattice uncertainties into account. The phase transition is characterized by analyzing the critical pressure and the behavior of isentropes. Furthermore, we calculate the holographic entanglement entropy for this model and compare its phase diagram to that of the thermodynamic entropy. We find an agreement in the vicinity of the critical point. Thus, the holographic entanglement entropy qualifies us to characterize different phase structures. The scaling behavior near the critical point is analyzed through the calculation of critical exponents.

Kurzdarstellung

Im Rahmen dieser Arbeit untersuchen wir ein holographisches Einstein-Maxwell-Dilaton Modell, welches an die Daten der 2+1 Flavor-Gittereichtheorie mit physikalischen Quarkmassen bezüglich der Zustandsgleichung und Suszeptibilitäten bei verschwindendem chemischen potential adjustiert ist. Das resultierende Phasendiagramm wird in der Temperatur-chemisches Potential Ebene analysiert. Ein Phasenübergang erster Ordnung setzt bei einer Temperatur von etwa 112 MeV und einem chemischen Potential von 612 MeV ein. Die Genauigkeit dieses Ergebnisses für den kritischen Punkt wird unter Berücksichtigung von Unsicherheiten der Gitterdaten in der Größenordnung von 5-8 % abgeschätzt. Der Phasenübergang wird durch Beschreibung des kritischen Druckes und dem Verhalten der Isentropen näher charakterisiert. Im Weiteren berechnen wir die holographische Verschränkungsentropie für dieses Modell und vergleichen das resultierende Phasendiagramm mit dem der thermodynamischen Entropie. Es stellt sich eine gute Übereinstimmung in der Nähe des kritischen Punktes heraus. Die holographisch berechnete Verschränkungsentropie kann daher zur Charakterisierung der verschiedenen Phasenstrukturen dienen. Das Skalenverhalten in der Nähe des kritischen Punktes wird durch Berechnung von kritischen Exponenten untersucht.

Publications¹ and talks

This thesis is based on the results and discussions from the following papers:

- [1] J. Knaute, R. Yaresko and B. Kämpfer:
Holographic QCD phase diagram with critical point from Einstein-Maxwell-dilaton dynamics,
arXiv:1702.06731 [hep-ph] (2017)

- [2] J. Knaute and B. Kämpfer:
Holographic entanglement entropy in the QCD phase diagram with a critical point,
Physical Review D 96, 106003 (2017)

Earlier work, which provided some background for this thesis, is published in:

- [3] R. Yaresko, J. Knaute and B. Kämpfer:
Cross-over versus first-order phase transition in holographic gravity-single-dilaton models of QCD thermodynamics,
European Physical Journal C 75, 295 (2015)

Results from this thesis have also been presented in the following talks:

- “Holographic QCD Phase Diagrams and Entanglement Entropy”, talk given at the 57th Cracow School of Theoretical Physics on Entanglement and Dynamics, Zakopane, Poland, June 13-21 2017

- “Entanglement Entropy in a holographic model for the QCD critical point”, talk given at the DESY Theory Workshop on fundamental physics in the cosmos, Hamburg, Germany, September 26-29 2017

¹On the occasion of a one-year exchange study at Princeton University during my master studies, a further paper [S. S. Gubser, J. Knaute, S. Parikh, A. Samberg and P. Witaszczyk: *p-Adic AdS/CFT*, Communications in Mathematical Physics 352, 1019 (2017)] was coauthored, whose content is not subject of this thesis.

Contents

| | | |
|----------|---|-----------|
| 1 | Introduction | 1 |
| 2 | Quantum Chromodynamics and heavy-ion collisions | 5 |
| 2.1 | Lagrangian formulation and β function | 5 |
| 2.2 | Lattice gauge theory and thermodynamics | 7 |
| 2.3 | The QCD phase diagram | 9 |
| 2.4 | Heavy-ion collisions | 11 |
| 3 | The gauge/gravity duality | 15 |
| 3.1 | Anti-de Sitter spacetimes | 15 |
| 3.2 | Aspects of conformal field theories | 17 |
| 3.3 | The AdS/CFT correspondence | 19 |
| 3.4 | Elements of the gauge/gravity duality | 22 |
| 4 | Holographic model | 25 |
| 4.1 | Review of the holographic EMd model | 25 |
| 4.2 | Adjustment to lattice QCD data at $\mu = 0$ | 29 |
| 4.3 | Holographic QCD phase diagrams | 33 |
| 5 | Entanglement Entropy | 41 |
| 5.1 | General aspects of entanglement entropy | 41 |
| 5.2 | Holographic entanglement entropy in the EMd model | 44 |
| 5.3 | Phase diagram of holographic entanglement entropy | 47 |
| 5.4 | Critical behavior | 50 |
| 6 | Summary and Outlook | 53 |
| A | Details of the dilaton potential | 57 |
| | Bibliography | 61 |

1 Introduction

According to our current understanding of physics, there are four fundamental forces in nature. The electroweak and strong forces are responsible for microscopic particle interactions, whereas gravitation determines the motion and structure of objects on large scales in the universe. The first three forces are described by quantum field theories (QFTs) as part of the standard model in particle physics - the most successful theory in science, which is falsified up to very high energies with incredibly high precision. Quantized fields represent the physical objects in QFTs and particles are described as quanta thereof. On the other side, gravity is described by general relativity as a classical, non-quantized field theory. So far, efforts to combine quantum mechanics and general relativity into an unified framework failed. String theory can be seen as a promising candidate towards that direction. Although pure *stringy* predictions are questionable and debated due to energy scales that are beyond experimental verification, applications of string theory methods can still be very helpful to explore properties of QFTs that are attainable in realistic experiments.

In this work, we use the so-called gauge/gravity duality to explore properties of Quantum Chromodynamics (QCD). QCD is the theory of strong interactions and part of the standard model. Its fundamental degrees of freedom are quarks and gluons. Additionally to the electric charge, those particles carry also a color charge. Due to color confinement, the hypothesis is put forward that only color-neutral hadronic matter states are observable. Examples for hadrons are mesons, which are composed of a quark-antiquark pair (e.g. pions) and baryons, which are made of three quarks (e.g. protons and neutrons as constituents of atomic nuclei); virtual quark-antiquarks and gluons make these, in total uncolored, objects to complicated composites. An important property of QCD is the “running” of the coupling constant. That is, the interaction strength between particles decreases at high energies. This asymptotic freedom causes a confinement-deconfinement transition at high energies. Put another way, a quark-gluon plasma (QGP) is formed at high temperatures and/or densities, where quarks are not bound into hadrons any more. The QGP is an extreme state of matter that existed in the early evolution of the universe after the big bang. During the evolution of the universe the cooling caused the quarks and gluons conversely to form nucleons, which represented the foundation for the subsequent formation of atomic nuclei. Another place where the QGP exists is in neutron stars and possible quark stars, i.e. in the interior of supernova type II remnants. Most importantly, the QGP is created in heavy-ion collisions (HIC) at facilities

like the Relativistic Heavy Ion Collider (RHIC) in Brookhaven or the Large Hadron Collider (LHC) at the European Organization for Nuclear Research (CERN). Moreover, the planned Compressed Baryonic Matter (CBM) experiment at the Facility for Antiproton and Ion Research (FAIR) in Darmstadt plans to study properties of the QGP at high densities [4]. Such experiments already revealed some fascinating properties: The QGP is not only the most perfect [5–8] but also the fastest-rotating (i.e. most vortical) fluid [9] ever measured in the entire universe. From the first property, one can conclude that the QGP is a strongly interacting liquid. The main interest of current research is the exploration of the QCD phase diagram, i.e. the different phases of strongly interacting matter, which are typically considered in the temperature-chemical potential or temperature-density plane. It is believed that the phase diagram exhibits a rich variety of different structures. Besides the already mentioned confined phase at low densities and temperatures and the QGP in the opposite regime, phases like color superconductors and quarkyonic matter could also exist. The exact structure of the phase diagram and types of different phase transitions are unknown. In particular, the possible existence of a critical endpoint (CEP) as the starting point of a first-order phase transition (FOPT) curve towards larger chemical potential or density is of utmost importance and a motivation for current and planned HIC experiments.

Perturbative methods are not applicable to study the strongly coupled QGP, since the series expansion does not converge. A well-established non-perturbative method to deal with QCD thermodynamics is lattice gauge theory. Here, spacetime is turned into an Euclidean one which is discretized on a lattice grid and the QCD path integral is evaluated statistically via Monte-Carlo integration. Although lattice QCD established the confinement-deconfinement transition at vanishing chemical potential as an analytic crossover already a long time ago [10], consistent results for the corresponding equation of state (EoS) are available only for a few years [11, 12]. These results determined the characteristic scale of the hadron-quark (HQ) deconfinement transition as $T_c = \mathcal{O}(150 \text{ MeV})$. Despite these tremendous successes, lattice QCD is limited up to now to calculations at vanishing chemical potential, i.e. on the temperature axis of the phase diagram, because of the so-called sign problem related to the fermionic determinant appearing in the former expressions.

A promising approach that allows phenomenological model calculations even at finite chemical potential and density is the so-called gauge/gravity duality. A first hint for such a duality was already prophesied decades ago by 't Hooft in his famous paper about planar diagrams [13], where he considered the large- N limit of a gauge theory and linked it with a dual string. The idea of a holographic principle was developed later by 't Hooft and Susskind [14, 15] and refers to the concept that a QFT in d dimensions might be related to a gravitational theory in $d + 1$ dimensions, similar to a holographic image. This idea is supported by the fact that the black hole entropy, due to Bekenstein [16], is proportional to the area of the event horizon and not to the volume. A concrete realization of this principle was found by Maldacena in 1997 [17] and

others [18, 19]. It is now called AdS/CFT correspondence and states in the most general case that a type IIB superstring theory on $AdS_5 \times S_5$ is dual to a $\mathcal{N} = 4$ supersymmetric Yang-Mills theory (SYM). The latter one is a conformal field theory (CFT), which is characterized by a vanishing beta function in contrast to the QFTs in the standard model. However, in a certain limit, there is a correspondence between a strongly coupled QFT and a classical theory of gravity. The strong coupling on the QFT side is translated into weak coupling on the string side and vice versa, which makes applications to strongly coupled systems feasible and explains the term *duality*. (The lower-dimensional QFT “lives” on the boundary of the higher-dimensional gravity theory.) Such correspondences have successfully applied to describe HICs and many other examples in particle or condensed matter physics and are now summarized by the more general term gauge/gravity duality. One of the outstanding outcomes is the holographic result for the shear viscosity to entropy density ratio [20]

$$\frac{\eta}{s} \geq \frac{1}{4\pi}, \quad (1.1)$$

which agrees well with the experimental results cited above.² Holographic methods have also provided important insight into the time-dependent hydrodynamization and isotropization as well as the far-from-equilibrium dynamics of HICs.

The subject of this work is the investigation of the QCD phase diagram with holographic methods. We use a so-called Einstein-Maxwell-dilaton (EMd) model, which was initially introduced by Gubser and collaborators [21]. This bottom-up model is adjusted to known physical results from lattice QCD at vanishing chemical potential and then extrapolates the information to finite density. It is based on a five-dimensional gravity model in an asymptotic anti-de Sitter (AdS) spacetime that contains black hole solutions. The black hole thermodynamics of Bekenstein [16] and Hawking [22] is thus related to the QCD thermodynamics. In this sense, the EMd model provides a phenomenological bottom-up AdS/QCD duality. We are particularly interested in the prediction of a critical point and its properties. Moreover, we study the holographic entanglement entropy of this model. Entanglement is a unique property in quantum mechanics that separates it from classical physics. Historically, entanglement was discussed as a *spooky action at a distance* and seen with scepticism, e.g. by Einstein. Nowadays, entanglement between particles is experimentally well confirmed, and entanglement entropy is a widely used quantity to quantify this property. Also in this context, the *holographic dictionary* provides a tool to calculate entanglement entropy in strongly coupled systems. We use those methods to explore and characterize the resulting phase diagram.

This thesis is organized as follows. In chapter 2 we present the necessary background of QCD and the physics of HICs. We concentrate on the thermodynamic properties and relevant

² $\eta/s = 1/4\pi$ is often considered the universal lower bound; however, depending on the gravity dual employed, it may be larger or smaller than the quoted value.

features. The gauge/gravity duality is introduced in chapter 3 with the relevant background of the AdS/CFT correspondence. Chapter 4 contains our results for the holographic model. We first review the setup of the EMd model and present our adjustment to lattice QCD thermodynamics. We then present our holographic QCD phase diagram and its properties. This represents the first reliable discussion of an holographic result for the QCD phase diagram. Chapter 5 is devoted to entanglement entropy. It includes an introduction to the concept and the holographic result for our EMd model. The ability of entanglement entropy to characterize the QCD phase diagram is analyzed. We sum up in chapter 6 and discuss our work in the context of related literature. Detailed elaborations on the dilaton potential can be found in appendix A.

2 Quantum Chromodynamics and heavy-ion collisions

2.1 Lagrangian formulation and β function

Quantum Chromodynamics is the non-Abelian quantum field theory of strong interactions with $N_f = 6$ flavors ($f = u, d, s, c, b, t$) and $N_c = 3$ colors. We give an introduction into the relevant foundations in this section following [23, 24]. Further comprehensive discussions can be found in [25, 26].

The classical QCD Lagrangian

$$\mathcal{L}_{cl} = -\frac{1}{4}F_{\mu\nu}^a F_a^{\mu\nu} + \sum_f^{N_f} \bar{q}_f (i\gamma^\mu D_\mu - m_f) q_f \quad (2.1)$$

is the most general relativistically invariant and renormalizable Lagrangian, which is gauge invariant under $SU(N_c)$ color transformations.³ Each quark flavor is described by three color Dirac four-spinors $q_{f\alpha}^c$ with $c = 1, \dots, N_c$ as the color and $\alpha = 1, \dots, 4$ as the spinor index in the fundamental representation of $SU(N_c)$. Gluons as gauge bosons are described by 4-vectors A_μ^a in the adjoint representation ($a = 1, \dots, N_c^2 - 1$). The covariant derivative is given by $D_\mu = \partial_\mu - igA_\mu$ with $A_\mu \equiv A_\mu^a t_a$ and t_a are the representation matrices of $SU(N_c)$. The gluon field strength tensor is defined as

$$F_{\mu\nu}^a \equiv \partial_\mu A_\nu^a - \partial_\nu A_\mu^a + gf^{abc} A_\mu^b A_\nu^c, \quad (2.2)$$

where g is the gauge coupling and f^{abc} are the structure constants of the corresponding Lie algebra. The last term in (2.2) shows that next to quark-gluon interactions also self-interactions among gluons are allowed.

The quantized QCD needs to be regularized and renormalized to cancel divergences. This introduces an energy scale μ into the theory and the β function describes the dependence of

³The full QCD Lagrangian $\mathcal{L}_{QCD} = \mathcal{L}_{cl} + \mathcal{L}_{gauge} + \mathcal{L}_{FP} + \mathcal{L}_{ct} + \mathcal{L}_\theta$ contains also a gauge fixing term $\mathcal{L}_{gauge} = -\frac{1}{2\xi}(\partial^\mu A_\mu^a)^2$, the Fadeev-Popov ghost term $\mathcal{L}_{FP} = \bar{c}^a(-\partial^\mu D_\mu^{ac})c^c$ and counterterms \mathcal{L}_{ct} for a consistent quantization and renormalization. A possible CP violating term $\mathcal{L}_\theta = \theta \frac{g^2}{32\pi^2} \tilde{F}_{\mu\nu}^a F_a^{\mu\nu}$ is neglected in all of our considerations.

the coupling constant on μ (“running coupling”):

$$\beta(g) = \mu \frac{dg}{d\mu}. \quad (2.3)$$

At first-loop order, the result is

$$\beta(g) = - (11N_c - 2N_f) \frac{g^3}{48\pi^2} + \mathcal{O}(g^5), \quad (2.4)$$

which is negative and thus causes the important property of the asymptotic freedom: The coupling constant is decreasing with increasing energy (i.e. at short distances) or the characteristic momentum transfer of a physical process. By dimensional transmutation, QCD is not described by a dimensionless coupling but by a dimensional scale $\Lambda_{QCD} \simeq 200 \text{ MeV}$, which is typically chosen as the scale at which the coupling is of order one. At the Z boson pole, the strong coupling constant $\alpha_s \equiv \frac{g^2}{4\pi}$ assumes the value $\alpha_s(m_z) = 0.1181$ [27]. Perturbative calculations are therefore only possible for large energies with free quarks and gluons at high temperatures or densities. Explorations of the QCD phase diagram (cf. section 2.3) hence require strictly non-perturbative methods or model calculations.

An important property of QCD is the breaking of scale invariance at the quantum level. The classical QCD Lagrangian (2.1) possesses dilatational symmetry in the chiral limit $m_f \rightarrow 0$.⁴ Quantum effects break this (approximate) invariance and give rise to the scale of QCD, Λ_{QCD} . The expectation value of the trace of the energy-momentum tensor is an order parameter for this anomaly, given by

$$\langle T^\mu_\mu \rangle = \frac{\beta}{2g} \langle F_{\mu\nu}^a F_a^{\mu\nu} \rangle + (1 + \gamma_m) \sum_f m_f \langle \bar{q}_f q \rangle. \quad (2.5)$$

The first term, the gluon condensate, is dominating and originates from quantum effects, which are described by the QCD β function (2.3). The second term demonstrates that quark masses explicitly break scaling invariance. Quantum effects are encoded in

$$\gamma_m(g) = \frac{\mu}{m_f} \frac{dm_f}{d\mu}, \quad (2.6)$$

which describes the quark mass dependence on the renormalization scale.

The classical scaling dimension Δ_0 of a field operator \mathcal{O} , which is defined under dilatations $x \mapsto x' = \lambda x$ through the transformation $\mathcal{O} \mapsto \mathcal{O}'(x') = \lambda^{-\Delta_0} \mathcal{O}(x)$ also receives a quantum

⁴In this case, the Noether theorem implies the conservation law $\partial_\mu j^\mu = T^\mu_\mu$ for the current $j^\mu = x_\nu T^{\mu\nu}$. Scale invariance is therefore valid for a traceless energy-momentum tensor $T^{\mu\nu}$. Quark masses explicitly break this symmetry, but even then, a vanishing β function would be expected at high energies.

contribution $\Delta = \Delta_0 + \gamma$ by the anomalous dimension

$$\gamma(g) = \frac{1}{2} \frac{d \ln Z_{\mathcal{O}}}{d \ln \mu}, \quad (2.7)$$

where $Z_{\mathcal{O}}$ is the renormalization constant of \mathcal{O} .

The elaborated properties, most notably the asymptotic freedom and symmetries of QCD, determine the structure of the phase diagram and are responsible for the richness of phenomena related to strongly coupled physics.

2.2 Lattice gauge theory and thermodynamics

Lattice gauge theory is a fundamental approach to solve full QCD and calculate thermodynamic quantities. We give a basic introduction into the relevant concepts in this section, following [24, 25, 28, 29]. Detailed discussions can be found in [30].

In lattice QCD the grand partition function is computed in the path integral formalism. A discretized Euclidean spacetime of size $N_\tau \times N_s$ with lattice spacing a is used such that the temperature and volume are given by

$$T = \frac{1}{N_\tau a}, \quad V = (N_s a)^3. \quad (2.8)$$

The smallest and largest length scale introduce an UV cutoff $\Lambda_{UV} \sim a^{-1}$ as the maximum momentum scale and an IR regulator via $\Lambda_{IR} \sim (N_s a)^{-1}$ respectively. The grand partition function is then given by the Euclidean path integral

$$Z(T, V, \vec{\mu}) = \int \mathcal{D}A_\mu \mathcal{D}q_f \mathcal{D}\bar{q}_f e^{-S^E}, \quad (2.9)$$

where the product over all gauge field components and flavors is implicitly assumed. The Euclidean action

$$S^E(T, V, \vec{\mu}) \equiv - \int_0^{1/T} d\tau \int_V d^3x \mathcal{L}^E(\vec{\mu}) \quad (2.10)$$

contains the inverse temperature and imaginary time $\tau = it$. The quark chemical potentials μ_f couple to the conserved quark number currents in the Lagrangian

$$\mathcal{L}^E(\vec{\mu}) = \mathcal{L}_{cl}^E + \sum_f \mu_f \bar{q}_f \gamma_0 q_f \quad (2.11)$$

with \mathcal{L}_{cl}^E as the classical QCD Lagrangian (2.1) in Euclidean spacetime. To preserve gauge invariance, the gauge fields are discretized as variables on links between the lattice sites. Several discretization schemes exist that define the fermionic degrees of freedom on the lattice sites itself.

Splitting the action into the gluonic and fermionic part, $S^E = S_g + S_f$, the quark fields can be integrated out since the action is bilinear in the fermion fields. This gives the determinant of the Dirac operator, $\det M_f(A_\mu, \mu_f)$, and the partition function simplifies to

$$Z(T, V, \vec{\mu}) = \int \mathcal{D}A_\mu \det M_f(A_\mu, \mu_f) e^{-S_g}, \quad (2.12)$$

where the high-dimensional integral is expressed with link variables $U_{x,\hat{\mu}} \equiv \exp(iagA_\mu(x))$ as $\mathcal{D}A_\mu = \prod_{x,\hat{\mu}} dU_{x,\hat{\mu}}$. The path integral can then be evaluated on the grid with the Monte-Carlo method as a sum over all possible field configurations. This Euclidean approach allows to calculate time-independent quantities but not dynamical ones.

Physical quantities in lattice QCD are extracted in the continuum limit $a \rightarrow 0$. At finite temperature and volume, this is achieved by increasing the number of lattice points, $N_\tau, N_s \rightarrow \infty$, such that the quantities in Eq. (2.8) are kept constant.⁵ The bare coupling in lattice QCD is adjusted such that asymptotic freedom corresponds to the limit $g(a \rightarrow 0) \rightarrow 0$. In this continuum limit, Lorentz invariance is restored and lattice QCD is renormalizable, i.e. UV divergences can be absorbed in the masses and coupling constants, such that physical observables are independent of the lattice spacing.

The EoS follows from the grand canonical potential

$$\Omega(T, V, z_f) = T \ln Z(T, V, z_f) - p_0 \quad (2.13)$$

with $z_f \equiv e^{\mu_f/T}$ as the fugacity related to the quark chemical potential μ_f . The normalization $p_0 = \lim_{T \rightarrow 0} T \ln Z(T, V, 1)$ is the vacuum pressure and is chosen such that Ω vanishes at zero temperature. By standard thermodynamic relations, the pressure p , energy density ϵ and speed of sound squared v_s^2 are obtained as

$$p = \frac{1}{V} \Omega(T, V, z_f), \quad \epsilon = \frac{T^2}{V} \frac{\partial \Omega(T, V, z_f)/T}{\partial T}, \quad v_s^2 = \frac{dp}{d\epsilon}. \quad (2.14)$$

Computationally, the basic observable in lattice QCD is the interaction measure I , which is related to the thermodynamic quantities and the thermal contribution to the trace of the energy-momentum tensor through the anomaly (2.5) as

$$I \equiv \epsilon - 3p = T^5 \frac{d}{dT} \left(\frac{p}{T^4} \right) = T^\mu_\mu = -\frac{T}{V} \frac{d \ln Z}{d \ln a}, \quad (2.15)$$

such that the pressure follows from integration (see e.g. [12] for details of the numerical procedure). At non-vanishing quark chemical potential, the quark densities n_f and entropy density

⁵The thermodynamic limit $V \rightarrow \infty$ for a given temperature requires $N_s \gg N_\tau$.

s are given by

$$\frac{n_f}{T^3} = \frac{1}{VT^3} \frac{\partial p/T^4}{\partial \mu_f/T}, \quad \frac{s}{T^3} = \frac{\epsilon + p}{T^4} - \sum_f \frac{n_f \mu_f}{T^4}. \quad (2.16)$$

Lattice QCD is now a well established quantitative method to solve full QCD at vanishing chemical potential. We will use results from these calculations in section 4.2 to adjust a holographic model to the thermodynamics. A direct evaluation of the partition function for $\mu_f > 0$ is, however, restricted by the sign problem: The fermion determinant becomes imaginary in this case and prevents a probabilistic integration. There are several approaches like the reweighting method, evaluations at imaginary μ_f , Taylor expansions, a complex Langevin method or a path optimization method that try to avoid or circumvent the sign problem. All of these ansätze, however, have intrinsic limitations and are, at best, limited to small chemical potentials.

2.3 The QCD phase diagram

It is believed that QCD exhibits a rich phase diagram as illustrated in Fig. 2.1 (left panel).⁶ An ultimate goal of current research is to explore these different structures, which are typically considered in the temperature-net baryon density plane (as in Fig. 2.1) or in the temperature-baryon chemical potential plane. In the following discussion, we present some important properties of these phases, following [23] and [24, 28, 29].

Let us start by looking at the zero temperature case, i.e. on the μ -axis at $T = 0$. Microscopically, attractive and repulsive forces between nucleons compete such that the ground state is assumed at a finite baryon density $n_0 \simeq 0.17 \text{ fm}^{-3}$. Nuclear matter in this ground state is stable, i.e. the pressure vanishes, $p = 0$, and therefore the baryon density $n(\mu)$ vanishes below some value $\mu_0 \simeq 924 \text{ MeV}$. The thermodynamic stability at smaller densities $n < n_0$ is preserved through fragmentation of nuclear matter into droplets of constant density n_0 . At finite but small temperature, single nucleons can thermally evaporate. The phase transition between nucleons in a mixed phase at low densities/chemical potential and nuclear matter at larger densities is well established as a gas-liquid (GL) FOPT curve terminating into a second-order critical point towards smaller chemical potential at a temperature in the order of 10 MeV. With increasing chemical potential μ , the pressure $p = \int n d\mu$ is increasing too. This region of the phase diagram is particularly important for the description of neutron or quark stars and core-collapse supernova explosions.

On the temperature axis, i.e. for $\mu = 0$, there is a phase transition between the hadronic phase at low temperatures and the QGP at high temperatures. In the hadronic phase, quarks and gluons are confined as colorless bound states, whereas the deconfined QGP is a strongly interacting near-ideal liquid, as suggested by experiments. The existence of a QGP phase

⁶Historically, the first remarks on QCD related phase transitions can be found in [32].

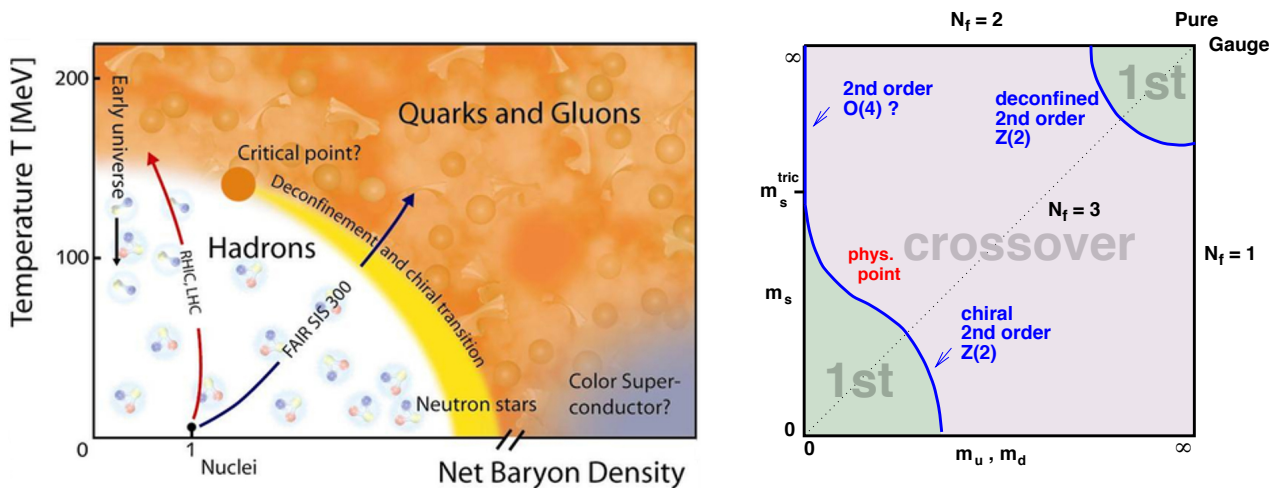


Figure 2.1: Left Panel: The QCD phase diagram with expected phases of strongly interacting matter. The net baryon density is related to the baryo chemical potential. (Figure: GSI, Darmstadt) Right panel: The Columbia plot sketches the type of the QCD phase transition at $\mu = 0$ in dependence of the quark masses for different flavors. (Figure taken from [31])

follows from the decreasing beta function, i.e. the asymptotic freedom in QCD. The Columbia plot [33] in Fig. 2.1 (right panel) shows the qualitative options for the type of this phase transition in dependence of the u, d, s quark masses $m_{u,d,s}$. (See [34] for recent investigations.) In the chiral limit, $m_{u,d,s} \rightarrow 0$ (lower left corner), and the infinitely heavy quark-mass limit, $m_{u,d,s} \rightarrow \infty$ (upper right corner), the deconfinement transition is a FOPT. These FOPT regions extend into the mass plane and are bounded by second-order transition lines. Such a critical line extends also from the upper left corner along the m_s axis and meets the FOPT region at a tricritical point. The rest of the quark-mass diagram is the crossover region. Lattice QCD revealed that the confinement-deconfinement transition in the real world with physical quark masses is a crossover [10] in the temperature range 150 – 170 MeV [11, 12].

The crossover-deconfinement transitions extends from the temperature axis into the phase diagram at finite chemical potential. There is the possibility that a true FOPT curve is emerging at a CEP towards larger chemical potential down to the μ -axis. Some recent remarks on the experimental signatures of a CEP in HICs can be found in [35]. Lattice calculations in this region are hampered by the sign problem. The exact phase structure in this range is therefore unconfirmed and especially model calculations become relevant. Such approaches predict for example color superconductors, quarkyonic matter or color-flavor locked structures. We however emphasize that current research is far away from a complete understanding of the entire phase diagram and many subtleties may arise, similar to the sensitive quark mass dependence in the Columbia plot already at $\mu = 0$.

Beyond the confinement-deconfinement transition, also chiral symmetry plays an important role in the QCD phase diagram. In the limit of massless flavors $m_u = m_d = m_s = \dots = 0$, the QCD Lagrangian is invariant under chiral transformations, i.e. independent global rotations

of left and right handed quarks, and therefore acquires the symmetry⁷

$$U(N_f)_L \times U(N_f)_R \simeq SU(N_f)_L \times SU(N_f)_R \times U(1)_V \times U(1)_A. \quad (2.17)$$

The QCD ground state spontaneously breaks the global flavor symmetry $SU(N_f)_L \times SU(N_f)_R$, generating three massless Goldstone pseudoscalar bosons and a non-vanishing quark-antiquark vacuum expectation value $\langle \bar{q}q \rangle$ (also called chiral condensate). At the physical point, the massive pions are interpreted as these approximate Goldstone bosons. In the QGP phase at high temperatures, asymptotic freedom suggests that condensates disappear and chiral symmetry is (approximately) restored. Thus, a phase transition to the chirally symmetric equilibrium state is expected at some temperature $T \sim \Lambda_{QCD}$. The exact nature of this transition and its relation to the deconfinement transition is unknown.

2.4 Heavy-ion collisions

Heavy-ion collisions are an experimental method to study the QCD phase diagram. In such collisions, a QGP can be created, which undergoes the transition to hadron matter similar to the evolution in the early universe at about $10 \mu s$ after the big bang. We give a brief introduction into the most relevant physical principles that govern such collisions, based on [36] and [25]. The former is an up to date review, which also discusses modern holographic approaches. Further information on that topic can be found in [26, 37].

There are two general ways how HICs can be performed: Central collisions with Lorentz-contracted nuclei create excited matter at high temperature, while fixed-target experiments compress the nuclear matter to high density. Our current understanding separates the evolution of HICs into three stages with a characteristic proper time scale $\tau_0 \sim 1 \text{ fm}$ (cf. Fig. 2.2 for an illustration in the space-time diagram):

- i) In the initial or pre-equilibrium stage ($0 < \tau < \tau_0$), the two nuclei pass through each other. This process is accompanied by a huge entropy production, whose microscopic origin is not fully understood. The difficulties arise due to the time-dependent non-equilibrium processes of QCD. The local thermalization produces the initial condition of the hydrodynamic evolution in the second stage. Microscopic models such as the Color Glass Condensate or AdS/CFT approaches suggest that the matter undergoes presumably a very fast thermalization and is dominated by gluons.
- ii) In the hydrodynamic stage ($\tau_0 < \tau < \tau_f$), after local thermal equilibrium is reached at τ_0 , the dynamical evolution can be described very well by relativistic viscous hydrodynamics.

⁷The $U(1)_V$ symmetry reflects the baryon number conservation and the axial symmetry $U(1)_A$ is explicitly broken by quantum fluctuations.

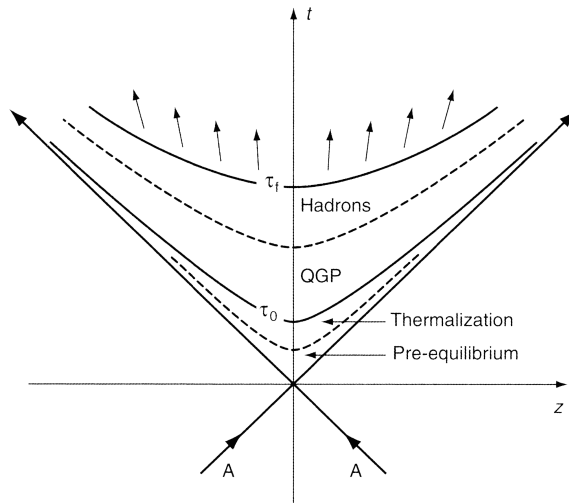


Figure 2.2: Time evolution of a ultra-relativistic HIC in the space-time diagram. The collision of two nuclei with mass number A takes place at the origin and the subsequent stages are shown inside the light cone. The hyperbolas are contour curves of constant proper time $\tau = (t^2 - z^2)^{1/2}$; τ_0 and τ_f are the characteristic time scales of the thermalization and freeze-out respectively. Figure taken from [25].

This framework is based on the conservation of the energy-momentum tensor and baryon number:⁸

$$\partial_\mu \langle T^{\mu\nu} \rangle = 0, \quad \partial_\mu \langle j_B^\mu \rangle = 0. \quad (2.18)$$

The microscopic input is encoded in the EoS $p(\epsilon)$ for a perfect fluid. Higher-order hydrodynamics also requires viscosities and conductivities as input. Such calculations were successfully applied to describe the time development of the second stage, in which the transition to the hadronic phase takes place.

- iii) In the freeze-out and post-equilibrium stage ($\tau > \tau_f$), the final state particles decouple and become free at some proper time $\tau_f > \tau_0$. The mean free path and time of plasma particles is increasing in this stage. There are two types of freeze-out, which depend on the hadron species: The chemical freeze-out takes places first and leaves the number of each particle species constant (equilibrium is still present), while after thermal freeze-out the particle momenta remain constant (local thermal equilibrium is no longer maintained).

During these stages the fireball of the HIC is expanding and cooling. The density is therefore decreasing and the final particles can be registered in the detectors. The key insight from holography was the result that the strongly-coupled fluid can hydrodynamize when it is still in an anisotropic state far from equilibrium [38–42].

There are several experimental signatures of the QGP in HICs, such as an increase in the

⁸As explained in [25], the expectation value is taken w.r.t. time-dependent states in local thermal equilibrium. See this reference for further details.

elliptic flow, jet quenching or modifications of properties of heavy mesons (J/Ψ , Υ , ...). Other effects are a rise in the average transverse momentum, caused by the increasing entropy during the phase transition, or an enhanced production of strangeness and charm. Further signatures and their relation to experimental data are discussed in [25, 26].

3 The gauge/gravity duality

In this chapter we describe the relevant foundations of the gauge/gravity duality and the AdS/CFT correspondence. These concepts relate different areas of physics, namely a conformal QFT to a higher-dimensional string theory. Since the CFT is defined in flat space and string theory is a quantized gravitational theory, the gauge/gravity duality provides also a promising approach towards quantum gravity. This concrete duality is also a realization of the holographic principle, which states that the number of degrees of freedom in a volume scale with the surface area of that volume for a gravitational theory. The original AdS/CFT proposal by Maldacena in [17] was refined in [18, 19] regarding the calculation of correlation functions and an operator/field relation. This remarkable duality between different fields in physics allowed insights into foundational questions and provided new methods to tackle problems in various areas of physics. By now, there are several good textbooks on this topic [37, 43–46]. We will mainly follow [43] and [37] in our discussions in this chapter. It is not our intention to give an profound introduction into string theory. We refer to the literature [47–49] and the discussions in the aforementioned textbooks for introductions.

3.1 Anti-de Sitter spacetimes

The AdS spacetime is a maximally symmetric spacetime with negative cosmological constant, which appears on the gravity side of the AdS/CFT correspondence. In $d+1$ dimensions, AdS_{d+1} is defined as an embedding in $(d+2)$ -dimensional Minkowski spacetime $(X^0, \dots, X^{d+1}) \in \mathbb{R}^{d,2}$ with metric $\bar{\eta} = \text{diag}(-, +, \dots, +, -)$ as the hyperboloid

$$\bar{\eta}_{MN} X^M X^N = -(X^0)^2 + \sum_{i=1}^d (X^i)^2 - (X^{d+1})^2 = -L^2, \quad (3.1)$$

where $M, N \in \{0, \dots, d+1\}$. This spacetime possesses $SO(d, 2)$ invariance and admits the maximum number of Killing vectors, i.e. it is maximally symmetric with constant curvature. Furthermore, an AdS_{d+1} spacetime has a conformal boundary, which is a compactification of d -dimensional Minkowski spacetime, and can be represented as the set of all lines on the light cone $\bar{\eta}_{MN} X^M X^N = 0$ originating from $0 \in \mathbb{R}^{d,2}$ [43].

AdS spacetimes can be represented in several common coordinate systems. Global coordinates

(ρ, τ, Ω_i) cover the whole AdS space and the metric takes the form⁹

$$ds^2 = L^2 (-\cosh^2 \rho d\tau^2 + d\rho^2 + \sinh^2 \rho d\Omega_{d-1}^2). \quad (3.2)$$

Introducing a new coordinate θ by $\tan \theta = \sinh \rho$ and rescaling gives the compactified metric

$$ds^2 = -d\tau^2 + d\theta^2 + \sin^2 \theta d\Omega_{d-1}^2, \quad \theta \in [0, \pi/2], \quad \tau \in [0, 2\pi), \quad (3.3)$$

which is also known as the ‘‘Einstein static universe’’. The periodicity in τ allows closed timelike curves, causing causal inconsistencies. The problem is solved by considering the universal cover, i.e. unwrapping the circle, such that $\tau \in \mathbb{R}$ with no identifications. The Penrose diagram of AdS₂ in these coordinates is an infinite strip between $\theta = -\pi/2$ and $\theta = +\pi/2$ while the conformal diagram for full AdS _{$d+1$} follows by adding a sphere S_{d-1} to each point. This demonstrates that the boundary of AdS _{$d+1$} spacetime is $\mathbb{R}_\tau \times S_{d-1}$. Poincaré patch coordinates $t \in \mathbb{R}$, $\vec{x} = (x^1, \dots, x^{d-1}) \in \mathbb{R}^{d-1}$, $r \in \mathbb{R}_+$ cover only half of the spacetime and the metric is given by

$$ds^2 = \frac{L^2}{r^2} dr^2 + \frac{r^2}{L^2} (-dt^2 + d\vec{x}^2), \quad (3.4)$$

exhibiting a conformal boundary at $r \rightarrow \infty$.¹⁰ The fifth coordinate can be interpreted as a warp direction that is relevant for holographic interpretations. The Ricci scalar in these coordinates is $R = -\frac{d(d+1)}{L^2} = \text{const} < 0$, demonstrating that L represents the curvature radius. This spacetime satisfies the source-free Einstein field equations $R_{MN} - \frac{1}{2}Rg_{MN} + \Lambda g_{MN} = 0$, following from the Hilbert action

$$S = \frac{1}{16\pi G_N^{(d+1)}} \int d^{d+1}x \sqrt{-g} (R - 2\Lambda), \quad (3.5)$$

if the cosmological constant Λ is chosen as

$$\Lambda = -\frac{d(d-1)}{2L^2} < 0. \quad (3.6)$$

Particular important for AdS/CFT interpretations are black hole solutions in asymptotic AdS spacetimes. That means that these spacetimes are on the boundary locally isometric to an AdS space and solve the Einstein field equations with negative cosmological constant. The corresponding thermodynamic quantities have interpretations on the gauge theory side.

⁹The coordinate system follows from the initial definition (3.1) through the parametrization $X^0 = L \cosh \rho \cos \tau$, $X^{d+1} = L \cosh \rho \sin \tau$, $X^i = L \Omega_i \sinh \rho$ ($i = 1, \dots, d$), where Ω_i are angular coordinates satisfying $\sum_i \Omega_i^2 = 1$ and $\rho \in \mathbb{R}_+$, $\tau \in [0, 2\pi)$.

¹⁰The coordinates (3.1) are parametrized as $X^0 = \frac{L^2}{2r} \left(1 + \frac{r^2}{L^4} [\vec{x}^2 - t^2 + L^2]\right)$, $X^i = \frac{rx^i}{L}$ ($i = 1, \dots, d-1$), $X^d = \frac{L^2}{2r} \left(1 + \frac{r^2}{L^4} [\vec{x}^2 - t^2 - L^2]\right)$, $X^{d+1} = \frac{rt}{L}$.

3.2 Aspects of conformal field theories

In QFT, the Coleman-Mandula theorem states that the Poincaré algebra cannot be extended, since the S-matrix would vanish. There are, however, two loopholes: Theories without a mass gap and S-matrix can be a representative of the conformal algebra while the introduction of graded Lie algebras realizes the supersymmetry (SUSY) algebra. In the context of the AdS/CFT correspondence, both properties are realized in $\mathcal{N} = 4$ SYM theory. We describe the important properties of such CFTs in this section, following [43, 44].

CFTs are quantum field theories which are invariant under conformal transformations. These are coordinate transformations in flat spacetime that locally preserve angles. The metric components transform as

$$g_{\mu\nu}(x) \mapsto \Omega(x)^{-2} g_{\mu\nu}(x) =: e^{2\sigma(x)} g_{\mu\nu}(x) \quad \Leftrightarrow \quad ds'^2 = e^{2\sigma(x)} ds^2, \quad (3.7)$$

which preserves the causal structure. For an infinitesimal conformal transformation $x^\mu \mapsto x^\mu + \epsilon^\mu(x)$, the definition (3.7) implies

$$(g_{\mu\nu} \partial_\rho \partial^\rho + (d-2) \partial_\mu \partial_\nu) \partial_\mu \epsilon^\mu = 0. \quad (3.8)$$

The case $d = 2$ is obviously different but not relevant for our considerations. We therefore assume $d > 2$, where the most general solution has the form

$$\epsilon^\mu(x) = a^\mu + \omega^\mu{}_\nu x^\nu + \lambda x^\mu + b^\mu x^2 - 2(b \cdot x) x^\mu. \quad (3.9)$$

The parameters a^μ , $\omega_{\mu\nu}$, λ and b_μ correspond to translations, Lorentz transformations, dilatations and special conformal transformations respectively.¹¹ These transformations form the symmetry group $SO(d, 2)$, which is the same as for AdS_{d+1} spacetime in the previous section. This agreement of the symmetry groups is already a strong hint for a possible relation between CFTs in flat space and a gravitational theory in an AdS space. The generators of this group form the corresponding algebra, in particular the momentum vector P^μ for translations, the dilatation generator D and K_μ for special conformal transformations, which are given with associated commutation relations.

Beyond the group theoretic point of view, there is also an important relation between scale and conformal invariance: Conformal invariance is a local symmetry that generalizes global scale invariance. As discussed in section 2.1 in the context of QCD, classical scale invariance can be broken at the quantum level through anomalies. Local conformal invariance, however, cannot be broken quantum-mechanically; this absence of quantum anomalies constrains the theory.

¹¹Special conformal transformations are given by $x^\mu \mapsto \frac{x^\mu + b^\mu x^2}{1 + 2b \cdot x + b^2 x^2}$. They can be decomposed into an inversion, translation and another inversion. Subtleties regarding a mapping to infinity and conformal compactification are discussed in [43].

A quantum-mechanically scale invariant theory can be realized by a vanishing β function or a nontrivial interacting fixed point. So far, all such known theories are also conformal invariant. Field transformations in CFTs are performed in irreducible representations of the conformal algebra. Induced representations are constructed from eigenfunctions of the the scaling operator D with eigenvalue $-i\Delta$, where Δ is the scaling dimension of ϕ (cf. section 2.1 for the definition). The generator P_μ increases Δ and acts similar to a creation operator

$$[D, P_\mu] = -iP_\mu \quad \Rightarrow \quad D(P_\mu\phi) = -i(\Delta + 1)(P_\mu\phi), \quad (3.10)$$

while K_μ decreases Δ similar to an annihilation operator due to

$$[D, K_\mu] = iK_\mu. \quad (3.11)$$

The primary operator Φ_0 is the lowest dimensional operator in this conformal algebra, defined by $K_\mu\Phi_0 = 0$. Successive application of P_μ and K_μ generates arbitrary states in the CFT.

Conformal invariance has some important consequences on observables and quantities in the QFT. For example, the two-point correlator of two arbitrary operators has the general form

$$\langle \mathcal{O}_i(x)\mathcal{O}_j(y) \rangle = \frac{C\delta_{ij}}{|x-y|^{\Delta_i+\Delta_j}}, \quad (3.12)$$

which follows from the operator product expansion up to some normalizable constant $C = 1$. Another important property is the tracelessness of the energy-momentum tensor:¹²

$$T^\mu{}_\mu = 0, \quad (3.13)$$

which ensures scale invariance of the classical field theory.

For the formulation of the AdS/CFT correspondence, $\mathcal{N} = 4$ SYM theory in $d = 4$ is relevant, which is a representation of the conformal group with with the largest amount of supersymmetry (i.e. 16 supercharges without gravity).¹³ This non-Abelian gauge theory contains a gauge field $A_\mu(x)$, four Weyl fermions $\lambda_\alpha^a(x)$ ($a = 1, \dots, 4$) and six real scalars $\phi^i(x)$ ($i = 1, \dots, 6$), which transform in the adjoint representation of $SU(N_c)$. The Lagrangian can be constructed in the superspace formalism or obtained from $\mathcal{N} = 1$ SYM theory in ten dimensions through dimensional reduction. The unique result has the Yang-Mills coupling constant g_{YM} and the number of colors N_c as parameters. The fields have mass dimensions $[A_\mu] = 1$, $[\lambda^a] = 3/2$, $[\phi^i] = 1$. Since $[g_{\text{YM}}] = 0$, the theory is classically scale invariant. In fact, $\mathcal{N} = 4$ SYM theory

¹²According to the Noether theorem, the energy-momentum tensor is the conserved current for translations. Scaling invariance restricts this tensor to be traceless due to the conserved dilatation current. This is also valid for the definition $T_{\mu\nu} = -\frac{2}{\sqrt{-g}}\frac{\delta S}{\delta g^{\mu\nu}}$ w.r.t. the classical action $S = \int d^d x \sqrt{-g} \mathcal{L}$ for scalings $g_{\mu\nu} \mapsto (1 + h(x^\mu))g_{\mu\nu}$, which imply $\delta g_{\mu\nu} = \delta h(x^\alpha)g_{\mu\nu}$ and thus $0 = \delta S = \int d^d x \sqrt{-g} \frac{1}{2} T^{\mu\nu} g_{\mu\nu} \delta h(x^\alpha)$.

¹³The supergroup is $SU(2, 2|4)$ [50]. It contains the conformal symmetry, R-symmetry, Poincaré supersymmetries and conformal supersymmetries.

is also at the quantum level scale invariant, because the β functions vanishes to all orders. It is expected that this theory is UV finite, since no UV divergences appear in the correlation functions of its fields. Moreover, from the discrete global S-duality group, one can infer a strong-weak duality, i.e. the invariance under the transformation $g_{\text{YM}} \leftrightarrow 4\pi/g_{\text{YM}}$.

3.3 The AdS/CFT correspondence

Motivation

We have already seen a hint for the AdS/CFT duality as a relation between a CFT_d and a theory of gravity in an AdS_{d+1} spacetime through the agreement of the symmetry groups. As explained in [37], this correspondence can be further motivated as a geometrization of the renormalization group (RG) flow: For a QFT in d Minkowski dimensions with a short-distance cutoff ϵ , an effective field theory at some length scale $z \gg \epsilon$ can be obtained by integrating out the short-distance degrees of freedom. The RG scale z can be interpreted as a spatial dimension, such that the resulting continuous family of effective field theories can be embedded into a single $(d+1)$ -dimensional theory. The holographic principle suggests that this theory could be a theory of quantum gravity. String theory as the natural candidate can be inferred from 't Hooft's large- N_c expansion of non-Abelian gauge theories [13].¹⁴ An AdS spacetime as the correct geometry for the $(d+1)$ -dimensional string theory is implied by requiring d -dimensional Poincaré and conformal symmetry.¹⁵

Derivation

The precise formulation of the AdS/CFT correspondence is obtained by analyzing two different prescriptions of Dp -branes (cf. Fig. 3.1). For that, we consider a type IIB string theory as a representative of a supersymmetric string theory in ten dimensions. The key insight is that (extremal) p -branes and Dp -branes are describing the same object [51]. The former are supergravity solutions and represent black holes in p spatial dimensions. On the other side, Dp -branes are dynamical solitonic objects on that open strings can end, occupying a p -dimensional

¹⁴This means that the expansion of the Euclidean partition function in powers of $1/N_c$ shows a remarkable similarity with the perturbative expansion of a closed string theory if one identifies $g_s \sim 1/N_c$, where g_s is the string coupling.

¹⁵As elaborated in [37], the most general ansatz $ds^2 = \Omega^2(z) (-dt^2 + d\vec{x}^2 + dz^2)$ needs to be invariant under $(t, \vec{x}) \rightarrow C(t, \vec{x})$ for some constant C to incorporate conformal invariance with simultaneous scaling of the holographic coordinate $z \rightarrow Cz$. This determines the conformal factor as $\Omega(z) = L/z$ for some constant L . The metric therefore takes the form

$$ds^2 = \frac{L^2}{z^2} (-dt^2 + d\vec{x}^2 + dz^2), \quad (3.14)$$

which is an AdS_{d+1} spacetime. Note that the coordinate z is related to r as $z \equiv \frac{L^2}{r}$ in the Poincaré coordinates (3.4). The Minkowski boundary is located at $z = 0$.

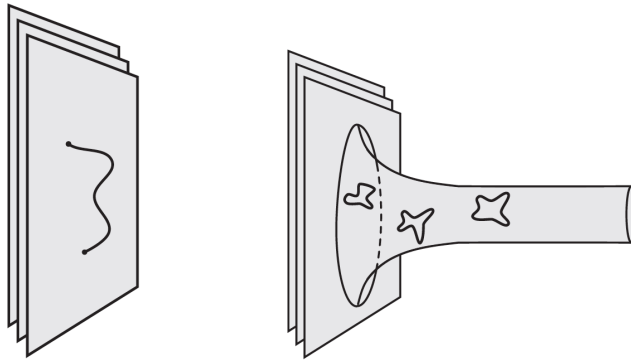


Figure 3.1: Illustration of the open string (left) and closed string perspective (right) of Dp -branes. Figure taken from [43].

subspace. For the following discussion, D3-branes that sweep out a 4-dimensional worldvolume are relevant. Consider now a stack of N_c coincident D3-branes along the spacetime directions x^0, \dots, x^3 transversal to x^4, \dots, x^9 .

- i) In the open string perspective, one treats the strings as small perturbations in the limit of small string coupling constant $g_s \ll 1$. The string spectrum contains finitely many massless modes and an infinite number of massive modes in this case. The former consists of an Abelian gauge field $A_\mu(x)$ (describing parallel open string excitations) and six scalar fields $\phi^i(x)$ (describing transverse fluctuations) for a single D3-brane (together with their superpartners). In the limit of small energies $E \ll \alpha'^{-1/2}$ only massless modes contribute.¹⁶ The effective action has contributions from closed and open string modes as well as their interactions:

$$S = S_{\text{closed}} + S_{\text{open}} + S_{\text{int}}. \quad (3.15)$$

In the limit $\alpha' \rightarrow 0$, S_{int} vanishes (decoupling of open and closed strings), while S_{closed} gives free supergravity in Minkowski spacetime. Moreover, S_{open} leads to the bosonic part of $\mathcal{N} = 4$ SYM theory for the identification $2\pi g_s = g_{\text{YM}}^2$ with gauge group $U(N_c)$. The $U(1)$ part (center of mass motion) decouples from the remaining $SU(N_c) \subset U(N_c)$ modes (describing the brane motions relative to one another).

- ii) The closed string perspective is valid for $g_s N_c \rightarrow \infty$, where one treats Dp -branes as massive objects that gravitate, i.e. curve the surrounding spacetime, by interchanging the strong coupling and low-energy limit. The supergravity solution for D3-branes takes the form

$$ds^2 = H^{-1/2} (-dt^2 + d\vec{x}^2) + H^{1/2} (dr^2 + r^2 d\Omega_5^2), \quad H(r) = 1 + \left(\frac{L}{r}\right)^4, \quad L^4 = 4\pi g_s N_c \alpha'^2, \quad (3.16)$$

¹⁶ α' is defined as $\alpha' = l_s^2$, where l_s is the fundamental string length scale.

where $r^2 \equiv \sum_{i=4}^9 x_i^2$ is a radial coordinate and L can be interpreted as the characteristic length scale of gravitational effects. In the limit $r \gg L$, one has $H(r) \sim 1$ and the metric represents a ten-dimensional Minkowski spacetime. In the near-horizon region $r \ll L$, where gravitational effects become strong, the metric reduces to

$$ds^2 = \frac{r^2}{L^2} (-dt^2 + d\vec{x}^2) + \frac{L^2}{r^2} dr^2 + L^2 d\Omega_5^2, \quad (3.17)$$

which is the metric of an AdS_5 spacetime times a compact five-sphere S_5 . These two regimes decouple in the low-energy supergravity limit of type IIB superstring theory, i.e. there are closed strings in flat Minkowski spacetime and, on the other side, closed strings propagating in the curved throat near the horizon of the Dp -brane.

In summary, we found two different descriptions of the same physical object with two decoupled theories in the low-energy limit respectively. The type IIB supergravity theories on $\mathbb{R}^{9,1}$ agree in both descriptions. It is therefore natural to conjecture that also the other two theories can be identified. The $\text{AdS}_5/\text{CFT}_4$ correspondence thus states the equivalence between the following two theories¹⁷

$$\mathcal{N} = 4 \text{ } SU(N_c) \text{ SYM in } \mathbb{R}^{1,3} \quad \iff \quad \text{IIB superstring theory in } \text{AdS}_5 \times S_5 \quad (3.18)$$

with parameter mapping

$$g_{\text{YM}}^2 = 2\pi g_s \quad \text{and} \quad 2g_{\text{YM}}^2 N_c = \left(\frac{L}{l_s}\right)^4. \quad (3.19)$$

Validity

The AdS/CFT correspondence relates different types of theories. In the strongest form, the correspondence is believed to hold for any values of the parameter mapping. For the strong form one considers the classical gravitational limit $g_s \ll 1$ at constant L/l_s . The first relation in Eq. 3.19 then implies $g_{\text{YM}} \ll 1$ and from the second mapping we infer that the 't Hooft coupling $\lambda \equiv g_{\text{YM}}^2 N_c$ is kept constant for $N_c \rightarrow \infty$. This is the planar limit of the CFT and the AdS/CFT correspondence hence is a concrete realization of the holographic principle as motivated above. For the weak form of the correspondence one assumes additionally the strongly coupled field theory limit $\lambda \rightarrow \infty$, which maps to $l_s/L \rightarrow 0$, i.e. the supergravity limit at vanishing string length. As a result, the holographic *duality* is relating a strongly coupled QFT to a weakly coupled gravitational theory, which is an important advantage for practical calculations.

¹⁷We defined the low-energy condition down such that the duality holds even for superstring theory and not only supergravity.

3.4 Elements of the gauge/gravity duality

Inspired by the discussions in [37] and [52], we discuss some important aspects and concepts of the holographic dictionary in this section.

UV/IR relation

From the motivation as a geometrization of the RG flow and the metric (3.14) follows that the gauge theory energy E_{YM} of an object is related to the holographic coordinate z as

$$E = \frac{z}{L} E_{\text{YM}}, \quad (3.20)$$

where E is the energy in the bulk (as the time conjugate). Since $E_{\text{YM}} \sim 1/z$, UV physics $E_{\text{YM}} \rightarrow \infty$ is mapped to bulk processes at $z \rightarrow 0$ near the Minkowski boundary, and conversely, the IR limit $E_{\text{YM}} \rightarrow 0$ is related to the region $z \rightarrow \infty$.

The infinite extension $z \rightarrow \infty$ of the bulk geometry encodes excitations of arbitrary low energies in the CFT. Confining theories with a mass gap m can be realized through a smooth ending at some finite value $z_0 \sim 1/m$. As we will discuss below, the introduction of a BH with a horizon at z_h introduces a finite temperature $T \sim 1/z_h$.

Operator/field map

The spectra of the different theories in the AdS/CFT correspondence are matched through the operator/field map, which relates bulk fields to operators in the boundary gauge theory. In particular, this duality states that the boundary value ϕ_0 of some bulk field Φ acts as a source for the local field operator \mathcal{O} . In the strong form, the generating functionals are identified within the path integral formalism on both sides of the correspondence through their partition functions, i.e.

$$Z_{\mathcal{O}}[\phi_0(x)]_{\text{CFT}} = Z_{\Phi}[\phi_0(x)]_{\text{string}}. \quad (3.21)$$

Here, the partition function of the CFT is calculated w.r.t. the gauge theory action S as $Z_{\mathcal{O}}[\phi_0(x)]_{\text{CFT}} = \int \mathcal{D}\mathcal{O} \exp(-S + \int d^d x \mathcal{O}(x) \phi_0(x))$ in Euclidean signature. In the classical limit, the string theory partition function reduces by a saddle point approximation to the supergravity expression $Z_{\Phi}[\phi_0(x)]_{\text{string}} = e^{-S_{\text{SUGRA}}[\Phi[\phi_0]]}$ subject to the boundary condition

$$\phi_0(x) = \lim_{z \rightarrow 0} z^{\alpha_{\Phi}} \Phi(x, z). \quad (3.22)$$

The coefficient α_{Φ} depends on the boundary asymptotics of the bulk field Φ for a well-defined limit. Correlation functions can be calculated from this prescription via functional derivatives

$$\langle \mathcal{O}(x_1) \dots \mathcal{O}(x_n) \rangle = \frac{1}{Z_{\mathcal{O}}[0]_{\text{CFT}}} \frac{\delta^n}{\delta \phi_0(x_1) \dots \delta \phi_0(x_n)} Z_{\mathcal{O}}[\phi_0(x)]_{\text{CFT}} \Big|_{\phi_0=0}. \quad (3.23)$$

Using the gravitational side of the duality (3.21) for this task requires solving the supergravity equations of motion with appropriate boundary condition (3.22) and a systematic holographic renormalization procedure to cancel divergences. This corresponds to the calculation of tree level diagrams in AdS spacetime, which are known as *Witten diagrams*.

Based on this operator/field duality, one can see that the AdS bulk metric g_{MN} is dual to the energy-momentum tensor $T^{\mu\nu}$ of the boundary theory with $\alpha_g = 2$ in (3.22). A gauge field A_M in the bulk is mapped to a conserved current j^μ with $\alpha_A = 0$ and a bulk scalar ϕ is dual to the glueball operator $\text{Tr}(F^2)$.

Let us consider the latter case of a bulk scalar ϕ with mass m in more detail. By applying a Kaluza-Klein compactification, the supergravity fields in $\text{AdS}_5 \times S_5$ are dimensionally reduced to AdS_5 . For the more general case of an AdS_{d+1} spacetime, the relevant bulk action for ϕ is $S \sim -\frac{1}{2} \int dz d^d x \sqrt{-g} (g^{MN} \partial_M \phi \partial_N \phi + m^2 \phi^2)$ under negligence of higher order terms. The Klein-Gordon equation has two independent solutions near the boundary at $z \rightarrow 0$:

$$\phi(x, z) \sim \phi_0(x) z^{\Delta_-} + \phi_+(x) z^{\Delta_+} + \dots, \quad (3.24)$$

where Δ_\pm are the roots of

$$m^2 L^2 = \Delta(\Delta - d), \quad (3.25)$$

i.e.

$$\Delta_\pm = \frac{d}{2} \pm \sqrt{\frac{d^2}{4} + m^2 L^2}, \quad (3.26)$$

which satisfy $\Delta_- = d - \Delta_+$. The non-normalizable modes

$$\phi_0(x) \equiv \lim_{z \rightarrow 0} \phi(x, z) z^{-\Delta_-} = \lim_{z \rightarrow 0} \phi(x, z) z^{\Delta_+ - d} \quad (3.27)$$

are interpreted as the source of the dual scalar field theory operator \mathcal{O} with scaling dimension $\Delta \equiv \Delta_+$, i.e. $\alpha_\phi = \Delta - d$ in (3.22), while the normalizable mode ϕ_+ can be identified with the vacuum expectation value of \mathcal{O} . Eq. (3.25) represents the Klein-Gordon equation in Fourier space in the limit $z \rightarrow 0$ and provides a remarkable relation between the scaling dimension of \mathcal{O} and the mass of the dual supergravity field. Furthermore, Eq. 3.26 implies that the scalar is even stable for negative mass as long as the inequality

$$m^2 L^2 \geq -\frac{d^2}{4} \quad (3.28)$$

is satisfied, which is known as the *Breitenlohner-Freedman bound*.

Further remarks on this duality and generalizations in other spacetime dimensions etc. can be found, e.g., in the early review [53].

Finite temperature and chemical potential

The nonzero temperature case can be studied by introducing a black hole (or black brane) into an asymptotic AdS_{d+1} spacetime with an event horizon at some finite value $r = r_h$ or $z = z_h$. The same reasoning behind the duality (3.18) allows to identify the associated thermodynamic quantities with those of the CFT. In particular, the temperature T and entropy density s are given by the Hawking and Bekenstein formulas

$$T = \frac{\varkappa}{2\pi}, \quad s = \frac{1}{V} \frac{A_H}{4G_N^{(d+1)}}, \quad (3.29)$$

where \varkappa is the surface gravity, A_H the event horizon area and $G_N^{(d+1)}$ the Newton constant in $d + 1$ dimensions. Motivated by a generic quantum gravity path integral formalism, the temperature can also be calculated through an Euclidean continuation $t \rightarrow -it_E$ and requiring regularity at the horizon, such that t_E has a period $1/T$.

Adding a $U(1)$ gauge field A_M in the bulk gives rise to a conserved boundary current j^μ . In the limit $z \rightarrow 0$, the vector field A_M has the asymptotic behavior $A_\mu = a_\mu + b_\mu z^{d-2}$. The time component of the source $a_\mu(x)$ is related to the chemical potential μ via

$$\mu = \frac{a_t}{L} = \frac{1}{L} \lim_{z \rightarrow 0} A_t, \quad (3.30)$$

while b_t is proportional to the baryon number density n . The component A_t represents an electrostatic potential, i.e. one considers charged BH solutions. Similarly, a magnetic field could be turned on through the spatial components of A_μ .

Holographic entanglement entropy

The entanglement entropy for a boundary region \mathcal{A} of a d -dimensional CFT on $\mathbb{R}^{1,d-1}$ can be calculated holographically as

$$S_{\text{HEE}} = \frac{\text{Area}(\gamma_{\mathcal{A}})}{4G_N^{(d+1)}}. \quad (3.31)$$

The gravitational dual represents the area of the minimal surface in the bulk, which shares the boundary with \mathcal{A} . This concept, introduced in [54, 55], allows to study properties of strongly coupled field theories and to characterize phase transitions. Furthermore, deep connections between the emergence of spacetime itself and the entanglement of underlying quantum degrees of freedom are conjectured (see e.g. [56, 57]). We will give a detailed introduction in chapter 5 and apply this method to our holographic model.

4 Holographic model

This chapter contains our calculations of the holographic model at finite temperature and net baryon density. We use a EMD model, which was originally developed in [21]. This work was based on an adjustment to preliminary lattice data, which are quantitatively different to the most recent and consistent lattice QCD results in [11, 12]. The position for the CEP in [21] is thus not reliable any more and one aim of this thesis is to update the CEP coordinates. We also remark, that the original model was extended in [58], where dynamical effects have been considered. In [59–61], the bottom-up approach was adjusted to recent lattice data and equilibration effects and transport phenomena were analyzed. However, the structure of the phase diagram and updated CEP position were not yet addressed. We investigate these properties in this chapter. There is also plenty of related work, e.g. in [62–67], which use versions of the original model or similar approaches. Since these works adjust their model to a meson spectrum to explore diverse properties, they are not of relevance for analyses in this chapter. See also [68] for a study of the effect of a magnetic field on the QCD thermodynamics in a holographic approach.

Below, we first review the setup of the EMD model in section 4.1. The discussion follows [21] and [59]. The adjustment to the recent lattice data is described in section 4.2 and we discuss our result for the CEP and structure of the phase diagrams in section 4.3, based on [1].

4.1 Review of the holographic EMD model

The 5-dimensional EMD model is based on the action

$$S = \frac{1}{2\kappa_5^2} \int d^5x \sqrt{-g} \left(R - \frac{1}{2} \partial^\mu \phi \partial_\mu \phi - V(\phi) - \frac{f(\phi)}{4} F^2 \right), \quad (4.1)$$

where R is the Ricci scalar as the Einstein-Hilbert part and $V(\phi)$ is a potential describing the self-interaction of the real scalar (dilaton) ϕ . The field strength tensor $F_{\mu\nu} = \partial_\mu A_\nu - \partial_\nu A_\mu$ with the Abelian gauge field $A_\mu dx^\mu = \Phi dt$ is coupled to the dilaton via a dynamical strength function $f(\phi)$ (also called gauge kinetic function). κ_5 is the 5-dimensional gravitational constant and g represents the determinant of the metric $g_{\mu\nu}$. The dilaton potential breaks conformal invariance and thus mimics the effect of a running coupling constant as in QCD, while the F^2 term introduces a chemical potential through the holographic dictionary. We do not perform a renormalization procedure on the action itself and consider only classical equations of motion

(EoM). As discussed in [21, 59], a boundary term, counterterms or a Chern-Simons term are not necessary in this context. The EoM for the action (4.1) follow from

$$R_{\mu\nu} - \frac{1}{2}Rg_{\mu\nu} = T_{\mu\nu}, \quad (4.2)$$

$$\nabla_\mu [f(\phi)F^{\mu\nu}] = 0, \quad (4.3)$$

$$\nabla_\mu \nabla^\mu \phi = \frac{\partial V(\phi)}{\partial \phi} + \frac{1}{4} \frac{\partial f(\phi)}{\partial \phi} F^2, \quad (4.4)$$

where the energy-momentum tensor is given by

$$T_{\mu\nu} = \frac{1}{2} \left[\partial_\mu \phi \partial_\nu \phi - \frac{1}{2} g_{\mu\nu} \partial_\alpha \phi \partial^\alpha \phi - g_{\mu\nu} V(\phi) \right] + \frac{f(\phi)}{2} \left[F_{\mu\alpha} F_\nu^\alpha - \frac{1}{4} g_{\mu\nu} F^2 \right]. \quad (4.5)$$

Demanding an asymptotical AdS space for vanishing scalar, one has

$$V(\phi = 0) \equiv 2\Lambda = -\frac{12}{L^2}, \quad (4.6)$$

where L is the AdS length scale. The cosmological constant Λ is thus implicitly contained in the third term of the energy-momentum tensor. The explicit forms of $V(\phi)$ and $f(\phi)$ are specified in the next section such that thermodynamic results are in agreement with lattice data. We consider the coordinates (t, \vec{x}, r) with r as the holographic coordinate and the following metric ansatz

$$ds^2 = e^{2A(r)} (-h(r) dt^2 + d\vec{x}^2) + \frac{e^{2B(r)}}{h(r)} dr^2. \quad (4.7)$$

The boundary of the asymptotical AdS space is located at $r \rightarrow \infty$, and a black hole horizon is located at $r = r_H$, defined by a simple zero of the blackness function $h(r)$. Only the dynamics in the bulk direction is assumed, i.e. the dilaton and the zero-component of the gauge field (which is essentially the electrostatic potential) depend only on the radial coordinate:

$$\phi = \phi(r), \quad \Phi = \Phi(r). \quad (4.8)$$

The field equations and EoM then follow as

$$A'' - A'B' + \frac{1}{6}\phi'^2 = 0, \quad (4.9)$$

$$h'' + (4A' - B')h' - e^{-2A} f(\phi)\Phi'^2 = 0, \quad (4.10)$$

$$\Phi'' + (2A' - B')\Phi' + \frac{d \ln f(\phi)}{d\phi} \phi' \Phi' = 0, \quad (4.11)$$

$$\phi'' + \left(4A' - B' + \frac{h'}{h} \right) \phi' - \frac{e^{2B}}{h} \left(\frac{\partial V(\phi)}{\partial \phi} - \frac{1}{2} e^{-2A-2B} \Phi'^2 \frac{\partial f(\phi)}{\partial \phi} \right) = 0, \quad (4.12)$$

$$h(24A'^2 - \phi'^2) + 6A'h' + 2e^{2B} V(\phi) + e^{-2A} f(\phi)\Phi'^2 = 0 \quad (4.13)$$

(the prime means a derivative w.r.t. r).¹⁸ By integrating Eq. (4.11), it follows that there is a Gauss charge

$$Q_G(r) = f(\phi) e^{2A-B} \Phi', \quad (4.14)$$

which is radially conserved: $dQ_G/dr = 0$.¹⁹

The following near-boundary asymptotics in powers of $e^{-\alpha(r)} \equiv \exp[-\frac{r}{L\sqrt{h_0^\infty}} - A_0^\infty]$ are valid [21]:

$$h(r) = h_0^\infty + \dots, \quad (4.15)$$

$$A(r) = \alpha(r) + \dots, \quad (4.16)$$

$$\Phi(r) = \Phi_0^\infty + \Phi_2^\infty e^{-2\alpha(r)} + \dots, \quad (4.17)$$

$$\phi(r) = \phi_A e^{-(4-\Delta)\alpha(r)} + \phi_B e^{-\Delta\alpha(r)} + \dots. \quad (4.18)$$

In line with the AdS/CFT formalism, the expansion of ϕ assumes the boundary expansion of the potential

$$L^2V(\phi) = -12 + \frac{1}{2}[\Delta(\Delta - 4)]\phi^2 + \dots \quad \text{for } \phi \rightarrow 0, \quad (4.19)$$

where Δ is the scaling dimension of the field theory operator dual to the scalar ϕ with mass $m^2L^2 = \Delta(\Delta - 4)$.²⁰ In the far from horizon asymptotics (4.18), ϕ_A is the source and ϕ_B the expectation value of the dual boundary theory operator.

For the calculation of thermodynamic quantities we choose the gauge $\tilde{B}(\tilde{r}) = 0$, where the tilde denotes functions and coordinates associated with this gauge. The ansätze take the form

$$d\tilde{s}^2 = e^{2\tilde{A}(\tilde{r})} \left(-\tilde{h}(\tilde{r}) d\tilde{t}^2 + d\vec{\tilde{x}}^2 \right) + \frac{d\tilde{r}^2}{\tilde{h}(\tilde{r})}, \quad \tilde{\phi} = \tilde{\phi}(\tilde{r}), \quad \tilde{A}_\mu d\tilde{x}^\mu = \tilde{\Phi}(\tilde{r}) d\tilde{t}. \quad (4.20)$$

The boundary expansions in this gauge are [21]:

$$\tilde{h}(\tilde{r}) = 1 + \dots, \quad (4.21)$$

$$\tilde{A}(\tilde{r}) = \frac{\tilde{r}}{L} + \dots, \quad (4.22)$$

$$\tilde{\Phi}(\tilde{r}) = \tilde{\Phi}_0^\infty + \tilde{\Phi}_2^\infty e^{-2\tilde{r}/L} + \dots, \quad (4.23)$$

$$\tilde{\phi}(\tilde{r}) = e^{-(4-\Delta)\tilde{r}/L} + \dots. \quad (4.24)$$

To express all quantities in the original coordinates (t, \vec{x}, r) , one sets $ds^2 = d\tilde{s}^2$, $\phi(r) = \tilde{\phi}(\tilde{r})$

¹⁸Only the first four equations are independent: Eq. (4.13) is the zero-energy constraint and its derivative can be expressed by the other equations.

¹⁹There is also a radially conserved Noether charge $Q_N(r) = e^{2A-B}[e^{2A} h' - f(\phi)\Phi\Phi']$, which however is not important for our purposes. Using Eqs. (4.11) and Eq. (4.10) is then equivalent to $dQ_N/dr = 0$.

²⁰These boundary asymptotics correspond to a relevant operator with scaling dimension $\Delta < 4$ in the boundary theory. An example for different potential asymptotics associated to a marginal operator is given in [69].

and $A_\mu dx^\mu = \tilde{A}_\mu d\tilde{x}^\mu$. By comparing the boundary asymptotics, this implies [21, 59]

$$\tilde{t} = \phi_A^{1/(4-\Delta)} \sqrt{h_0^\infty} t, \quad \vec{\tilde{x}} = \phi_A^{1/(4-\Delta)} \vec{x}, \quad \frac{\tilde{r}}{L} = \alpha(r) - \ln \left(\phi_A^{1/(4-\Delta)} \right), \quad (4.25)$$

$$\tilde{h}(\tilde{r}) = \frac{h(r)}{h_0^\infty}, \quad \tilde{A}(\tilde{r}) = A(r) - \ln \left(\phi_A^{1/(4-\Delta)} \right), \quad \tilde{\Phi}(\tilde{r}) = \frac{\Phi(r)}{\phi_A^{1/(4-\Delta)} \sqrt{h_0^\infty}} \quad (4.26)$$

and specifically (from the last relation)

$$\tilde{\Phi}_0^\infty = \frac{\Phi_0^\infty}{\phi_A^{1/(4-\Delta)} \sqrt{h_0^\infty}}, \quad \tilde{\Phi}_2^\infty = \frac{\Phi_2^\infty}{\phi_A^{3/(4-\Delta)} \sqrt{h_0^\infty}}. \quad (4.27)$$

The thermodynamic quantities temperature T , entropy density s , baryo-chemical potential μ and baryon density n are now obtained as [21, 59]

$$T = \frac{\varkappa}{2\pi} = \frac{e^{\tilde{A}(\tilde{r}_H)} d\tilde{h}}{4\pi d\tilde{r}} \Big|_{\tilde{r}_H} = \frac{1}{L} \frac{1}{4\pi \phi_A^{1/(4-\Delta)} \sqrt{h_0^\infty}}, \quad (4.28)$$

$$s = \frac{1}{V} \frac{A_H}{4G_N^{(5)}} = \frac{2\pi}{\kappa_5^2} e^{3\tilde{A}(\tilde{r}_H)} = \frac{1}{\kappa_5^2} \frac{2\pi}{\phi_A^{3/(4-\Delta)}}, \quad (4.29)$$

$$\mu = \frac{1}{L} \lim_{\tilde{r} \rightarrow \infty} \tilde{\Phi}(\tilde{r}) = \frac{\tilde{\Phi}_0^\infty}{L} = \frac{1}{L} \frac{\Phi_0^\infty}{\phi_A^{1/(4-\Delta)} \sqrt{h_0^\infty}}, \quad (4.30)$$

$$n = \lim_{\tilde{r} \rightarrow \infty} \frac{\partial \mathcal{L}}{\partial(\partial_{\tilde{r}} \tilde{\Phi})} = -\frac{\tilde{\Phi}_2^\infty}{\kappa_5^2} = -\frac{1}{\kappa_5^2} \frac{\Phi_2^\infty}{\phi_A^{3/(4-\Delta)} \sqrt{h_0^\infty}}. \quad (4.31)$$

The temperature and entropy density follow from the black hole thermodynamics according to Bekenstein-Hawking (\varkappa is the surface gravity and A_H the event horizon area) while μ and n are given by the holographic dictionary.

Numerical solutions to the EoM are obtained by integrating Eqs. (4.9)-(4.12) from $r_H + \epsilon$ towards the boundary at $r \rightarrow \infty$. We choose $\epsilon = \mathcal{O}(10^{-6})$ to avoid the horizon as the singular point and set $r_H = 0$ (which is allowed by rescaling the r -coordinate). To determine the initial conditions at this point minimally above the horizon, a Taylor series $X(r) = \sum_{n=0}^{\infty} X_n(r-r_H)^n$ for any of the fields h, A, Φ, ϕ is plugged into the Eqs. (4.9)-(4.13) and every power of ϵ in the resulting equations is set to zero. The following assumptions are valid for this purpose:²¹

$$h_0 = 0, \quad h_1 = 1/L, \quad A_0 = 0, \quad \Phi_0 = 0. \quad (4.32)$$

As a consequence, a solution to the field equations is fully specified by $\phi_0 \equiv \phi(r_H)$ and $\Phi_1 \equiv \frac{\partial \Phi}{\partial r} \Big|_{r_H}$ as the only free parameters. Plugging the horizon expansion up to first order in the constraint equation (4.13) yields $A_1 = -\frac{L}{6} [2V(\phi_0) + f(\phi_0)\Phi_1^2]$. Demanding an asymptotically

²¹As explained in [21, 59], the first condition follows from the definition of the horizon as a simple zero, $h(r_H) \equiv 0$, and $h_1 = 1/L$ is achieved by rescaling t . Similarly, $A_0 = 0$ is obtained by rescaling (t, \vec{x}) . $\Phi_0 = 0$ is necessary for a well-defined integration measure Φdt at the horizon.

AdS space requires $A_1 > 0$. Taking into account $V(\phi_0) < 0$ and $f(\phi_0) > 0$, it follows that Φ_1 is bounded from above as $\Phi_1 < \Phi_1^{max} \equiv \sqrt{-\frac{2V(\phi_0)}{f(\phi_0)}}$. Applying the horizon expansion to the Gauss charge (4.14) gives $Q_G(r_H) = f(\phi_0)\Phi_1$, while the value at the boundary is $Q_G(r \rightarrow \infty) = -2f(0)\Phi_2^\infty/\sqrt{h_0^\infty}$ from (4.17). The conservation law implies

$$\Phi_2^\infty = -\frac{\sqrt{h_0^\infty}}{2f(0)}f(\phi_0)\Phi_1. \quad (4.33)$$

Computationally, we employed the horizon expansion up to fifth order and solved the field equations (4.9)-(4.12) using the function `odeint` implemented in `python`. The values for h_0^∞ , ϕ_A and Φ_0^∞ are extracted by fitting the numerical solutions to the boundary behavior in Eqs. (4.15)-(4.18) at large r . At intermediate steps, we set $\kappa_5 = L = 1$ and restore afterwards physical units by introducing dimensional scaling factors $\lambda_{T,s,\mu,n}$ as in [21, 58]. The scaling factors satisfy $\lambda_T = \lambda_\mu := 1/L$ and $\lambda_s = \lambda_n := 1/\kappa_5^2$ and accommodate the only two scales L and κ_5 appearing in the action (4.1). Together with Eq. (4.33), our final formulas for the thermodynamic quantities thus take the form

$$T = \lambda_T \frac{1}{4\pi\phi_A^{1/(4-\Delta)}\sqrt{h_0^\infty}}, \quad (4.34)$$

$$s = \lambda_s \frac{2\pi}{\phi_A^{3/(4-\Delta)}}, \quad (4.35)$$

$$\mu = \lambda_\mu \frac{\Phi_0^\infty}{\phi_A^{1/(4-\Delta)}\sqrt{h_0^\infty}}, \quad (4.36)$$

$$n = \lambda_n \frac{f(\phi_0)\Phi_1}{2f(0)\phi_A^{3/(4-\Delta)}}. \quad (4.37)$$

Based on this setup, the T - μ plane is uncovered with suitably chosen initial conditions (ϕ_0, Φ_1) . From the thermodynamic laws, the pressure follows by integrating $dp(T, \mu) = s(T, \mu)dT + n(T, \mu)d\mu$, with $p(0, 0) = 0$ and $T = 0, \mu = 0$ correspond to $\phi_0 \rightarrow \infty, \Phi_1 = 0$. (Details of that integral are discussed in the next sections.)

4.2 Adjustment to lattice QCD data at $\mu = 0$

The holographic model introduced in the previous section is supplemented by a specific form of the dilaton potential $V(\phi)$ and the gauge kinetic function $f(\phi)$. This bottom-up approach is adjusted to lattice QCD data at $\mu = 0$. Proper engineering of $V(\phi)$ determines the EoS at $\mu = 0$ and the phase transition type - in particular it allows to incorporate a FOPT (as for pure glue dynamics or QCD in the chiral limit(s)) or a crossover (as for 2+1 flavor QCD with physical quark masses). We refer to [3, 71, 72] for recent discussions and to [69, 73–77] for original investigations.

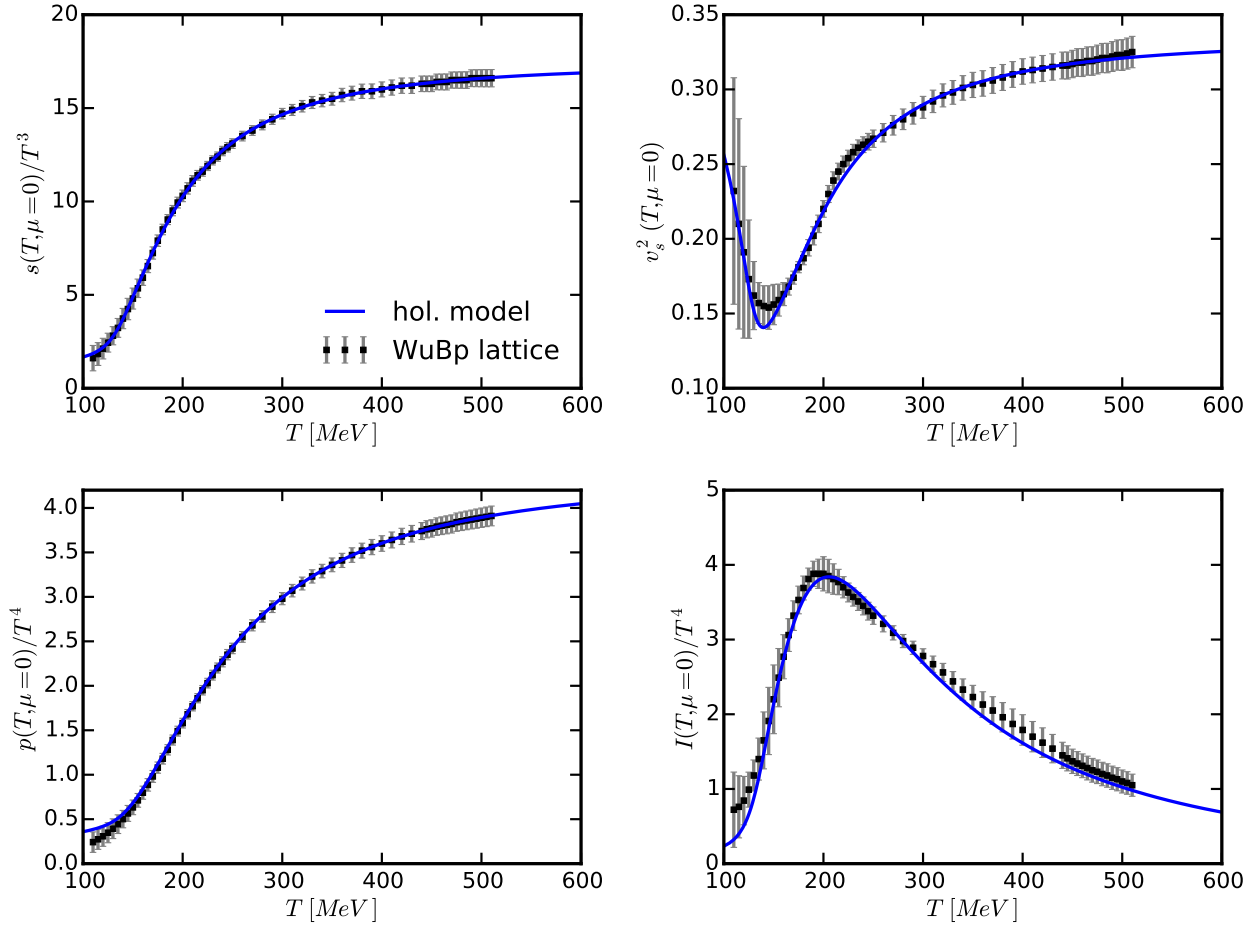


Figure 4.1: Equation of state of the updated holographic EMd model with parametrizations (4.38)-(4.40) as functions of T for $\mu = 0$: scaled entropy density (top left), speed of sound squared $v_s^2 = \frac{\partial \ln T}{\partial \ln s}$ (top right), scaled pressure (bottom left) and scaled trace anomaly (bottom right). Lattice results from [11] are displayed as symbols with error bars. Figure from [1].

We found the following dilaton potential by a fit of the scaled entropy density s/T^3 to the lattice data

$$L^2 V(\phi) = \begin{cases} -12 \exp \left\{ \frac{a_1}{2} \phi^2 + \frac{a_2}{4} \phi^4 \right\} & : \phi < \phi_m \\ a_{10} \cosh [a_4 (\phi - a_5)]^{a_3/a_4} \exp \left\{ a_6 \phi + \frac{a_7}{a_8} \tanh [a_8 (\phi - a_9)] \right\} & : \phi \geq \phi_m \end{cases} \quad (4.38)$$

with parameters

| | | | | | | |
|----------|---------|---------|--------|----------|--------|--------|
| ϕ_m | a_1 | a_2 | a_3 | a_4 | a_5 | (4.39) |
| 1.7058 | 0.2840 | -0.0089 | 0.7065 | 0.4951 | 0.1761 | |
| a_6 | a_7 | a_8 | a_9 | a_{10} | | |
| -0.0113 | -0.4701 | 2.1420 | 4.3150 | -10.0138 | | |

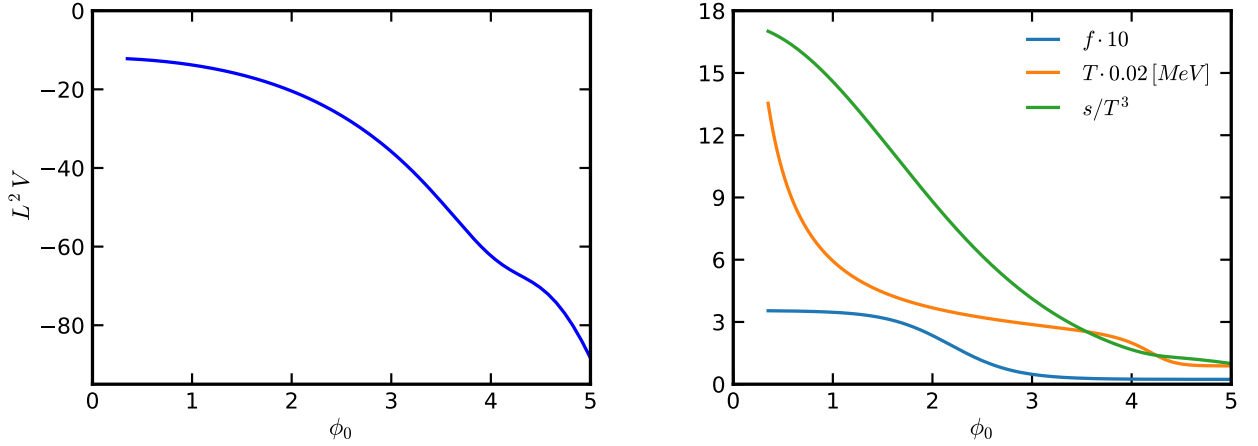


Figure 4.2: Left panel: Dilaton potential $L^2 V$ (4.38) with coefficients (4.39) as a function of the initial conditions ϕ_0 for the adjustment to lattice QCD data at $\mu = 0$. Right panel: Coupling function f (4.44) (blue curve) with coefficients (4.45), temperature T (orange curve) and scaled entropy density s/T^3 (green curve) as a function of the initial conditions ϕ_0 . The values of f and T are scaled for a suitable representation.

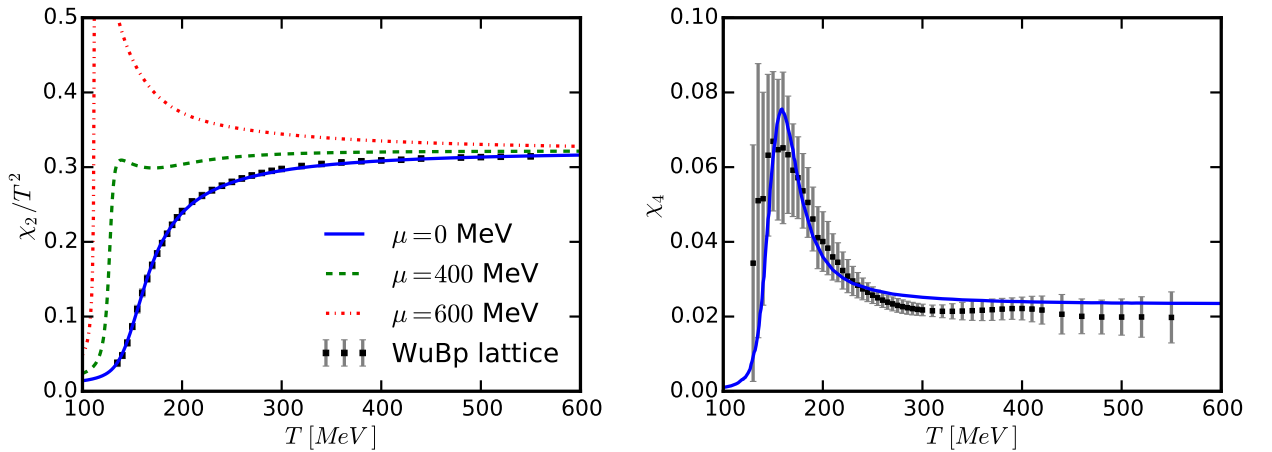


Figure 4.3: Second-order susceptibility χ_2/T^2 (left panel) and fourth-order susceptibility χ_4 (right panel) of the updated holographic EMd model with parametrizations (4.38)-(4.40) as function of T for different values of the chemical potential μ . Lattice results from [70] are displayed as symbols with error bars. Figure from [1].

implying $\Delta = 2(1 + \sqrt{1 - 3a_1})$ and the scaling factors

$$\frac{\lambda_T = \lambda_\mu}{1148.07 \text{ MeV}} \bigg| \frac{\lambda_s = \lambda_n}{(513.01 \text{ MeV})^3}. \quad (4.40)$$

We set $\Phi_1 = 0$ to numerically generate charged black hole solutions with initial conditions $\phi_0 \in [0.35, 5.0]$ at $\mu = 0$. The resulting equation of state is exhibited in Fig. 4.1. The lattice QCD results of [11] are consistent with the data in [12]; we select the tabulated results of [11] for the fit procedure and comparison.

The parameters (4.39) represent the best fit values that allow the most precise description of available lattice data within our model. In more detail, the parameters a_1 and a_2 of the dilation potential $V(\phi)$ for small ϕ_0 are used to mimic the asymptotic behavior near the boundary. The parameters a_3 - a_5 determine the thermodynamic behavior at large temperatures T . The exponential term with parameter a_6 dominates at large ϕ_0 , i.e. at low T . The parameters a_7 - a_9 modulate this asymptotics and are relevant to incorporate the crossover, e.g. the minimum of the speed of sound. Together, the parametrization (4.38) of $V(\phi)$ represents a monotonically decreasing function that avoids singular points as shown in Fig. 4.2 (left panel). The right panel in Fig. 4.2 shows the temperature and scaled entropy density as a function of the initial conditions ϕ_0 (orange and green curves). Both functions are monotonically decreasing and the limit $T \rightarrow 0$ corresponds to $\phi_0 \rightarrow \infty$. In appendix A we elaborate further details of this dilaton potential.

The pressure in the lower left panel in Fig. 4.1 is calculated from the thermodynamic relations as an integral over the entropy density w.r.t. the temperature. This is actually a pressure difference, similar to the discussion in [59], since the lower bound T_{low} of the integral is finite:

$$p(T, \mu = 0) \approx \Delta p(T, \mu = 0) = p(T, \mu = 0) - p(T_{low}, \mu = 0) = \int_{T_{low}}^T d\bar{T} s(\bar{T}, \mu = 0). \quad (4.41)$$

In our work, we put $T_{low} = 44 \text{ MeV}$ and the considered phase diagrams in the next section are for temperatures larger than $0.5T_{CEP} = 56 \text{ MeV}$. By choosing even smaller values for T_{low} , we checked that our value for T_{low} gives stable results in the relevant temperature range and thus the approximation is adequate. (The integrals converge quickly to the same values.) The interaction measure I then follows as $I = \epsilon - 3p = sT - 4p$ for $\mu = 0$.

The holographic model is completed by fixing $f(\phi)$. This is done by adjusting the EMD model to the quark number susceptibility from lattice QCD data. Susceptibilities are important fluctuation measures and defined as derivatives of the pressure, $\chi_i(T, \mu) \equiv \left. \frac{\partial^i p(T, \mu)}{\partial \mu^i} \right|_T$, $i = 2, 3, 4, \dots$. Odd susceptibilities $\chi_{3,5,\dots}$ vanish by CP invariance only at $\mu = 0$. An explicit formula for χ_2 at $\mu = 0$ follows from the definition

$$\chi_2(T, \mu = 0) = \lim_{\mu, \delta \rightarrow 0} \frac{n(T, \mu + \delta) - n(T, \mu)}{\delta} = \lim_{\mu \rightarrow 0} \frac{n(T, \mu)}{\mu}. \quad (4.42)$$

As outlined in [21, 59], the result can easily be derived from the relations (4.34)-(4.37) and contains only information of the functions at vanishing chemical potential. The equation for the dimensionless ratio χ_2/T^2 allows the matching of $f(\phi)$ to lattice data and reads

$$\frac{\chi_2(T, \mu = 0)}{T^2} = \frac{L}{16\pi^2 f(0)} \frac{s}{T^3} \frac{1}{\int_{r_H}^{\infty} dr \frac{e^{-2A(r)}}{f(\phi(r))}}. \quad (4.43)$$

We use the following ansatz for $f(\phi)$ in (4.43) to fit χ_2/T^2 to lattice data in [70]

$$f(\phi) = c_0 + c_1 \tanh [c_2(\phi - c_3)] + c_4 \exp [-c_5\phi] \quad (4.44)$$

with parameters

| | | | | | |
|--------|---------|--------|--------|--------|----------|
| c_0 | c_1 | c_2 | c_3 | c_4 | c_5 |
| 0.1892 | -0.1659 | 1.5497 | 2.1820 | 0.6219 | 112.7136 |

(4.45)

Fig. 4.3 shows the resulting susceptibilities at $\mu = 0$ (blue curves). The last term $c_4 e^{-c_5\phi}$ in Eq. (4.44) with $c_5 \approx 100$ as fit parameter is a delta function like contribution and puts significantly weight for $\phi \rightarrow 0$, i.e. for large values of r near the boundary. Hence, the integrand in Eq. (4.43) is continuously changed and the last term in $f(\phi)$ has the overall effect similar to a normalization factor for χ_2/T^2 , which allows to circumvent additional independent scales λ_μ and λ_n as in [21, 58]. Since the initial conditions in our phase diagrams are chosen for $\phi_0 > 0.35$, the last term in $f(\phi)$ is highly suppressed in this range and the thermodynamic behavior is dominated by the tanh-term in (4.44) (see blue curve in the right panel of Fig. 4.2). As outlined in [1], the fourth-order susceptibility χ_4 is calculated by applying smoothed spline derivatives w.r.t. $n(\mu, T = \text{const})$ curves. The robustness of this numerical procedure was verified for different smoothing conditions. Results for χ_2/T^2 at finite μ are obtained similarly without smoothing technique. The adjustment of χ_2/T^2 in the left panel of Fig. 4.3 to the lattice data represents an input, while the values for χ_4 in the right panel are the result of the holographic EMD model. Since both functions are in very good agreement within lattice uncertainties, one may be confident to transport the information from $\mu = 0$ to finite chemical potential and to make robust predictions within the framework of this holographic EMD model based on the concrete realization described in this section.

4.3 Holographic QCD phase diagrams

In this section, we describe the results of the holographic EMD model at finite chemical potential and density. The initial conditions for the numerical generation of charged BH solutions are $\phi_0 \in [0.35, 4.5]$ and $\Phi_1/\Phi_1^{max}(\phi_0) \in [0, 0.755]$. These input values uncover the $T-\mu$ plane as shown in Fig. 4.4. Numerically generated BH solutions are represented by dots. The colors indicate the sign of the determinant of the susceptibility matrix

$$J \equiv \det \mathcal{S} = \frac{\partial(s, n)}{\partial(T, \mu)} = \frac{\chi_2 C_n}{T}. \quad (4.46)$$

The last equality follows from standard thermodynamic relations (C_n is the heat capacity at constant baryon density) and shows that negative values for J correspond to thermodynamically unstable states.

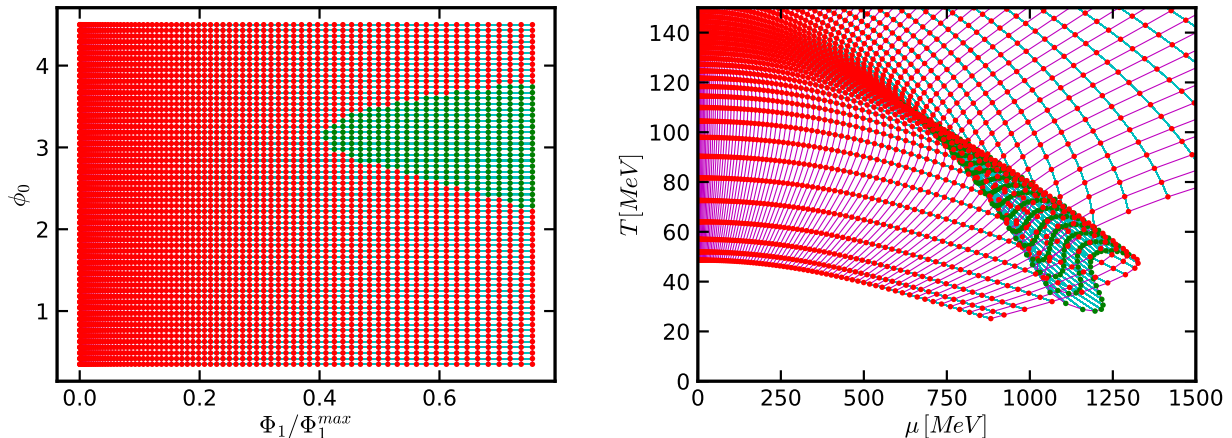


Figure 4.4: Initial conditions for numerically charged black hole solutions (left panel) and resulting location in the $T-\mu$ plane (right panel, excerpt). Red dots represent black hole solutions with a positive sign of the determinant J in (4.46), while green dots mark a negative sign. Curves of constant ϕ_0 and Φ_1/Φ_1^{max} are connected by thin lines.

cally unstable solutions (green dots in Fig. 4.4) whereas thermodynamically stable phases have $J > 0$ (red dots in Fig. 4.4). The determinant (4.46) is calculated by a finite difference approximation as in [21] and allows a rough approximation for the CEP position: The green dots in the right panel of Fig. 4.4 indicate an unstable branch with multivalued thermodynamic functions that terminates in a CEP at about $T_{CEP} \approx 110$ MeV and $\mu_{CEP} \approx 600$ MeV.

To determine the phase structure, we need to identify initial conditions (ϕ_0, Φ_1) , which result in constant temperatures (but are functions of the other thermodynamic quantities s , μ and n). We do so by generating contour plots of constant temperature in the (ϕ_0, Φ_1) plane with a relatively small number of numerical BH solutions. These curves are unique and used as an approximate input for a minimization algorithm that determines the initial conditions for $T = \text{const}$ curves with an accuracy of 10^{-8} MeV. On every $T = \text{const}$ line (which we displace in steps of 1 MeV), we calculate the pressure (as the relevant thermodynamic potential) as an integral over the baryon density w.r.t. the chemical potential:

$$p(T = \text{const}, \mu) = \int_0^\mu d\bar{\mu} n(T = \text{const}, \bar{\mu}) + p(T = \text{const}, \mu = 0). \quad (4.47)$$

The integration constant $p(T = \text{const}, \mu = 0)$ is taken from the previous calculation at $\mu = 0$ in (4.41) and no further approximation is necessary here. In case of a FOPT at $T < T_{CEP}$, the baryon density as a function of the chemical potential, i.e. $n(\mu, T = \text{const})$, is multivalued (S shape) and thus the pressure exhibits a typical loop. Then, the critical chemical potential μ_c , where the FOPT takes place, can be uniquely determined by the thermodynamic stability criterion (stable phases are those with highest pressure) as the intersection point of the low-temperature and high-temperature pressure branches. We can also simply identify unstable and metastable phases by this procedure.

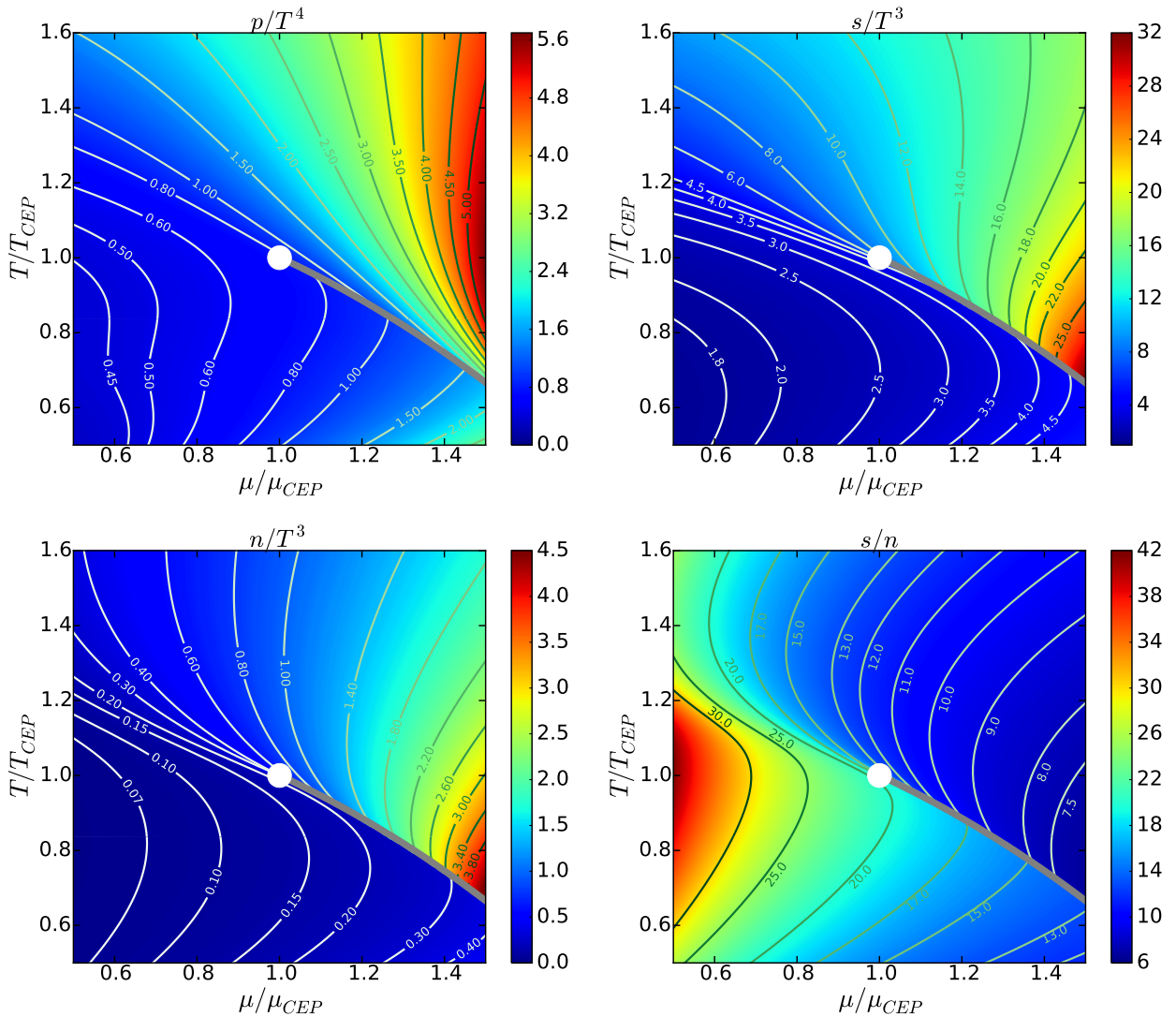


Figure 4.5: Contour plots of scaled pressure (top left), scaled entropy density (top right), scaled baryon density (bottom left), and entropy-to-baryon ratio (bottom right) over the scaled $T - \mu$ plane for the updated holographic EMD model. The position of the CEP is marked by a white dot and the FOPT curve is displayed as grey line. Figure from [1].

This construction results in the phase diagram in Fig. 4.5, where quantities in the thermodynamically stable phase are shown in several variants over the $T - \mu$ plane. The position of the CEP is

$$T_{CEP} = (111.5 \pm 0.5) \text{ MeV} \quad \text{and} \quad \mu_{CEP} = (611.5 \pm 0.5) \text{ MeV}. \quad (4.48)$$

The uncertainties are determined by the numerical calculation of lines of $T = \text{const}$ as discussed above and similarly also for $\mu = \text{const}$. The FOPT curve is signaled by a kinky behavior of the pressure (top left panel) and a discontinuous jump of the entropy density (top right panel), baryon density (bottom left panel) and entropy-to-baryon ratio (bottom right panel). More precisely, the entropy and baryon density jump towards larger values across the FOPT curve with increasing temperature or chemical potential, whereas the entropy-to-baryon ratio

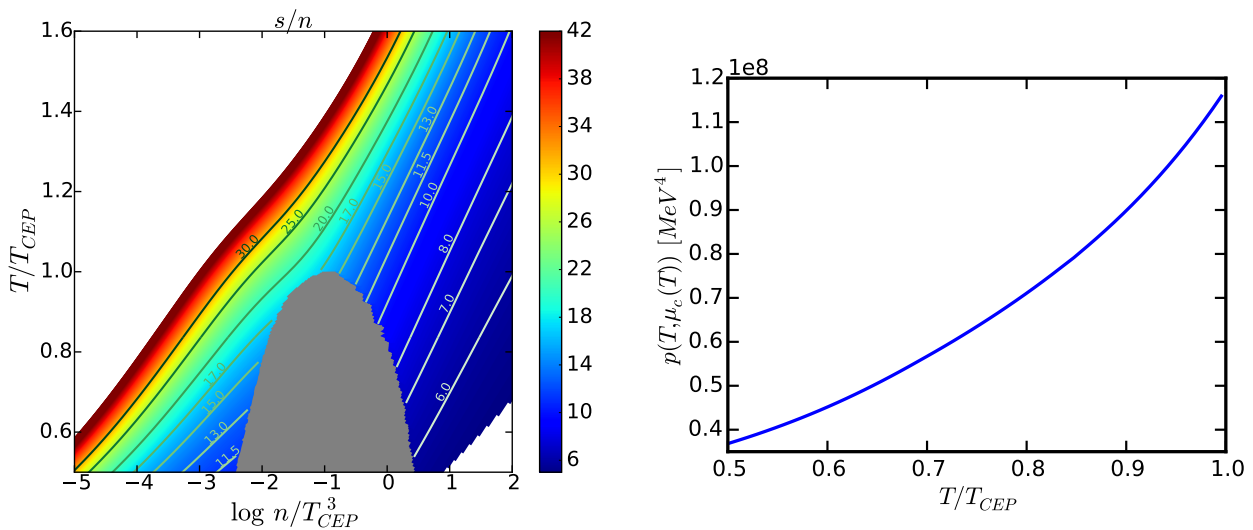


Figure 4.6: Left panel: Contour plot of entropy-to-baryon ratio over the $T/T_{CEP} - \log(n/T_{CEP}^3)$ plane for the updated holographic EMD model. The coexistence region is shown in grey. White regions indicate areas that are beyond the range of the colorbar. Right panel: Critical pressure $p_c = p(T, \mu_c(T))$ for the updated holographic EMD model. Figure from [1].

is pushed towards smaller values. Similar to the scaled entropy density and baryon density, the scaled pressure in Fig. 4.5 is increasing in μ -direction and the highlighted contour curves in this panel can be interpreted as scaled isobars, $p/T^4 = \text{const}$. Contour curves in the s/n -panel represent isentropes. In heavy-ion collisions, these represent paths of matter (gas or fluid) elements during the expansion, which is assumed to be adiabatic. The entropy-to-baryon ratio is decreasing towards finite values of μ .

The FOPT can further be specified as a gas-liquid (GL) one by the following observations: A comparison of the entropy-to-baryon ratios s/n on both sides of a point on the FOPT curve gives $s/n|_- > s/n|_+$, where the label $-(+)$ means approaching the FOPT curve from the left/dilute (right/dense) side. As emphasized in [1], this implies that the critical pressure $p_c(T) = p(T, \mu_c(T))$ increases with temperature (see right panel in Fig. 4.6) because the Clausius-Clapeyron relation

$$\frac{dp_c(T)}{dT} = \left(\left. \frac{s}{n} \right|_- - \left. \frac{s}{n} \right|_+ \right) \left(\left. \frac{1}{n} \right|_- - \left. \frac{1}{n} \right|_+ \right) > 0 \quad (4.49)$$

implies a positive slope of the curve $p(T, \mu_c(T))$ as a function of T . Furthermore, the FOPT curve is steeper than neighboring isobars. Both features are characteristic for a GL FOPT.

The quark number susceptibility at finite μ is another important quantity that probes the CEP. As exhibited in Fig. 4.3 (green and red curves in the left panel), χ_2/T^2 is pushed towards larger values with increasing chemical potential. At the CEP, an evolving maximum is transformed into a divergence.

The left panel in Fig. 4.6 elucidates the behavior of the isentropes as paths of adiabatically expanding and cooling pieces of matter in the $T - \log n$ plane. Isentropes enter the coexistence region on the deconfined/dense side and leave the FOPT curve on the confined/dilute side at lower temperature. Inside the two-phase coexistence region, which is depicted by a grey region, isentropes can be constructed by the lever rule, but are not displayed here. A detailed discussion of different FOPT types is presented in [78]. According to the nomenclature therein, the holographic EMd model is classified as type IA and represents a GL phase transition. We also calculated the phase diagram for the original model in [21] and found only incoming isentropes. This shows that the general structure of the phase diagram is dependent and rather sensitive on the concrete adjustment to lattice QCD data at $\mu = 0$.

The equation of state for different values of the baryo-chemical potential is explicitly shown in Fig. 4.7. The scaled pressure (top left panel), interaction measure (top right panel) and scaled entropy density (bottom right panel) are pushed towards higher values with increasing chemical potential. Here, the pressure at finite values of μ is calculated by Eq. (4.47) for a given value of T ; the interaction measure then follows as

$$I(T, \mu) = \epsilon(T, \mu) - 3p(T, \mu) = Ts(T, \mu) + \mu n(T, \mu) - 4p(T, \mu). \quad (4.50)$$

In particular, the maxima of the scaled interaction measure are attained for lower temperatures at larger values of μ . For $\mu \geq \mu_{CEP}$, both the scaled interaction measure and scaled entropy density jump across the FOPT. The bottom left panel in Fig. 4.7 shows the sound velocity squared v_s^2 for different values of the chemical potential μ . The following relation holds

$$v_s^2(T, \mu = \text{const}) \equiv \left. \frac{dp}{d\epsilon} \right|_{\mu} = \left(\left. \frac{T}{s} \frac{\partial s(T, \mu)}{\partial T} \right|_{\mu} + \left. \frac{\mu}{s} \frac{\partial n(T, \mu)}{\partial T} \right|_{\mu} \right)^{-1}, \quad (4.51)$$

where $dp = s dT + n d\mu$ and $d\epsilon = T ds + \mu dn$ follow from the first law of thermodynamics. For $\mu = \mu_{CEP}$, the sound velocity squared drops to zero, as typical for a second-order phase transition (cf. [80]). The holographic results are in reasonable agreement with lattice data at finite values of μ from [79] (shown as red symbols in Fig. 4.7) and support the described qualitative behavior.²²

In Fig. 4.8 (left panel), the holographic result for isentropes of constant s/n is explicitly compared to lattice QCD results [81] in the $T - \mu$ plane. The lattice data at finite values of μ are extrapolated from analytical calculations, i.e. a Taylor expansion in powers of μ/T is performed, where the coefficients in [81] are calculated at $\mu = 0$ up to sixth order. The holographic result describes well the pattern of isentropes at small μ but seems to deviate for larger values of μ . We however remark that the calculations performed in [81] involve some bound-

²²We point out that the available lattice data in [79] are not identical to the most recent data in [11, 12]. The latter however do not include similar curves for fixed finite values μ . We thus use the data from [79] for a comparison in Fig. 4.7.

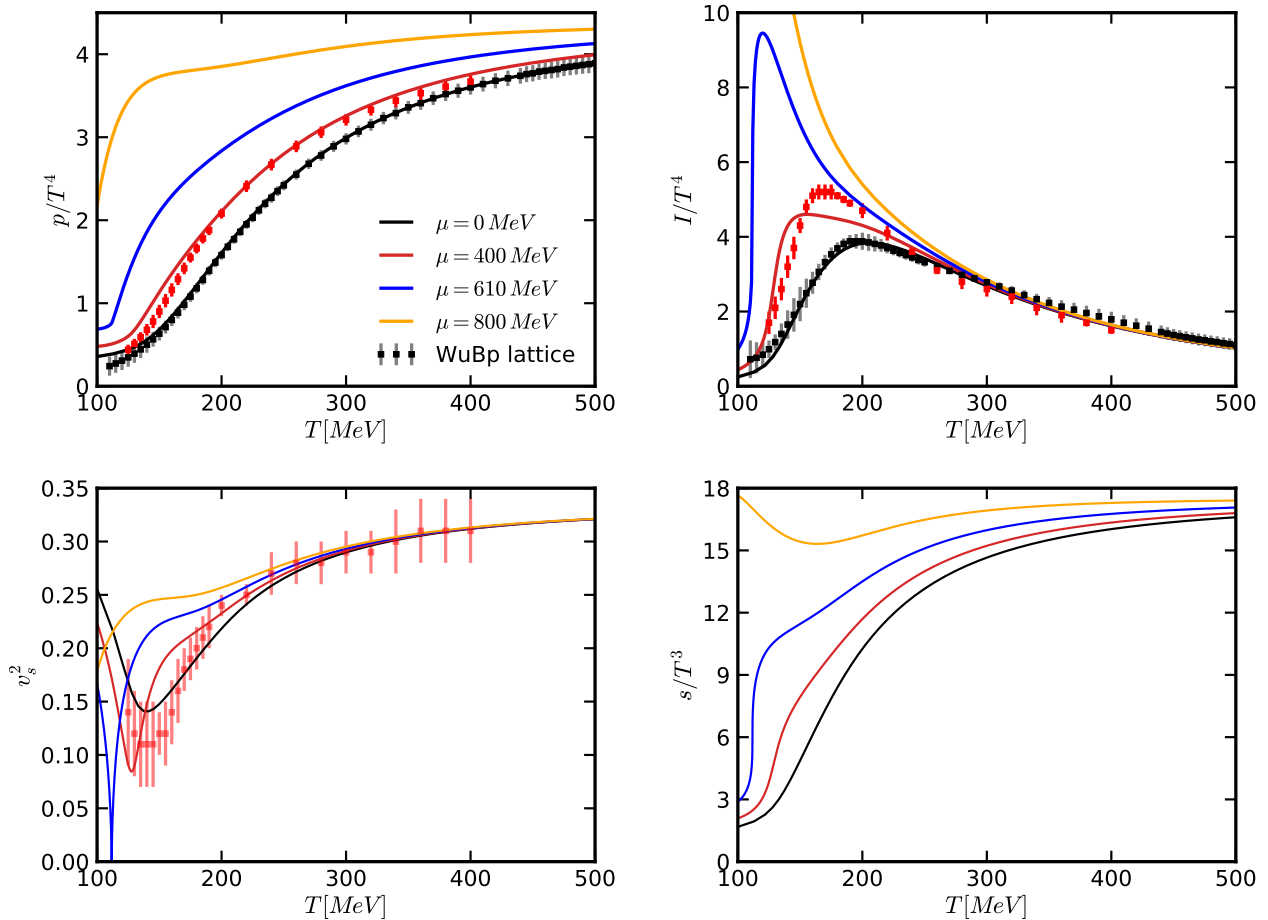


Figure 4.7: Equation of state of the updated holographic EMD model as functions of T for $\mu = 0$ and $\mu > 0$: scaled pressure (top left), scaled trace anomaly (top right), speed of sound squared (bottom left) and scaled entropy density (bottom right). Lattice results from [11] for $\mu = 0$ are displayed as black symbols with error bars and lattice data from [79] for finite values of μ are shown as red symbols with error bars.

ary conditions w.r.t. charge densities that we do not take into account in the EMD model. A direct comparison of lattice and holographic results might thus not be fully appropriate in this context. In addition, we stress that lattice data are only available for temperatures above 130 MeV. Hence, a comparison of the isentrope pattern at low temperatures and in the eventual CEP region is not possible. Results of a hadron resonance gas model in [81] do not seem to support the “outgoing” isentrope behavior at lower T as discussed above. We however emphasize that these findings are not (yet) supported by reliable lattice calculations and therefore only represent model calculations and/or extrapolations.

To summarize the above results, we explored the QCD phase diagram within a holographic EMD model, which is based on an adjustment to recent lattice QCD data at $\mu = 0$ and then transports the information to finite values of μ . As just stated, there are no lattice data available in the low-temperature regime $T \lesssim 100$ MeV and the CEP (4.48) is located in a temperature range near, but outside the range of lattice data for the EoS and susceptibilities.

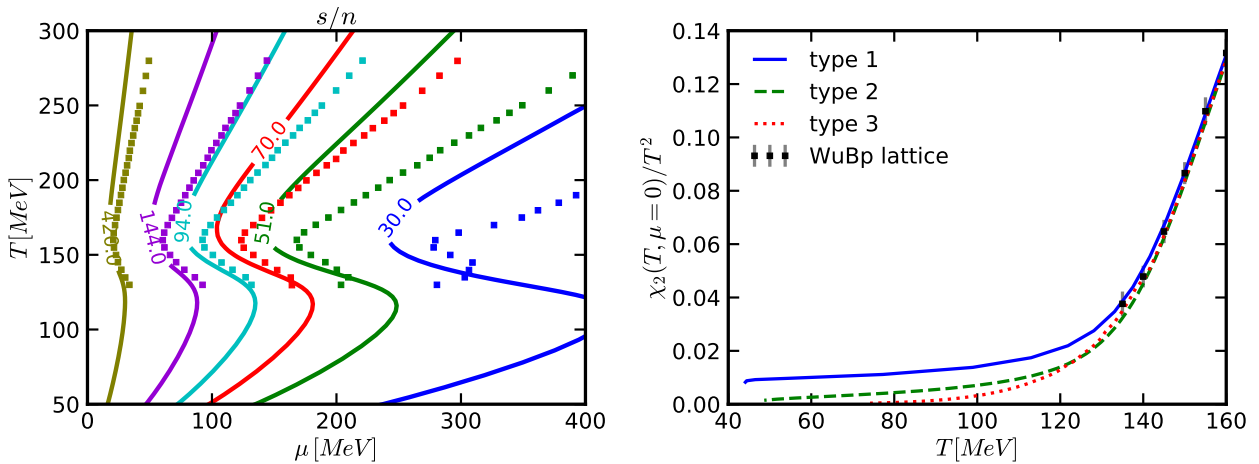


Figure 4.8: Left panel: Isentropes, i.e. curves of constant s/n , in the QCD phase diagram. The result of the holographic EMD model is shown as solid curves and corresponding lattice data from [81] are depicted as squares. Right panel: Different types of low-temperature asymptotics for the susceptibility χ_2/T^2 that are used to estimate the CEP accuracy.

For this reason, it is an important task to analyze the accuracy of the CEP position, i.e. the uncertainties in the T_{CEP} and μ_{CEP} coordinates that are consistent with lattice uncertainties. We proceed twofold. First, we estimated that parameter variations in the order of 0.8% for the dilaton potential (4.39) and 3% of the coupling function parameters (4.45) still provide a good description of the EoS and $\chi_{2,4}$ within the error band of the lattice results.²³ Second, we assumed different generic low-temperature asymptotics for the quark number susceptibility as shown in Fig. 4.8 (right panel). “type 1” corresponds to the best fit discussed above and exhibits a nearly constant behavior for χ_2/T^2 at low T . For the “type 2”, χ_2/T^2 is continued to zero nearly linear, which is achieved by a modified parametrization of the coupling function (4.44) at large ϕ . For “type 3”, we additionally perform a Taylor expansion of the dilaton potential (4.38) up to second order around $\phi \approx 3.13$ and use this series expansion for large values of ϕ , i.e. low temperatures T . Taking different permutations of parameter variations and low-temperature asymptotics into account, we find that T_{CEP} is maximally varied in the order of 5 MeV and μ_{CEP} in the order of 50 MeV. This corresponds to moderate changes of approximately 5% and 8% respectively. Our final prediction for the CEP in the holographic QCD phase diagram hence is

$$T_{CEP} = (112 \pm 5) \text{ MeV} \quad \text{and} \quad \mu_{CEP} = (612 \pm 50) \text{ MeV}. \quad (4.52)$$

We remark that types 2 and 3 of the additional asymptotics are accompanied with numerical instabilities at large μ . It is therefore not possible to study the effect of these asymptotics on the structure of the phase diagram.

²³Since there are multiple parameters, we do not consider individual parameter changes. Instead, we estimate the maximal deviation by collectively decreasing or increasing the coefficients by the listed amount.

5 Entanglement Entropy

This chapter is devoted to the study of entanglement entropy in our holographic EMD model. The main aim is to analyze the capability of entanglement entropy to characterize the different structures in the QCD phase diagram. An introduction into the concept of entanglement entropy as a widely used concept in quantum mechanics and QFT is given in section 5.1. This discussion follows the reviews [82, 83] and [43, 84]. Here, we calculate the entanglement entropy holographically, i.e. based on the gauge/gravity duality as outlined in section 5.2. The resulting phase diagram is discussed in section 5.3 and compared to its thermodynamic counterpart. Some aspects that quantify the critical behavior near the CEP are analyzed in section 5.4. The discussion in these latter sections is based on [2].

5.1 General aspects of entanglement entropy

Entanglement is a unique property of quantum mechanical systems compared to classical systems. In general, a quantum mechanical state is called entangled if it is inseparable. To elaborate this definition in more detail, we first consider pure states. Assuming two systems \mathcal{A} and \mathcal{B} with Hilbert spaces $\mathcal{H}_{\mathcal{A}}$ and $\mathcal{H}_{\mathcal{B}}$, the total Hilbert space is the tensor product $\mathcal{H} = \mathcal{H}_{\mathcal{A}} \otimes \mathcal{H}_{\mathcal{B}}$. States in $\mathcal{H}_{\mathcal{A}}$ can be represented as $|\psi\rangle_{\mathcal{A}} = \sum_i c_i^{\mathcal{A}} |i\rangle_{\mathcal{A}}$, where $\{|i\rangle_{\mathcal{A}}\}$ is a basis in $\mathcal{H}_{\mathcal{A}}$ and similarly $|\psi\rangle_{\mathcal{B}} = \sum_j c_j^{\mathcal{B}} |j\rangle_{\mathcal{B}}$ for states in $\mathcal{H}_{\mathcal{B}}$. A state $|\psi\rangle_{\mathcal{AB}} = \sum_{i,j} c_{ij} |i\rangle_{\mathcal{A}} \otimes |j\rangle_{\mathcal{B}}$ in \mathcal{H} is separable if the coefficients satisfy $c_{ij} = c_i^{\mathcal{A}} c_j^{\mathcal{B}}$, otherwise the state would be inseparable and thus entangled. An equivalent definition holds for mixed states (ensembles) w.r.t. the separability of the density matrices of the subsystems.

The simplest example for an entangled pure state can be constructed from a two-qubit system with Hilbert space $\mathcal{H} = \mathcal{H}_{qubit} \otimes \mathcal{H}_{qubit} = \text{lin}\{|00\rangle, |01\rangle, |10\rangle, |11\rangle\}$.²⁴ Then, the superposition $\frac{1}{\sqrt{2}}(|01\rangle - |10\rangle)$ is a correlated state that cannot be separated into single qubit components and hence the state is entangled.

An important non-local observable for the quantification of entanglement in pure states is the entanglement entropy. Entanglement entropy can be used for several purposes, e.g. to characterize phases, as an order parameter for phase transitions and as a measure of degrees of freedom or quantum information in diverse physical systems. Some of these properties and applications are discussed e.g. in [85–91]. For the definition of entanglement entropy we assume

²⁴We use the common notation $|i\rangle_{\mathcal{A}} \otimes |j\rangle_{\mathcal{B}} \equiv |ij\rangle$ here.

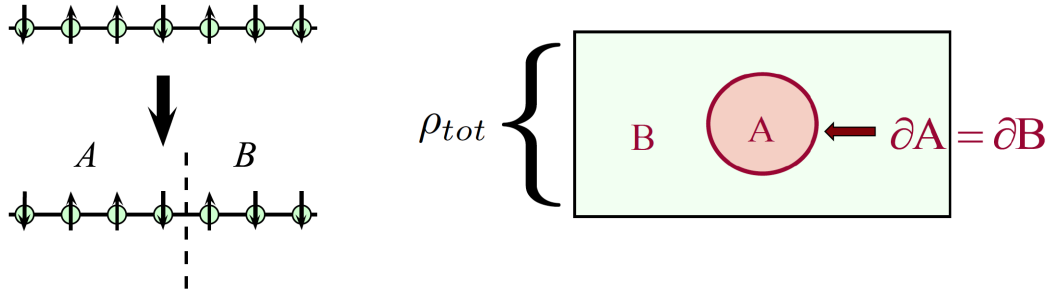


Figure 5.1: Separation of a quantum mechanical system into a subsystem \mathcal{A} and its complement \mathcal{B} for the definition of entanglement entropy. Typical examples include a spin chain (left panel) and a spatial bipartitioning of a QFT at a constant time slice (right panel). Figures adapted from [82] and [84].

a quantum mechanical system which is described by the density operator $\rho_{tot} = |\Psi\rangle\langle\Psi|$, where $|\Psi\rangle$ is a pure state. The system is divided into a subsystem \mathcal{A} and its complement \mathcal{B} . An illustration of this process for two examples is shown in Fig. 5.1. The entanglement entropy of \mathcal{A} is now defined as the von Neumann entropy

$$S_{\mathcal{A}} := -\text{Tr}_{\mathcal{A}} \rho_{\mathcal{A}} \ln \rho_{\mathcal{A}} \quad (5.1)$$

for the reduced density matrix $\rho_{\mathcal{A}} = \text{Tr}_{\mathcal{B}} \rho_{tot}$. While the von Neumann entropy for ρ_{tot} vanishes, $S_{\mathcal{A}}$ can be nonzero and quantifies the entanglement or “quantumness” of the state.

In the aforementioned example of the two-qubit system, one can easily show that the separable product state $|\Psi\rangle = \frac{1}{2}(|1\rangle_{\mathcal{A}} + |0\rangle_{\mathcal{A}}) \otimes (|1\rangle_{\mathcal{B}} + |0\rangle_{\mathcal{B}})$ has vanishing entanglement entropy, $S_{\mathcal{A}} = 0$, while the entangled state $|\Psi\rangle = \frac{1}{\sqrt{2}}(|01\rangle - |10\rangle)$ gives $S_{\mathcal{A}} = \ln 2$.

Entanglement entropy obeys some important relations and properties that we want to discuss in the following (without derivations). To begin with, entanglement entropy is not an extensive quantity. This is implied by the relation

$$S_{\mathcal{A}} = S_{\mathcal{B}}, \quad (5.2)$$

which is valid for the conditions mentioned above (e.g. for a ground state at zero temperature). For three non-interacting subsystems \mathcal{A} , \mathcal{B} and \mathcal{C} , the following strong subadditivity inequalities are valid:

$$S_{\mathcal{A}+\mathcal{B}+\mathcal{C}} + S_{\mathcal{B}} \leq S_{\mathcal{A}+\mathcal{B}} + S_{\mathcal{B}+\mathcal{C}}, \quad (5.3)$$

$$S_{\mathcal{A}} + S_{\mathcal{C}} \leq S_{\mathcal{A}+\mathcal{B}} + S_{\mathcal{B}+\mathcal{C}}. \quad (5.4)$$

Choosing the empty set for \mathcal{B} in (5.3) (and renaming $\mathcal{C} \rightarrow \mathcal{B}$) yields the subadditivity relation

$$S_{\mathcal{A}+\mathcal{B}} \leq S_{\mathcal{A}} + S_{\mathcal{B}}, \quad (5.5)$$

which motivates the definition of the mutual information $I(\mathcal{A}, \mathcal{B})$ as²⁵

$$I(\mathcal{A}, \mathcal{B}) := S_{\mathcal{A}} + S_{\mathcal{B}} - S_{\mathcal{A}+\mathcal{B}} \geq 0. \quad (5.6)$$

Entanglement entropy in d -dimensional QFTs is defined as in (5.1) on a $(d-1)$ -dimensional spatial manifold at constant time with a submanifold \mathcal{A} and its complement \mathcal{B} . The result is divergent and takes the general form

$$S_{\mathcal{A}} = c_0 \frac{\text{Area}(\partial\mathcal{A})}{\epsilon^{d-2}} + \text{subleading terms}, \quad (5.7)$$

where ϵ is a cutoff such that $\epsilon \rightarrow 0$ corresponds to the UV limit, $\partial\mathcal{A}$ is the boundary of the submanifold \mathcal{A} and the coefficient c_0 depends on the specific QFT. This equation looks similar to the Bekenstein entropy and is the reason why entanglement entropy was historically also considered in the context of BH entropy. In this context, it was found that entanglement entropy can be interpreted as the contribution stemming from quantum corrections to the BH entropy in the presence of matter fields (see [82] and references therein for details). The area law (5.7), however, is not true in general. For even d , there are additional logarithmic terms of the form

$$S_{\mathcal{A}} = \dots + c_d \ln \left(\frac{L}{\epsilon} \right) + \dots, \quad (5.8)$$

where L is the characteristic length scale of $\partial\mathcal{A}$. In particular for a two-dimensional CFT with central charge c , the leading divergence in (5.7), which is proportional to $(L/\epsilon)^{d-2}$, vanishes and one can derive the analytical result

$$S_{\mathcal{A}} = \frac{c}{3} \ln \frac{l}{\epsilon} \quad (5.9)$$

for the subsystem \mathcal{A} with length l .

An explicit calculation of entanglement entropy in a QFT can be performed with the so-called replica-trick. It allows to rewrite the definition of the entanglement entropy as

$$S_{\mathcal{A}} = -\frac{\partial}{\partial n} \ln \text{Tr}_{\mathcal{A}} \rho_{\mathcal{A}}^n \Big|_{n=1} = -\frac{\partial}{\partial n} \text{Tr}_{\mathcal{A}} \rho_{\mathcal{A}}^n \Big|_{n=1}. \quad (5.10)$$

The validity of this relation can easily be seen by rewriting $\ln \text{Tr}_{\mathcal{A}} \rho_{\mathcal{A}}^n = \ln (\sum_i \lambda_i^n)$ with the eigenvalues λ_i of $\rho_{\mathcal{A}}$. Differentiating w.r.t. n then gives $-\frac{\partial}{\partial n} \ln \text{Tr}_{\mathcal{A}} \rho_{\mathcal{A}}^n \Big|_{n=1} = -\frac{\sum_i \lambda_i^n \ln \lambda_i}{\sum_i \lambda_i^n} \Big|_{n=1} = -\frac{\sum_i \lambda_i \ln \lambda_i}{\sum_i \lambda_i} = -\sum_i \lambda_i \ln \lambda_i = -\frac{\partial}{\partial n} \text{Tr}_{\mathcal{A}} \rho_{\mathcal{A}}^n \Big|_{n=1} = -\text{Tr}_{\mathcal{A}} \rho_{\mathcal{A}} \ln \rho_{\mathcal{A}}$, where we used the normalization $\text{Tr}_{\mathcal{A}} \rho_{\mathcal{A}} = \sum_i \lambda_i = 1$ of the density matrix. Therefore, the quantity that needs to be evaluated for a given QFT is $\text{Tr}_{\mathcal{A}} \rho_{\mathcal{A}}^n$, which can be done in the path integral formalism as an integral on a Riemann surface with n sheets. For an arbitrary interacting QFT, this task is notoriously difficult or even impossible and only a few analytical results are known. For

²⁵The symbols I and L appearing in this chapter must not be mixed with the notation in chapter 4.

example, in a two-dimensional CFT, the general result is given in (5.9). On the other side, the holographic method to calculate entanglement entropy, as explained in the next section, allows computations even for strongly coupled QFTs and thus provides a promising approach to explore properties of entanglement entropy in higher dimensions.

5.2 Holographic entanglement entropy in the EMd model

The dual holographic description of entanglement entropy (HEE) was proposed by Ryu and Takayanagi [54, 55] in the context of the AdS/CFT correspondence. It relates the entanglement entropy of a CFT with a given entangling area to the associated minimal surface in the bulk of AdS spacetime. (See the left panel in Fig. 5.2 for a pictorial representation.) This concept inspired numerous investigations in several fields. For example, HEE was calculated to study the Van der Waals-like phase transition in charged Reissner-Nordström-AdS black holes [92–94] and massive [95] or Weyl [96] gravity. Other studies showed that HEE can also be used to characterize thermalization processes [97, 98]. In the context of the gravity/condensed matter correspondence [99], HEE was analyzed in studies of holographic superconductors [100–105] and metal-insulator transitions [106–108]. A recent proposal [109] argues that HEE can even be measured in an analog system on a quantum simulator in the context of tensor networks. The holographic interpretation of entanglement entropy thus allows interesting investigations in physical systems, where the field theoretical calculation is not applicable and hence can be used to study strongly coupled systems or quantum gravitational effects.

Most importantly, HEE was also used as a probe of confinement in large- N_c gauge theory duals: The authors of [110] calculated the minimal surface in dependence of the width of the entangling region and observed the change from a connected to a disconnected surface, which they interpreted as the confinement-deconfinement transition. Further studies showed a similar behavior for several background geometries [111–115], and lattice calculations for non-Abelian gauge theories could also confirm this property [116–118]. The following analysis is inspired by the work of Zhang [119], in which the author used HEE to characterize the different phases in a holographic bottom-up model [76, 120] that mimics the QCD EoS at vanishing chemical potential. In contrast to the previously mentioned references, the calculation therein is performed for a fixed boundary area but in dependence on the temperature. Here, we extend these calculations for our holographic EMd model to explore the capability of HEE to characterize the different phases in the $T-\mu$ plane, in particular the existence of the CEP in the QCD phase diagram.

The precise statement of the Ryu–Takayanagi prescription [54, 55] is that the holographic dual for the entanglement entropy (5.1) in a CFT $_d$ on $\mathbb{R}^{1,d-1}$ is given by

$$S_{\text{HEE}} = \frac{\text{Area}(\gamma_{\mathcal{A}})}{4G_N^{(d+1)}}. \quad (5.11)$$

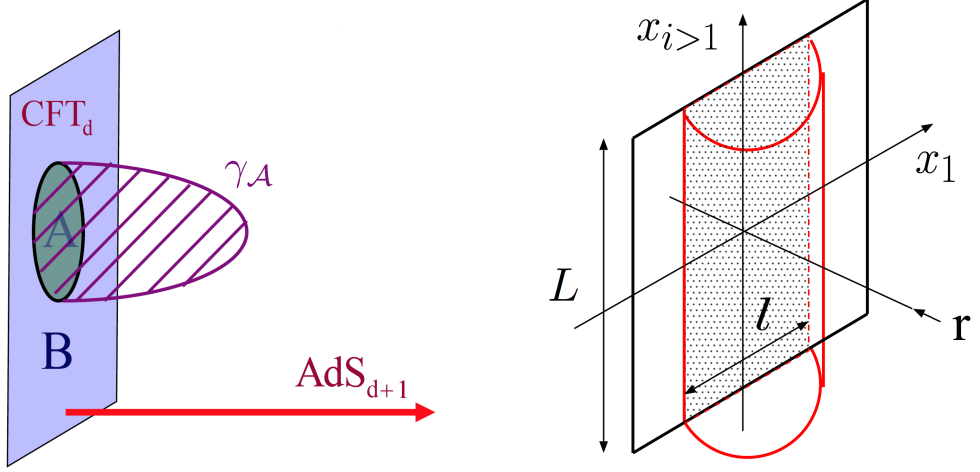


Figure 5.2: Left panel: Illustration of the definition of holographic entanglement entropy (HEE) as a minimal surface in the bulk of AdS spacetime. Right panel: Geometrical setup of the minimal surface for a rectangular strip on the boundary as the entangling area. Figures adapted from [84].

Here, $\gamma_{\mathcal{A}}$ represents the static minimal surface in AdS_{d+1} whose boundary satisfies $\partial\gamma_{\mathcal{A}} = \partial\mathcal{A}$ and $G_N^{(d+1)}$ is the $d+1$ dimensional Newton constant (cf. left panel in Fig. 5.2 for this setup). Due to the hyperbolic properties of the AdS spacetime, the HEE is infinite and the leading divergence satisfies the same area law (5.7) as in the CFT case. In the original proposal, this quantity was calculated for AdS_3 spacetime and it was shown that the result indeed agrees with the known formula (5.9) for the identification $c = 3/(2G_N^{(3)})$ (at unity curvature radius). Similarly, one can also show that HEE satisfies the (strong) subadditivity relations (5.3)-(5.5). We refer to [82, 83] for heuristic arguments regarding the derivation of the holographic formula, which, however, are not relevant for the following discussions.

For the present analysis, we assume a fixed rectangular strip shape on the boundary at $r = \infty$ as the entangling area

$$\mathcal{A}: \quad x_1 \in [-l/2, l/2], \quad x_2, x_3 \in [-L/2, L/2]. \quad (5.12)$$

Requiring translation invariance with $L \gg l$, the minimal surface can be parameterized by the single function $r = r(x_1)$. (See the right panel in Fig. 5.2 for this configuration.) To calculate the minimal surface area, the induced metric on the static minimal surface is needed, which is given by

$$ds_{\gamma_{\mathcal{A}}}^2 = \left(e^{2A} + \frac{r'^2}{h} \right) dx_1^2 + e^{2A} (dx_2^2 + dx_3^2), \quad (5.13)$$

where a prime denotes a derivative w.r.t. x_1 . The formula (5.11) for the HEE then yields

$$S_{\text{HEE}} = \frac{1}{4} \int dx_1 dx_2 dx_3 \sqrt{\gamma} = \frac{V_2}{2} \int_0^{l/2} dx_1 e^{2A(r)} \sqrt{e^{2A(r)} + \frac{r'^2}{h(r)}}. \quad (5.14)$$

Here, we set the Newton constant to unity, V_2 is defined as $V_2 \equiv \int dx_2 dx_3$, and γ is the determinant of the induced metric on $\gamma_{\mathcal{A}}$. The area (5.14) can formally be extremized by evaluating the Euler-Lagrange equations. This can be simplified by observing that the integrand \mathcal{L} in (5.14) does not explicitly depend on x_1 , which gives the following integration constant

$$\text{const} = r' \frac{\partial \mathcal{L}}{\partial r'} - \mathcal{L} = \frac{e^{2A(r)} r'^2}{h(r) \sqrt{e^{2A(r)} + \frac{r'^2}{h(r)}}} - e^{2A(r)} \sqrt{e^{2A(r)} + \frac{r'^2}{h(r)}} = -e^{3A(r_*)}, \quad (5.15)$$

where we determined the integration constant at the point r_* , which is the closest position of the minimal surface to the horizon, such that

$$r(0) \equiv r_*, \quad r'(0) = 0, \quad r \left(\pm \frac{l}{2} \right) = \infty. \quad (5.16)$$

(In the right panel of Fig. 5.2, this would correspond to the turning point of the half cylinder.)

Equation (5.15) can be simplified to

$$\sqrt{e^{2A(r)} + \frac{r'^2}{h(r)}} = \frac{e^{4A(r)}}{e^{3A(r_*)}} \quad (5.17)$$

$$\iff r' = \sqrt{h(r) (e^{8A(r)-6A(r_*)} - e^{2A(r)})}. \quad (5.18)$$

With (5.18), the last boundary condition in Eq. (5.16) can now be reexpressed as

$$\frac{l}{2} = \int_0^{l/2} dx_1 = \int_{r_*}^{\infty} dr [h(r) (e^{8A(r)-6A(r_*)} - e^{2A(r)})]^{-1/2}. \quad (5.19)$$

Using Eq. (5.17) and (5.18), S_{HEE} follows from Eq. (5.14) as

$$S_{\text{HEE}} = \frac{V_2}{2} \int_0^{l/2} dx_1 \frac{e^{6A(r)}}{e^{3A(r_*)}} = \frac{V_2}{2} \int_{r_*}^{\infty} dr \frac{e^{6A(r)-3A(r_*)}}{e^{A(r)} \sqrt{h(r) (e^{6A(r)-6A(r_*)} - 1)}}. \quad (5.20)$$

As already mentioned above, this quantity is divergent in AdS space. One can also observe that the integrand in Eq. (5.20) contains only metric functions and therefore HEE indeed represents a non-local geometric quantity. In our computational setup, we only have numerical solutions of the metric functions from slightly outside the horizon to some finite value of the holographic coordinate r . We thus cannot perform a systematic regularization and renormalization procedure as e.g. in [121, 122] with an analytical expansion and suitable counterterms. As a first step, we therefore explore an ad-hoc regularized HEE density, which is defined as

$$S_{\text{HEE}}^{\text{reg}} := \frac{1}{2} \int_{r_*}^{r_m} dr \frac{e^{6A(r)-3A(r_*)}}{e^{A(r)} \sqrt{h(r) (e^{6A(r)-6A(r_*)} - 1)}}, \quad (5.21)$$

where r_m is a sufficiently large cutoff, similarly employed in the boundary condition (5.19).²⁶ Second, we perform a more rigorous renormalization procedure as follows: Let the integrand in Eq. (5.20) be denoted as $H(r)$ and define $\tilde{H}(r)$ by setting $A(r_*) \equiv 0$ in $H(r)$. Equations (4.15) and (4.16) show that $h(r)$ is constant for $r \rightarrow \infty$ at the boundary, while $A(r)$ is linear. The entanglement integrand $H(r)$ therefore goes asymptotically like $\exp\{2r/\sqrt{h_0^\infty}\}$ for large values of r . Although these series expansions are valid in the limit $r \rightarrow \infty$, the metric functions converge rapidly to the near-boundary behavior and thus $H(r)$ diverges generically as $1/\sqrt{r}$ for small values of r near the horizon. The newly defined function $\tilde{H}(r)$ obeys the same boundary asymptotics but is shifted such that it deviates near r_* compared to $H(r)$. It therefore picks up the same divergence at the cutoff r_m in the UV limit $r_m \rightarrow \infty$ and we consider the finite renormalized integrand $H(r) - \tilde{H}(r)$. Since the numerical values become very large and the difference is numerically demanding, we employ the logarithm and rewrite the integrand as $\ln H(r) - \ln \tilde{H}(r) = \ln[H(r)/\tilde{H}(r)]$. The renormalized HEE is now defined as

$$S_{\text{HEE}}^{\text{ren}} := \frac{1}{2} \int_{r_*}^{r_m} dr \ln \frac{H(r)}{\tilde{H}(r)}. \quad (5.22)$$

We remark that we introduced this renormalization scheme to avoid negative values of the HEE that appear for example in a renormalization procedure w.r.t. some reference point as in [119]. Since negative values for an entanglement entropy (as a von Neumann entropy for a subsystem) are not possible in the definition (5.1), we do not interpret these as physical.

Our final comment in this section is devoted to disconnected surfaces. In general, there could be also the possibility of a disconnected minimal entangling surface reaching from the boundary at $r = \infty$ up to the horizon at $r_* = r_H = 0$. However, as discussed in [123], extremal surfaces in static spacetimes cannot penetrate the event horizon of a BH. We therefore do not consider such a surface class in our analysis.

5.3 Phase diagram of holographic entanglement entropy

In this section we describe the numerical results of the HEE calculation in our holographic QCD phase diagram with the same initial conditions as in section 4.3. For each BH solution we solved the boundary condition (5.19) numerically for a fixed value $l = 0.04$ of the strip width and obtained the corresponding value of r_* . The regularized and renormalized HEE integrals (5.21) and (5.22) are then calculated with $r_m = 2.0$ as the UV regulator. We explicitly checked that the qualitative behavior is similar also for larger cutoff values.

In Fig. 5.3, $S_{\text{HEE}}^{\text{reg}}$ and $S_{\text{HEE}}^{\text{ren}}$ are shown in dependence on the temperature for different values of the chemical potential. At vanishing chemical potential, the regularized HEE (left panel)

²⁶The notion *density* refers to the fact that we divided by the infinite volume V_2 . This emulates the effect of an IR regulator.

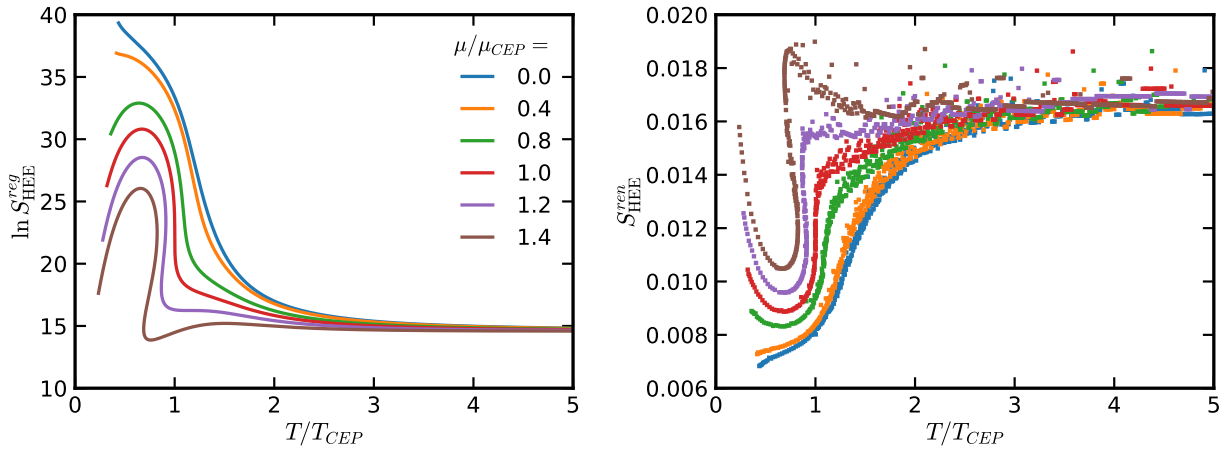


Figure 5.3: Regularized HEE density $\ln S_{\text{HEE}}^{\text{reg}}$ (left panel, figure source [2]) and renormalized HEE density $S_{\text{HEE}}^{\text{ren}}$ (right panel) as a function of the temperature T for different values of the chemical potential μ .

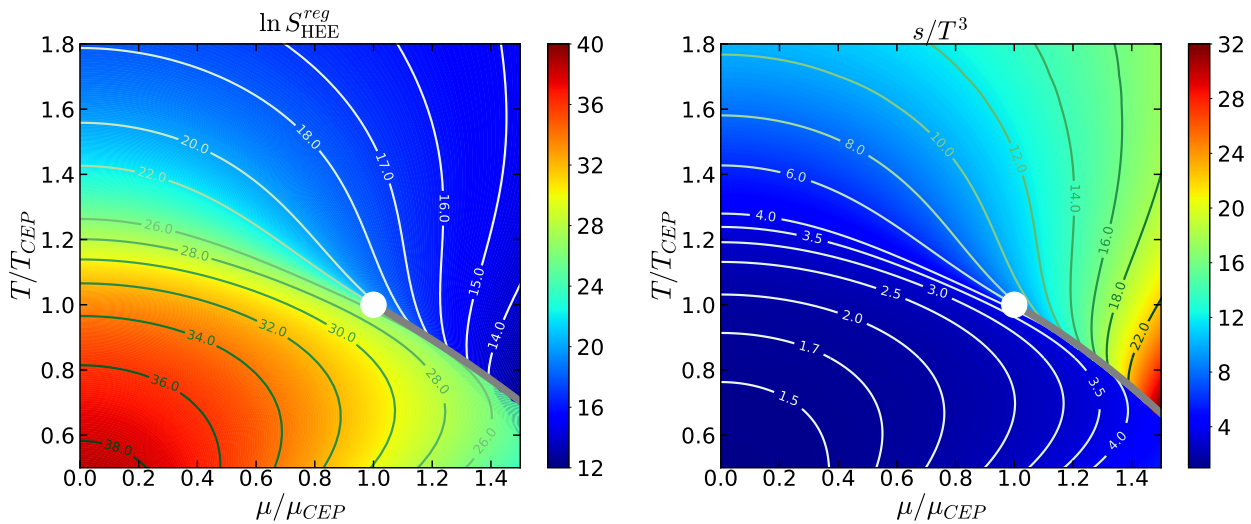


Figure 5.4: Contour plots of the regularized holographic entanglement entropy density $\ln S_{\text{HEE}}^{\text{reg}}$ (left) and scaled entropy density s/T^3 (right) over the scaled $T-\mu$ plane. The position of the CEPs is marked by a white dot and the FOPT curves are displayed as grey lines. Figure from [2].

is monotonically decreasing in the characteristic crossover region $T = \mathcal{O}(150 \text{ MeV})$. With increasing chemical potential, the HEE is pushed towards smaller values and a FOPT at large values of μ is signaled by the appearance of a multivalued branch. At the critical value $\mu \equiv \mu_{\text{CEP}}$, the entanglement entropy curve (red line in Fig. 5.3) has an infinite slope at $T \equiv T_{\text{CEP}}$, signalling the divergence at the CEP. The renormalized HEE (right panel) exhibits the opposite qualitative behavior, i.e. the values are monotonically increasing. A multivalued branch is analogously appearing for large $\mu \geq \mu_{\text{CEP}}$. Interestingly, the renormalized HEE resembles qualitatively well the shape of s/T^3 , c.f. Fig. 4.7. In [119], this was already observed for $\mu = 0$ in a different renormalization scheme. The calculations here show, that this is still

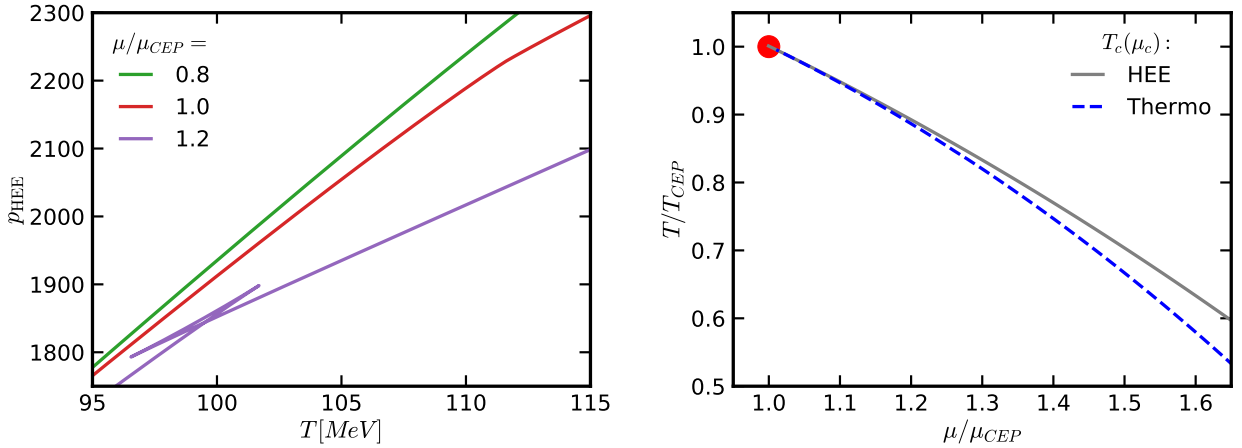


Figure 5.5: Left panel: Pseudo-pressure p_{HEE} in dependence on the temperature. The values follow from the regularized HEE definition by integrating $dp_{\text{HEE}} = \ln(S_{\text{HEE}}^{\text{reg}})dT$ for different values $\mu \equiv \text{const}$. Right panel: Comparison of FOPT curves over the scaled $T-\mu$ plane based on the left panel of Fig. 4.5 (grey curve) and the result exhibited in the right panel of Fig. 4.5 (blue dashed curve). The position of the CEP is marked by a red dot. Figure from [2].

true at finite μ . If one considers the dependence of the HEE on the width l , this agreement with the thermodynamic entropy would not be surprising for large l , since in that case the minimal surface is close to the BH horizon and the minimal area therefore is proportional to the area of the event horizon, i.e. the entropy according to the Bekenstein formula. However, in our case for fixed l but varying T , this agreement is a priori not obvious and nontrivial. In both definitions, the entanglement entropy at large temperatures T is nearly independent of μ and asymptotically constant. Remembering the fact that entanglement entropy characterizes the quantumness of a physical system, this shows that these holographically computed quantities can separate the quantum region of the holographic QCD phase diagram at low temperatures T from the thermodynamic region at large T and/or μ . From Fig. 5.3, it becomes obvious that the renormalized definition (5.22) is numerically more unstable compared to (5.21). We therefore continue to study the regularized HEE (5.21). We are confident that these results are robust since both definitions, although being rather ad-hoc, are clearly able to distinguish the phase structure and show the same features as outlined in the previous discussions.

To determine the phase structure in more detail, in particular the precise FOPT curve, we need to calculate the pressure as a thermodynamic potential. Regarding entanglement entropy, however, there is no first law of thermodynamics in general systems. Only for very special cases, an equivalent thermodynamic relation is known for excited states [124]. We therefore define a pseudo-pressure p_{HEE} through the integration

$$dp_{\text{HEE}} = \ln(S_{\text{HEE}}^{\text{reg}})dT \quad \text{for} \quad \mu \equiv \text{const}, \quad (5.23)$$

which is inspired by the first law of thermodynamics. The resulting dependence on the temper-

ature is shown in Fig. 5.5 (left panel). Note that a possible integration constant in this integral is irrelevant for the transition temperature. For $\mu < \mu_{CEP}$, p_{HEE} is monotonically increasing and starts to develop a kink at $\mu = \mu_{CEP}$, indicating the FOPT towards larger values of μ . In case of a FOPT at $\mu > \mu_{CEP}$, the pressure exhibits a typical loop, resulting from the multi-valued branch, and the temperature $T_c(\mu_c)$ of the FOPT is given by the intersection point of the low-temperature and high-temperature branches. We identify the stable phases as those with lowest pressure. This is contrary to standard thermodynamics, where stable phases have highest pressure, but represents an artefact of the regularized definition in which $S_{HEE}^{reg}(T)$ is decreasing (see left panel in Fig. 5.3). Since $S_{HEE}^{ren}(T)$ resembles the thermodynamic entropy and is increasing (see right panel in Fig. 5.3), this behavior would be opposite and similar to the thermodynamic interpretation in this case.

The resulting phase diagram of the regularized HEE density over the $T-\mu$ plane is shown in Fig. 5.4 (left panel) and compared to its counterpart, the standard thermodynamic-statistical entropy density s/T^3 (right panel). The CEP position $T_{CEP} = (111.5 \pm 0.5)$ MeV and $\mu_{CEP} = (611.5 \pm 0.5)$ MeV of the HEE phase diagram is in agreement with the thermodynamic result (4.48). Only the stable phases are shown. Across the FOPT curve, the HEE is discontinuous and jumps towards smaller values with increasing temperature or chemical potential. As already stressed above, this qualitative behavior of the regularized HEE density is opposite to the thermodynamic entropy. However, it is visible that the contour lines, i.e. “scaled isentropes”, show a remarkable similarity in both phase diagrams. This illustrates that HEE is indeed a quantity that is capable to characterize the different structures in the holographic QCD phase diagram.

Based on the HEE pseudo-pressure definition and the true thermodynamic stability criterion, we explicitly compare the location of the FOPT curves over the $T-\mu$ plane in Fig. 5.5 (right panel). In the vicinity of the critical point up to $\mu_c/\mu_{CEP} \approx 1.2$, the two curves agree very well but deviate from each other approximately 5% for $\mu_c/\mu_{CEP} \approx 1.6$. We remark that the definition of p_{HEE} in (5.23) with the logarithmic values $\ln S_{HEE}^{reg}$ is ad-hoc. This is justified by the fact that no exact first law for HEE exist. Furthermore, one can observe that this definition yields a better agreement of the resulting FOPT curve with the thermodynamic one than with the values S_{HEE}^{reg} itself.

5.4 Critical behavior

An important concept, which allows to describe the universal behavior of physical quantities near the critical point, are critical exponents. In general, they quantify the divergence of derivatives of the free energy as power laws. Here, we would like to use only the information from the HEE and thus consider the power law dependence of the specific heat at constant

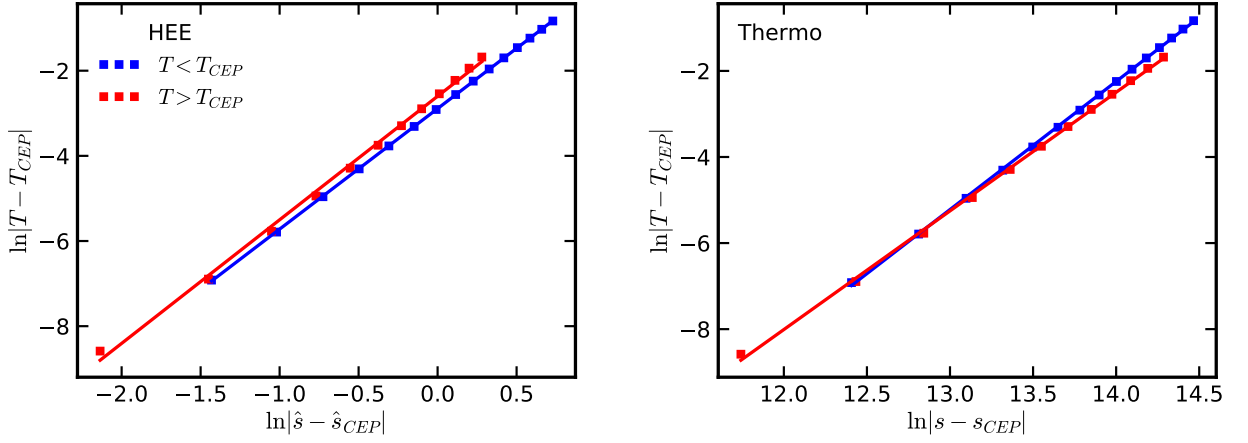


Figure 5.6: The logarithmic difference $\ln|T - T_{CEP}|$ in dependence on $\ln|s - s_{CEP}|$ for the regularized HEE density $\hat{s} \equiv \ln S_{\text{HEE}}^{\text{reg}}$ (left panel) and standard thermodynamic quantities (right panel). Blue dots are approaching the CEP along the $\mu \equiv \mu_{CEP}$ curve for $T < T_{CEP}$ and red dots for $T > T_{CEP}$. The straight lines represent the corresponding linear fit functions.

chemical potential:

$$C_\mu \equiv T \left. \frac{\partial \hat{s}}{\partial T} \right|_\mu = -T \left. \frac{\partial^2 f}{\partial T^2} \right|_\mu \sim |T - T_{CEP}|^{-\alpha}. \quad (5.24)$$

In this definition, the CEP is approached along $\mu = \mu_{CEP}$ and $T < T_{CEP}$. The exponent α' is defined similarly for $T > T_{CEP}$.²⁷

The calculation is performed as follows: We consider the proportionality $|T - T_{CEP}| \sim |\hat{s} - \hat{s}_{CEP}|^\beta$ and calculate the exponent β through the linear fit function $\ln|T - T_{CEP}| = \beta \ln|\hat{s} - \hat{s}_{CEP}| + \text{const}$ as shown in Fig. 5.6. From the definition (5.24), C_μ is proportional to $T/|T - T_{CEP}|^{1/\beta-1}$ and the critical exponent is then given by $\alpha = 1 - 1/\beta$.

We start with the thermodynamic entropy $\hat{s} \equiv s$ and find the following results for the BH solutions closest to the CEP (cf. right panel in Fig. 5.6):

$$\ln|T - T_{CEP}| = 2.9767 \ln|s - s_{CEP}| - 43.9173 \quad \text{for } T < T_{CEP}, \quad (5.25)$$

$$\ln|T - T_{CEP}| = 2.7568 \ln|s - s_{CEP}| - 41.0910 \quad \text{for } T > T_{CEP}. \quad (5.26)$$

The critical exponents then follow as

$$\alpha \approx 0.66, \quad \alpha' \approx 0.64. \quad (5.27)$$

Regarding the HEE, we employ the logarithmic values $\hat{s} \equiv \ln S_{\text{HEE}}^{\text{reg}}$ and find (cf. left panel in

²⁷In common notation, α is also used in the literature as the critical exponent for C_n , i.e. the heat capacity at constant baryon density along the FOPT curve. The latter has the mean field result $\alpha = \alpha' = 0$ and does not coincide with our definition here.

Fig. 5.6):

$$\ln |T - T_{CEP}| = 2.8309 \ln |\hat{s} - \hat{s}_{CEP}| - 2.8901 \quad \text{for } T < T_{CEP}, \quad (5.28)$$

$$\ln |T - T_{CEP}| = 2.9024 \ln |\hat{s} - \hat{s}_{CEP}| - 2.5998 \quad \text{for } T > T_{CEP}. \quad (5.29)$$

This procedure yields the following critical exponents:

$$\alpha_{\text{HEE}} \approx 0.65, \quad \alpha'_{\text{HEE}} \approx 0.66. \quad (5.30)$$

These values characterize the second-order phase transition at the CEP in the holographic QCD phase diagram. One can observe that in both cases, the results nearly give the same value $\alpha = \alpha' = 2/3$, which is the value for the van der Waals criticality in AdS black holes [125].

6 Summary and Outlook

In this thesis we have studied the QCD phase diagram within the framework of a holographic Einstein-Maxwell-dilaton (EMd) model. The model, originally proposed in [21], rests on a 5-dimensional classical gravitational theory in an anti-de Sitter (AdS) space coupled to a real dilaton scalar field with self-interaction (described by a nontrivial potential) and an Abelian gauge field (coupled to the dilaton with a dynamical strength function). The gravitational theory admits black hole solutions and, based on AdS/CFT interpretations, the associated thermodynamic quantities are related to a quantum field theory (QFT) at the four-dimensional boundary of the AdS space. The dilaton potential breaks conformal invariance and is responsible for mimicking the running coupling constant in QCD, while the Abelian gauge field introduces a chemical potential in the dual QFT.

We found multi-parameter ansätze for the dilaton potential and dynamical strength function that allow a very precise description of the most recent $2 + 1$ flavor lattice QCD data with physical quark masses at baryo-chemical potential $\mu = 0$ [11, 12, 70] (cf. section 4.2). In particular, we found appropriate dilaton potential parameters by a fit to the QCD equation of state (EoS) (cf. Fig. 4.1) and the parameters for the dynamical strength function were determined by a fit to the second-order quark number susceptibility (cf. Fig. 4.3). Based on this adjustment, we extrapolate the information of the holographic EMd model to finite density and chemical potential by suitably chosen initial conditions.

At this point, we should also emphasize the limitations of this bottom-up approach as an effective model to mimic selected QCD properties. Foremost, the model accounts only implicitly for fundamental aspects of QCD such as confinement and chiral symmetry by adjustment to lattice QCD results. Explicit considerations on chiral symmetry breaking and its restoration at finite temperature and density can only be done by taking flavored branes in the bulk into account, as in [126] (see [127–132] for further developments). The underlying setup here represent the simplest effective model with a minimal number of degrees of freedom (i.e. a single-dilaton potential). As discussed in [59], this kind of EMd model also does not take into account quantum string corrections or the strongly coupled UV fixed point in the classical gravitational theory. The setup is therefore limited to an intermediate temperature range above the quantum phase transition. However, since we are able to describe the second-order (which is input) and also fourth-order (which follows as a result) baryon susceptibilities at $\mu = 0$ of the lattice data, we are confident to make robust predictions for the QCD phase

diagram at finite values of μ .

Our realization of this EMD model (see section 4.3) results in a critical end point (CEP) at a temperature $T_{CEP} = (112 \pm 5)$ MeV and a baryo-chemical potential $\mu_{CEP} = (612 \pm 50)$ MeV as the starting point of a first-order phase transition (FOPT) curve towards larger chemical potential (cf. Fig. 4.5). The uncertainties of the CEP position follow from parameter variations and different low-temperature asymptotics for the second-order quark number susceptibility and EoS that take lattice uncertainties into account. This prediction is consistent with recent lattice estimates in [133] and the covered range of the phase diagram in [81]. The holographic QCD phase diagram in the $T - \mu$ plane is similar to a gas-liquid phase transition. This can be seen from the fact that the critical pressure as a function of the temperature is increasing (cf. Fig. 4.6) and the discontinuous jump of isentropes towards smaller values across the FOPT curve with increasing temperature and chemical potential (cf. Fig. 4.5). In particular, isentropes enter the coexistence region from the deconfined/dense side, run through and leave the FOPT curve on the confined/dilute side at lower temperature.

Recently, the authors of [134] calculated higher-order susceptibilities within the framework of this holographic EMD model to probe properties of the quark-gluon plasma (QGP) at finite density. Their adjustment to lattice QCD data is based on other parametrizations of the dilaton potential and dynamical strength function as well and results in a CEP with coordinates $T_{CEP} = (89 \pm 11)$ MeV and $\mu_{CEP} = (723 \pm 36)$ MeV, only marginally consistent with our result. In both works, the available lattice data (i.e. the EoS and susceptibilities) can be described equally good. We therefore conclude that the holographic EMD model is sensitive to the input data and internal parametrization, which, however, affect the CEP position and phase structure. In future studies, it would be promising to draw more profound conclusions and to find reasons for this behavior. For that purpose and an unique determination of CEP coordinates, precision lattice data in the range $T \lesssim 100$ MeV would be very helpful, since both setups seem to differ in this low-temperature region, where currently no lattice data are available.

In the second part of the thesis, we studied the entanglement entropy in our holographic QCD phase diagram (cf. chapter 5). Entanglement entropy is an important non-local quantity that allows to characterize phases in physical systems or can be used as an order parameter for phase transitions. Here, we calculate this quantity holographically (HEE) based on the proposal [54, 55] as a minimal surface in the bulk in the context of the AdS/CFT correspondence.

We assume a fixed strip shape as the entangling surface on the boundary and introduce a cutoff to regularize the divergent entropy integral to explore the phase structure in the temperature-chemical potential plane. In agreement with the thermodynamic result, a FOPT curve is setting in at the same CEP towards larger chemical potential (cf. section 5.2). We determine the FOPT curve in the entanglement setup by defining a pseudo-pressure as an integral over

the HEE density. In case of a FOPT, the HEE exhibits a multivalued branch and thus the pseudo-pressure allows to calculate the transition temperature. The resulting FOPT curves based on the HEE and from the thermodynamic calculation agree well in the vicinity of the CEP (cf. Fig. 5.5). We find that the HEE is capable to characterize the different structures in the QCD phase diagram (cf. Fig. 5.4): The regularized HEE density is decreasing rapidly in the crossover region of the phase diagram and jumps towards smaller values across the FOPT curve. This behavior is opposite to the thermodynamic entropy. Another ad-hoc definition of a renormalized HEE density, however, shows a similar behavior as the thermodynamic-statistical entropy density (cf. Fig. 5.3) and supports these general findings.

A detailed analysis of the criticality near the CEP shows that the logarithmic values of the regularized HEE density show a similar scaling behavior as the thermodynamic entropy density. In particular, we calculated the critical exponent of the heat capacity at constant chemical potential. The resulting values agree well with the van der Waals criticality in AdS black holes. Our results show that entanglement entropy qualifies to probe the hadronic phase and the QGP in our holographic EMD model. The confinement/deconfinement transition can be described (only) in the vicinity of the CEP of the QCD phase diagram and the qualitative behavior of HEE in the temperature-chemical potential plane is dependent on the regularization or renormalization scheme.

The significance of this thesis lies in a reliable discussion of expected structures in the QCD phase diagram within a holographic approach, which is based on a quantitative adjustment to the most recent lattice QCD results. Our prediction for the CEP is relevant for heavy-ion collision experiments in future facilities and our predictions for the phase structure at finite density and chemical potential could in principle be checked by advanced lattice QCD techniques that circumvent or solve the sign problem, which hampers up to now a direct lattice evaluation of thermodynamic quantities at non-zero chemical potential. Furthermore, we consider here for the first time the qualitative behavior of HEE in a holographic QCD phase diagram.

In future studies, it would be promising to adjust the model also at low temperatures to lattice QCD data, in particular in view of the aforementioned paper [134]. Furthermore, it might be interesting to incorporate effects like confinement and chirality explicitly in the holographic approach. Such effects, however, require a comprehensive extension of the current setup of the gravitational model and are not easy to implement. Regarding the HEE studies, improvements and more detailed studies for the renormalization procedure were desirable. In our current studies, these issues are limited by the numerical implementation. An extension of the present apparatus would allow to study the HEE in a self-consistent way.

A Details of the dilaton potential

In this appendix, we describe some details to motivate the explicit form

$$L^2V(\phi) = \begin{cases} -12 \exp \left\{ \frac{a_1}{2} \phi^2 + \frac{a_2}{4} \phi^4 \right\} & : \phi < \phi_m \\ a_{10} \cosh [a_4(\phi - a_5)]^{a_3/a_4} \exp \left\{ a_6 \phi + \frac{a_7}{a_8} \tanh [a_8(\phi - a_9)] \right\} & : \phi \geq \phi_m \end{cases} \quad (\text{A.1})$$

of the dilaton potential in our holographic model. These arguments are based on the results and discussions in [3].

The dilaton potential $V(\phi)$ is restricted by two conditions: The near-boundary expansion at $\phi \rightarrow 0$ is fixed by requiring an asymptotic AdS space as

$$\lim_{\phi \rightarrow 0} V(\phi) = -\frac{12}{L^2} + \frac{1}{2} m^2 \phi^2 + \dots, \quad (\text{A.2})$$

where the dilaton mass m is related to the scaling dimension Δ via $m^2 L^2 = \Delta(\Delta - 4)$. For the expansion of (A.1), this implies $\Delta = 2(1 + \sqrt{1 - 3a_1})$.²⁸ On the other side, near the black brane horizon at $\phi \rightarrow \infty$, the potential must obey the Chamblin-Reall behavior [135]

$$\lim_{\phi \rightarrow \infty} V(\phi) = V_0 e^{\gamma \phi} \quad (\text{A.3})$$

with $V_0 < 0$ and $\gamma = \text{const.}$ The form (A.1) was chosen to interpolate between these two behaviors (cf. blue curve in the left panel of Fig. A.1). However, these two conditions are not enough. A relevant quantity is also the ratio V'/V . (A prime denotes a derivative w.r.t. ϕ .) This is evident by considering v_s^2 , the speed of sound squared, as a quantity, which is sensitive to the phase transition type (cf. also [80]). Namely, in an adiabatic approximation, one has [76]

$$v_s^2 \approx \frac{1}{3} - \frac{1}{2} \left(\frac{V'}{V} \right)^2. \quad (\text{A.4})$$

A local minimum of v_s^2 as a characteristic feature of a crossover deconfinement phase transition (cf. Fig. 4.1) therefore corresponds to a local maximum of V'/V and vice versa. In addition, one can infer from Eq. (A.2) that V'/V must exhibit a polynomial behavior in the UV limit. (A possible divergent term in the series expansion around $\phi = 0$ is neglected since we always

²⁸This gives $\Delta \approx 2.7692$ or $m^2 L^2 \approx -3.4085 \geq -4$ for the fit parameters (4.39), satisfying the Breitenlohner-Freedman bound (3.28).

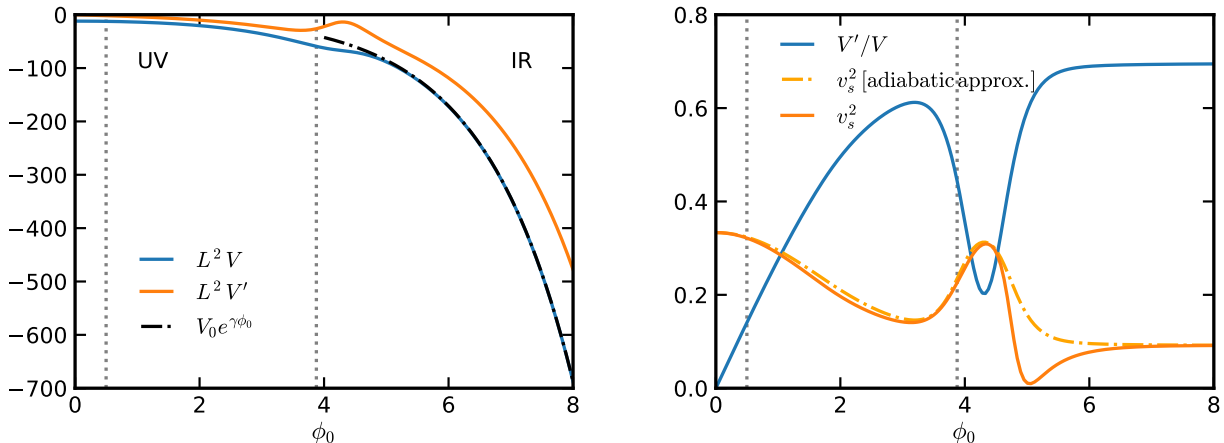


Figure A.1: Left panel: Dilaton potential L^2V (A.1) (blue curve) and its derivative L^2V' (orange curve) with coefficients (4.39) as a function of the initial conditions ϕ_0 . The asymptotic Chamblin-Reall potential is shown as black dash-dotted curve. Right panel: The ratio V'/V (blue curve) and speed of sound v_s^2 (orange curve) in dependence of ϕ_0 . The orange dash-dotted curve represents v_s^2 in the adiabatic approximation. Vertical dotted lines bracket the range of the lattice QCD data.

consider $\phi > 0$.) In the IR limit, Eq. (A.3) implies $V'/V = \text{const}$. Having these desired properties in mind, we make the following simple ansatz

$$v(\phi) := \frac{V'(\phi)}{V(\phi)} = \begin{cases} a_1\phi + a_2\phi^3 & : \phi < \phi_m \\ a_3 \tanh[a_4(\phi - a_5)] + a_6 + a_7 \text{sech}^2[a_8(\phi - a_9)] & : \phi \geq \phi_m \end{cases} \quad (\text{A.5})$$

which smoothly interpolates between the different regimes. The tanh term in (A.5) generates the asymptotic constant behavior, while the sech term generates a local maximum. Requiring regularity of v and v' at ϕ_m , one can solve for a_1 and a_2 (analytically). Upon integration, the dilaton potential (A.1) is derived, in which the integration constant a_{10} is determined by demanding regularity of V at ϕ_m . The right panel in Fig. A.1 shows v (blue curve) with best fit parameters (4.39) and v_s^2 (orange curve) in a large range of initial conditions ϕ_0 . The local maximum of v at $\phi_0 \approx 3.2$ corresponds to the local minimum of v_s^2 in the deconfinement crossover region. The adiabatic approximation (A.4) (orange dash-dotted curve) agrees quite accurately with the full result. The orange curve in the left panel of Fig. A.1 shows also V' separately. Allowing for a normalization, scaling and shift parameter for the tanh and sech term and an overall constant in (A.5), one has at least seven independent parameters to define $v(\phi)$ in the different regimes.²⁹ Together with ϕ_m , we allowed for eight free fit parameters. These parameters are adjusted in the range of available lattice data, which is enclosed by the vertical dotted lines in Fig. A.1. If the additional local minimum of v at $\phi_0 \approx 4.3$ is “justified” cannot

²⁹In more detail, a_3 and a_6 cause a vertical shift of $v(\phi)$, a_4 affects the height of the local maximum, a_5 determines the slope at $\phi \gtrsim \phi_m$, a_7 governs the depth of the “throat” at the local minimum, whose position is shifted by a_9 , and a_8 regulates its width.

be assessed, since it is beyond the fit range. From Eq. A.5, we deduce $\gamma \equiv \lim_{\phi \rightarrow \infty} v(\phi) = a_3 + a_6 \approx 0.6952$, demonstrating that $V(\phi)$ indeed obeys the Chamblin-Reall behavior (A.3) with $V_0 \approx -2.6405$ (cf. black dash-dotted curve in the left panel of Fig. A.1). As elaborated in [3] and [69], the thermodynamic requirement $p(\phi = \infty) = 0$ is satisfied for $\gamma < 2\sqrt{2/3} \approx 1.6330$, corresponding to a “good” singularity at $\phi \rightarrow \infty$. Considering v_s by taking the square root of Eq. A.4, one can deduce the more stringent condition $\gamma < \sqrt{2/3} \approx 0.8165$ by demanding thermodynamic stability (see also [76]). Both conditions are satisfied for the ansatz (A.5) with parameters (4.39) (cf. right panel in Fig. A.1). This exemplifies that the holographic model has no explicit confinement and fermionic degrees of freedom [69].

Bibliography

- [1] J. Knaute, R. Yaresko, and B. Kämpfer, *Holographic QCD phase diagram with critical point from Einstein-Maxwell-dilaton dynamics*, (2017), arXiv:1702.06731 [hep-ph]
- [2] J. Knaute and B. Kämpfer, *Holographic entanglement entropy in the QCD phase diagram with a critical point*, Phys. Rev. **D 96**, 106003 (2017), arXiv:1706.02647 [hep-ph]
- [3] R. Yaresko, J. Knaute, and B. Kämpfer, *Cross-over versus first-order phase transition in holographic gravity-single-dilaton models of QCD thermodynamics*, Eur. Phys. J. **C 75**, 295 (2015), arXiv:1503.09065 [hep-ph]
- [4] <http://www.fair-center.eu>
- [5] K. Adcox *et al.* (PHENIX), *Formation of dense partonic matter in relativistic nucleus-nucleus collisions at RHIC: Experimental evaluation by the PHENIX collaboration*, Nucl. Phys. **A 757**, 184 (2005), arXiv:nucl-ex/0410003 [nucl-ex]
- [6] J. Adams *et al.* (STAR), *Experimental and theoretical challenges in the search for the quark gluon plasma: The STAR Collaboration's critical assessment of the evidence from RHIC collisions*, Nucl. Phys. **A 757**, 102 (2005), arXiv:nucl-ex/0501009 [nucl-ex]
- [7] B. B. Back *et al.*, *The PHOBOS perspective on discoveries at RHIC*, Nucl. Phys. **A 757**, 28 (2005), arXiv:nucl-ex/0410022 [nucl-ex]
- [8] I. Arsene *et al.* (BRAHMS), *Quark-gluon plasma and color glass condensate at RHIC? The Perspective from the BRAHMS experiment*, Nucl. Phys. **A 757**, 1 (2005), arXiv:nucl-ex/0410020 [nucl-ex]
- [9] L. Adamczyk *et al.* (STAR), *Global Λ hyperon polarization in nuclear collisions*, Nature **548**, 62 (2017), arXiv:1701.06657 [nucl-ex]
- [10] Y. Aoki, G. Endrodi, Z. Fodor, S. D. Katz, and K. K. Szabo, *The order of the quantum chromodynamics transition predicted by the standard model of particle physics*, Nature **443**, 675 (2006), arXiv:hep-lat/0611014 [hep-lat]
- [11] S. Borsanyi, Z. Fodor, C. Hoelbling, S. D. Katz, S. Krieg, and K. K. Szabo, *Full result for the QCD equation of state with 2+1 flavors*, Phys. Lett. **B 730**, 99 (2014), arXiv:1309.5258 [hep-lat]
- [12] A. Bazavov *et al.* (HotQCD), *Equation of state in (2+1)-flavor QCD*, Phys. Rev. **D 90**, 094503 (2014), arXiv:1407.6387 [hep-lat]
- [13] G. 't Hooft, *A planar diagram theory for strong interactions*, Nucl. Phys. **B 72**, 461 (1974)
- [14] G. 't Hooft, *Dimensional Reduction in Quantum Gravity*, in *Salamfestschrift* (1993) pp. 284–296, arXiv:gr-qc/9310026 [gr-qc]

- [15] L. Susskind, *The world as a hologram*, J. Math. Phys. **36**, 6377 (1995), arXiv:hep-th/9409089 [hep-th]
- [16] J. D. Bekenstein, *Black Holes and Entropy*, Phys. Rev. D **7**, 2333 (1973)
- [17] J. M. Maldacena, *The Large- N Limit of Superconformal Field Theories and Supergravity*, Int. J. Theor. Phys. **38**, 1113 (1999), [Adv. Theor. Math. Phys. 2, 231 (1998)], arXiv:hep-th/9711200 [hep-th]
- [18] S. S. Gubser, I. R. Klebanov, and A. M. Polyakov, *Gauge theory correlators from non-critical string theory*, Phys. Lett. B **428**, 105 (1998), arXiv:hep-th/9802109 [hep-th]
- [19] E. Witten, *Anti de Sitter Space and Holography*, Adv. Theor. Math. Phys. **2**, 253 (1998), arXiv:hep-th/9802150 [hep-th]
- [20] P. Kovtun, D. T. Son, and A. O. Starinets, *Viscosity in Strongly Interacting Quantum Field Theories from Black Hole Physics*, Phys. Rev. Lett. **94**, 111601 (2005), arXiv:hep-th/0405231 [hep-th]
- [21] O. DeWolfe, S. S. Gubser, and C. Rosen, *A holographic critical point*, Phys. Rev. D **83**, 086005 (2011), arXiv:1012.1864 [hep-th]
- [22] S. Hawking, *Particle creation by black holes*, Commun. Math. Phys. **43**, 199 (1975)
- [23] B. Friman, C. Hohne, J. Knoll, S. Leupold, J. Randrup, R. Rapp, and P. Senger, *The CBM Physics Book: Compressed Baryonic Matter in Laboratory Experiments*, Lect. Notes Phys. **814**, 1 (2011)
- [24] P. Braun-Munzinger, V. Koch, T. Schäfer, and J. Stachel, *Properties of hot and dense matter from relativistic heavy ion collisions*, Phys. Rept. **621**, 76 (2016), arXiv:1510.00442 [nucl-th]
- [25] K. Yagi, T. Hatsuda, and Y. Miake, *Quark-Gluon Plasma: From Big Bang to Little Bang*, Camb. Monogr. Part. Phys. Nucl. Phys. Cosmol. **23** (2005)
- [26] S. Sarkar, H. Satz, and B. Sinha, *The Physics of the Quark-Gluon Plasma*, Lect. Notes Phys. **785**, 1 (2010)
- [27] C. Patrignani *et al.* (Particle Data Group), *Review of Particle Physics*, Chin. Phys. C **40**, 100001 (2016)
- [28] D. H. Rischke, *The quark-gluon plasma in equilibrium*, Prog. Part. Nucl. Phys. **52**, 197 (2004), arXiv:nucl-th/0305030 [nucl-th]
- [29] H.-T. Ding, F. Karsch, and S. Mukherjee, *Thermodynamics of strong-interaction matter from lattice QCD*, Int. J. Mod. Phys. E **24**, 1530007 (2015), arXiv:1504.05274 [hep-lat]
- [30] C. Gattringer and C. B. Lang, *Quantum Chromodynamics on the Lattice*, Lect. Notes Phys. **788**, 1 (2010)
- [31] C. Bonati, P. de Forcrand, M. D'Elia, O. Philipsen, and F. Sanfilippo, *Constraints on the two-flavor QCD phase diagram from imaginary chemical potential*, PoS LATTICE2011, 189 (2011), arXiv:1201.2769 [hep-lat]
- [32] N. Cabibbo and G. Parisi, *Exponential hadronic spectrum and quark liberation*, Phys. Lett. B **59**, 67 (1975)
- [33] F. R. Brown, F. P. Butler, H. Chen, N. H. Christ, Z. Dong, W. Schaffer, L. I. Unger, and A. Vaccarino, *On the existence of a phase transition for QCD with three light quarks*, Phys. Rev. Lett. **65**, 2491 (1990)

-
- [34] F. Cuteri, C. Czaban, O. Philipsen, and A. Sciarra, *Updates on the Columbia plot and its extended/alternative versions*, (2017), arXiv:1710.09304 [hep-lat]
- [35] X. Luo and N. Xu, *Search for the QCD critical point with fluctuations of conserved quantities in relativistic heavy-ion collisions at RHIC: an overview*, Nucl. Sci. Tech. **28**, 112 (2017), arXiv:1701.02105 [nucl-ex]
- [36] W. Florkowski, M. P. Heller, and M. Spalinski, *New theories of relativistic hydrodynamics in the LHC era*, (2017), arXiv:1707.02282 [hep-ph]
- [37] J. Casalderrey-Solana, H. Liu, D. Mateos, K. Rajagopal, and U. A. Wiedemann, *Gauge/String Duality, Hot QCD and Heavy Ion Collisions* (Cambridge University Press, 2014)
- [38] P. M. Chesler and L. G. Yaffe, *Boost invariant flow, black hole formation, and far-from-equilibrium dynamics in $\mathcal{N} = 4$ supersymmetric Yang-Mills theory*, Phys. Rev. D **82**, 026006 (2010), arXiv:0906.4426 [hep-th]
- [39] M. P. Heller, R. A. Janik, and P. Witaszczyk, *Characteristics of Thermalization of Boost-Invariant Plasma from Holography*, Phys. Rev. Lett. **108**, 201602 (2012), arXiv:1103.3452 [hep-th]
- [40] M. Attems, J. Casalderrey-Solana, D. Mateos, D. Santos-Oliván, C. F. Sopuerta, M. Triana, and M. Zilhão, *Paths to equilibrium in non-conformal collisions*, JHEP **06**, 154 (2017), arXiv:1703.09681 [hep-th]
- [41] P. Romatschke, *Far From Equilibrium Fluid Dynamics*, (2017), arXiv:1704.08699 [hep-th]
- [42] R. Critelli, R. Rougemont, and J. Noronha, *Homogeneous isotropization and equilibration of a strongly coupled plasma with a critical point*, (2017), arXiv:1709.03131 [hep-th]
- [43] M. Ammon and J. Erdmenger, *Gauge/Gravity Duality* (Cambridge University Press, 2015)
- [44] H. Nastase, *Introduction to the AdS/CFT Correspondence* (Cambridge University Press, 2015)
- [45] M. Natsuume, *AdS/CFT Duality User Guide*, Lect. Notes Phys. **903**, 1 (2015), arXiv:1409.3575 [hep-th]
- [46] E. Papantonopoulos, *From Gravity to Thermal Gauge Theories: The AdS/CFT Correspondence*, Lect. Notes Phys. **828**, 1 (2011)
- [47] K. Becker, M. Becker, and J. Schwarz, *String Theory and M-Theory: A Modern Introduction* (Cambridge University Press, 2007)
- [48] J. Polchinski, *String theory. Vol. 1: An introduction to the bosonic string* (Cambridge University Press, 2005)
- [49] J. Polchinski, *String theory. Vol. 2: Superstring theory and beyond* (Cambridge University Press, 2005)
- [50] E. D'Hoker and D. Z. Freedman, *Supersymmetric Gauge Theories and the AdS/CFT Correspondence*, (2002), arXiv:hep-th/0201253 [hep-th]
- [51] J. Polchinski, *Dirichlet Branes and Ramond-Ramond Charges*, Phys. Rev. Lett. **75**, 4724 (1995), arXiv:hep-th/9510017 [hep-th]

-
- [52] A. W. Samberg, *Applied String Theory, Hot and Cold: A Holographic View on Quark-Gluon Plasma and Superfluids*, Ph.D. thesis, Universität Heidelberg (2016)
- [53] O. Aharony, S. S. Gubser, J. M. Maldacena, H. Ooguri, and Y. Oz, *Large N field theories, string theory and gravity*, Phys. Rept. **323**, 183 (2000), arXiv:hep-th/9905111 [hep-th]
- [54] S. Ryu and T. Takayanagi, *Holographic Derivation of Entanglement Entropy from the anti-de Sitter Space/Conformal Field Theory Correspondence*, Phys. Rev. Lett. **96**, 181602 (2006), arXiv:hep-th/0603001 [hep-th]
- [55] S. Ryu and T. Takayanagi, *Aspects of holographic entanglement entropy*, JHEP **08**, 045 (2006), arXiv:hep-th/0605073 [hep-th]
- [56] M. Van Raamsdonk, *Building up spacetime with quantum entanglement*, Gen. Rel. Grav. **42**, 2323 (2010), [Int. J. Mod. Phys. D **19**, 2429 (2010)], arXiv:1005.3035 [hep-th]
- [57] B. Swingle and M. Van Raamsdonk, *Universality of Gravity from Entanglement*, (2014), arXiv:1405.2933 [hep-th]
- [58] O. DeWolfe, S. S. Gubser, and C. Rosen, *Dynamic critical phenomena at a holographic critical point*, Phys. Rev. **D 84**, 126014 (2011), arXiv:1108.2029 [hep-th]
- [59] R. Rougemont, A. Ficnar, S. Finazzo, and J. Noronha, *Energy loss, equilibration, and thermodynamics of a baryon rich strongly coupled quark-gluon plasma*, JHEP **04**, 102 (2016), arXiv:1507.06556 [hep-th]
- [60] R. Rougemont, J. Noronha, and J. Noronha-Hostler, *Suppression of Baryon Diffusion and Transport in a Baryon Rich Strongly Coupled Quark-Gluon Plasma*, Phys. Rev. Lett. **115**, 202301 (2015), arXiv:1507.06972 [hep-ph]
- [61] R. Rougemont, R. Critelli, J. Noronha-Hostler, J. Noronha, and C. Ratti, *Dynamical versus equilibrium properties of the QCD phase transition: A holographic perspective*, Phys. Rev. **D 96**, 014032 (2017), arXiv:1704.05558 [hep-ph]
- [62] R.-G. Cai, S. He, and D. Li, *A h QCD model and its phase diagram in Einstein-Maxwell-Dilaton system*, JHEP **03**, 033 (2012), arXiv:1201.0820 [hep-th]
- [63] S. He, S.-Y. Wu, Y. Yang, and P.-H. Yuan, *Phase structure in a dynamical soft-wall holographic QCD model*, JHEP **04**, 093 (2013), arXiv:1301.0385 [hep-th]
- [64] Y. Yang and P.-H. Yuan, *A refined holographic QCD model and QCD phase structure*, JHEP **11**, 149 (2014), arXiv:1406.1865 [hep-th]
- [65] C. Ewerz, O. Kaczmarek, and A. Samberg, *Free Energy of a Heavy Quark-Antiquark Pair in a Thermal Medium from AdS/CFT*, (2016), arXiv:1605.07181 [hep-th]
- [66] M.-W. Li, Y. Yang, and P.-H. Yuan, *Approaching confinement structure for light quarks in a holographic soft wall QCD model*, Phys. Rev. **D 96**, 066013 (2017), arXiv:1703.09184 [hep-th]
- [67] Z. Li, Y. Chen, D. Li, and M. Huang, *Locating the QCD critical end point through the peaked baryon number susceptibilities along the freeze-out line*, (2017), arXiv:1706.02238 [hep-ph]

-
- [68] R. A. J. Critelli, *Strongly coupled non-Abelian plasmas in a magnetic field*, Master thesis, University of São Paulo (2016), arXiv:1609.03104 [hep-ph]
- [69] U. Gürsoy, E. Kiritsis, L. Mazzanti, and F. Nitti, *Holography and thermodynamics of 5D dilaton-gravity*, JHEP **05**, 033 (2009), arXiv:0812.0792 [hep-th]
- [70] R. Bellwied, S. Borsanyi, Z. Fodor, S. D. Katz, A. Pasztor, C. Ratti, and K. K. Szabo, *Fluctuations and correlations in high temperature QCD*, Phys. Rev. **D 92**, 114505 (2015), arXiv:1507.04627 [hep-lat]
- [71] R. Yaresko and B. Kämpfer, *Equation of state and viscosities from a gravity dual of the gluon plasma*, Phys. Lett. **B 747**, 36 (2015), arXiv:1306.0214 [hep-ph]
- [72] J. Knaute, *Holographic description of the equation of state of the quark-gluon plasma*, Bachelor thesis, Technische Universität Dresden (2014)
- [73] C. Csáki and M. Reece, *Toward a systematic holographic QCD: a braneless approach*, JHEP **05**, 062 (2007), arXiv:hep-ph/0608266 [hep-ph]
- [74] U. Gürsoy and E. Kiritsis, *Exploring improved holographic theories for QCD: part I*, JHEP **02**, 032 (2008), arXiv:0707.1324 [hep-th]
- [75] U. Gürsoy, E. Kiritsis, and F. Nitti, *Exploring improved holographic theories for QCD: part II*, JHEP **02**, 019 (2008), arXiv:0707.1349 [hep-th]
- [76] S. S. Gubser and A. Nellore, *Mimicking the QCD equation of state with a dual black hole*, Phys. Rev. **D 78**, 086007 (2008), arXiv:0804.0434 [hep-th]
- [77] U. Gürsoy, E. Kiritsis, L. Mazzanti, and F. Nitti, *Improved holographic Yang-Mills at finite temperature: Comparison with data*, Nucl. Phys. **B 820**, 148 (2009), arXiv:0903.2859 [hep-th]
- [78] F. Wunderlich, R. Yaresko, and B. Kämpfer, *Arguing on Entropic and Enthalpic First-Order Phase Transitions in Strongly Interacting Matter*, J. Mod. Phys. **7**, 852 (2016), arXiv:1604.00179 [hep-ph]
- [79] S. Borsanyi, G. Endrodi, Z. Fodor, S. D. Katz, S. Krieg, C. Ratti, and K. K. Szabo, *QCD equation of state at nonzero chemical potential: continuum results with physical quark masses at order μ^2* , JHEP **08**, 053 (2012), arXiv:1204.6710 [hep-lat]
- [80] R. Zöllner and B. Kämpfer, *Extended soft wall model with background related to features of QCD thermodynamics*, Eur. Phys. J. **A 53**, 139 (2017), arXiv:1701.01398 [hep-ph]
- [81] J. Günther, R. Bellwied, S. Borsanyi, Z. Fodor, S. D. Katz, A. Pasztor, and C. Ratti, *The QCD equation of state at finite density from analytical continuation*, EPJ Web Conf. **137**, 07008 (2017), arXiv:1607.02493 [hep-lat]
- [82] T. Nishioka, S. Ryu, and T. Takayanagi, *Holographic entanglement entropy: an overview*, J. Phys. **A 42**, 504008 (2009), arXiv:0905.0932 [hep-th]
- [83] M. Rangamani and T. Takayanagi, *Holographic Entanglement Entropy*, Lect. Notes Phys. **931**, 1 (2017), arXiv:1609.01287 [hep-th]
- [84] T. Takayanagi, *Recent Developments in (Holographic) Entanglement Entropy*, Talk presented at the International Symposium Ahrenschoop on the Theory of Elementary Particles “Recent Developments in String and Field Theory” (2012)

-
- [85] H. Terashima, *Entanglement entropy of the black hole horizon*, Phys. Rev. **D 61**, 104016 (2000), arXiv:gr-qc/9911091 [gr-qc]
- [86] G. Vidal, J. I. Latorre, E. Rico, and A. Kitaev, *Entanglement in Quantum Critical Phenomena*, Phys. Rev. Lett. **90**, 227902 (2003), arXiv:quant-ph/0211074 [quant-ph]
- [87] P. Calabrese and J. L. Cardy, *Entanglement entropy and quantum field theory*, J. Stat. Mech. **0406**, P06002 (2004), arXiv:hep-th/0405152 [hep-th]
- [88] R. O. Orus Lacort, *Entanglement, quantum phase transitions and quantum algorithms*, Ph.D. thesis, Barcelona University (2006), arXiv:quant-ph/0608013 [quant-ph]
- [89] P. Calabrese and J. Cardy, *Entanglement entropy and conformal field theory*, J. Phys. **A 42**, 504005 (2009), arXiv:0905.4013 [cond-mat.stat-mech]
- [90] C. Rovelli and M. Smerlak, *Unruh effect without trans-horizon entanglement*, Phys. Rev. **D 85**, 124055 (2012), arXiv:1108.0320 [gr-qc]
- [91] N. Laflorencie, *Quantum entanglement in condensed matter systems*, Phys. Rept. **646**, 1 (2016), arXiv:1512.03388 [cond-mat.str-el]
- [92] P. Chaturvedi, V. Malvimat, and G. Sengupta, *Entanglement thermodynamics for charged black holes*, Phys. Rev. **D 94**, 066004 (2016), arXiv:1601.00303 [hep-th]
- [93] H.-L. Li, S.-Z. Yang, and X.-T. Zu, *Holographic research on phase transitions for a five dimensional AdS black hole with conformally coupled scalar hair*, Phys. Lett. **B 764**, 310 (2017)
- [94] X.-X. Zeng and L.-F. Li, *Holographic Phase Transition Probed by Nonlocal Observables*, Adv. High Energy Phys. **2016**, 1 (2016), arXiv:1609.06535 [hep-th]
- [95] X.-X. Zeng, H. Zhang, and L.-F. Li, *Phase transition of holographic entanglement entropy in massive gravity*, Phys. Lett. **B 756**, 170 (2016), arXiv:1511.00383 [gr-qc]
- [96] A. Dey, S. Mahapatra, and T. Sarkar, *Thermodynamics and entanglement entropy with Weyl corrections*, Phys. Rev. **D 94**, 026006 (2016), arXiv:1512.07117 [hep-th]
- [97] E. Caceres and A. Kundu, *Holographic thermalization with chemical potential*, JHEP **09**, 055 (2012), arXiv:1205.2354 [hep-th]
- [98] D. S. Ageev and I. Ya. Aref'eva, *Memory Loss in Holographic Non-equilibrium Heating*, (2017), arXiv:1704.07747 [hep-th]
- [99] T. Takayanagi, *Entanglement entropy and gravity/condensed matter correspondence*, Gen. Rel. Grav. **46**, 1693 (2014)
- [100] T. Albash and C. V. Johnson, *Holographic studies of entanglement entropy in superconductors*, JHEP **05**, 079 (2012), arXiv:1202.2605 [hep-th]
- [101] R.-G. Cai, S. He, L. Li, and Y.-L. Zhang, *Holographic entanglement entropy in insulator/superconductor transition*, JHEP **07**, 088 (2012), arXiv:1203.6620 [hep-th]
- [102] R.-G. Cai, S. He, L. Li, and Y.-L. Zhang, *Holographic entanglement entropy in P-wave superconductor phase transition*, JHEP **07**, 027 (2012), arXiv:1204.5962 [hep-th]

-
- [103] C. V. Johnson, *Large N phase transitions, finite volume, and entanglement entropy*, JHEP **03**, 047 (2014), arXiv:1306.4955 [hep-th]
- [104] A. Dey, S. Mahapatra, and T. Sarkar, *Very general holographic superconductors and entanglement thermodynamics*, JHEP **12**, 135 (2014), arXiv:1409.5309 [hep-th]
- [105] M. K. Zangeneh, Y. C. Ong, and B. Wang, *Entanglement entropy and complexity for one-dimensional holographic superconductors*, Phys. Lett. **B 771**, 235 (2017), arXiv:1704.00557 [hep-th]
- [106] Y. Ling, P. Liu, C. Niu, J.-P. Wu, and Z.-Y. Xian, *Holographic entanglement entropy close to quantum phase transitions*, JHEP **04**, 114 (2016), arXiv:1502.03661 [hep-th]
- [107] Y. Ling, P. Liu, and J.-P. Wu, *Characterization of quantum phase transition using holographic entanglement entropy*, Phys. Rev. **D 93**, 126004 (2016), arXiv:1604.04857 [hep-th]
- [108] Y. Ling, P. Liu, J.-P. Wu, and Z. Zhou, *Holographic metal-insulator transition in higher derivative gravity*, Phys. Lett. **B 766**, 41 (2017), arXiv:1606.07866 [hep-th]
- [109] K. Li, M. Han, G. Long, Y. Wan, D. Lu, B. Zeng, and R. Laflamme, *Measuring Holographic Entanglement Entropy on a Quantum Simulator*, (2017), arXiv:1705.00365 [quant-ph]
- [110] I. R. Klebanov, D. Kutasov, and A. Murugan, *Entanglement as a probe of confinement*, Nucl. Phys. **B 796**, 274 (2008), arXiv:0709.2140 [hep-th]
- [111] A. Lewkowycz, *Holographic entanglement entropy and confinement*, JHEP **05**, 032 (2012), arXiv:1204.0588 [hep-th]
- [112] N. Kim, *Holographic entanglement entropy of confining gauge theories with flavor*, Phys. Lett. **B 720**, 232 (2013)
- [113] U. Kol, C. Núñez, D. Schofield, J. Sonnenschein, and M. Warschawski, *Confinement, phase transitions and non-locality in the entanglement entropy*, JHEP **06**, 005 (2014), arXiv:1403.2721 [hep-th]
- [114] M. Ghodrati, *Schwinger effect and entanglement entropy in confining geometries*, Phys. Rev. **D 92**, 065015 (2015), arXiv:1506.08557 [hep-th]
- [115] D. Dudal and S. Mahapatra, *Confining gauge theories and holographic entanglement entropy with a magnetic field*, JHEP **04**, 031 (2017), arXiv:1612.06248 [hep-th]
- [116] A. Velytsky, *Entanglement entropy in $d+1$ $SU(N)$ gauge theory*, Phys. Rev. **D 77**, 085021 (2008), arXiv:0801.4111 [hep-th]
- [117] P. V. Buividovich and M. I. Polikarpov, *Numerical study of entanglement entropy in $SU(2)$ lattice gauge theory*, Nucl. Phys. **B 802**, 458 (2008), arXiv:0802.4247 [hep-lat]
- [118] E. Itou, K. Nagata, Y. Nakagawa, A. Nakamura, and V. I. Zakharov, *Entanglement in four-dimensional $SU(3)$ gauge theory*, PTEP **2016**, 061B01 (2016), arXiv:1512.01334 [hep-th]
- [119] S.-J. Zhang, *Holographic entanglement entropy close to crossover/phase transition in strongly coupled systems*, Nucl. Phys. **B 916**, 304 (2017), arXiv:1608.03072 [hep-th]

-
- [120] S. S. Gubser, A. Nellore, S. S. Pufu, and F. D. Rocha, *Thermodynamics and Bulk Viscosity of Approximate Black Hole Duals to Finite Temperature Quantum Chromodynamics*, Phys. Rev. Lett. **101**, 131601 (2008), arXiv:0804.1950 [hep-th]
- [121] M. Taylor and W. Woodhead, *Renormalized entanglement entropy*, JHEP **08**, 165 (2016), arXiv:1604.06808 [hep-th]
- [122] M. Taylor and W. Woodhead, *Non-conformal entanglement entropy*, (2017), arXiv:1704.08269 [hep-th]
- [123] V. E. Hubeny, *Extremal surfaces as bulk probes in AdS/CFT*, JHEP **07**, 093 (2012), arXiv:1203.1044 [hep-th]
- [124] J. Bhattacharya, M. Nozaki, T. Takayanagi, and T. Ugajin, *Thermodynamical Property of Entanglement Entropy for Excited States*, Phys. Rev. Lett. **110**, 091602 (2013), arXiv:1212.1164 [hep-th]
- [125] K. Bhattacharya, B. R. Majhi, and S. Samanta, *van der Waals criticality in AdS black holes: A phenomenological study*, Phys. Rev. D **96**, 084037 (2017), arXiv:1709.02650 [gr-qc]
- [126] M. Järvinen and E. Kiritsis, *Holographic models for QCD in the Veneziano limit*, JHEP **03**, 002 (2012), arXiv:1112.1261 [hep-ph]
- [127] T. Alho, M. Järvinen, K. Kajantie, E. Kiritsis, and K. Tuominen, *On finite-temperature holographic QCD in the Veneziano limit*, JHEP **01**, 093 (2013), arXiv:1210.4516 [hep-ph]
- [128] D. Areán, I. Iatrakis, M. Järvinen, and E. Kiritsis, *The discontinuities of conformal transitions and mass spectra of V-QCD*, JHEP **11**, 068 (2013), arXiv:1309.2286 [hep-ph]
- [129] T. Alho, M. Järvinen, K. Kajantie, E. Kiritsis, C. Rosen, and K. Tuominen, *A holographic model for QCD in the Veneziano limit at finite temperature and density*, JHEP **04**, 124 (2014), [Erratum: JHEP 02, 033 (2015)], arXiv:1312.5199 [hep-ph]
- [130] M. Järvinen, *Massive holographic QCD in the Veneziano limit*, JHEP **07**, 033 (2015), arXiv:1501.07272 [hep-ph]
- [131] U. Gürsoy, I. Iatrakis, M. Järvinen, and G. Nijs, *Inverse magnetic catalysis from improved holographic QCD in the Veneziano limit*, JHEP **03**, 053 (2017), arXiv:1611.06339 [hep-th]
- [132] U. Gürsoy, M. Järvinen, and G. Nijs, *Holographic QCD in the Veneziano limit at finite Magnetic Field and Chemical Potential*, (2017), arXiv:1707.00872 [hep-th]
- [133] A. Bazavov *et al.*, *QCD equation of state to $\mathcal{O}(\mu_B^6)$ from lattice QCD*, Phys. Rev. D **95**, 054504 (2017), arXiv:1701.04325 [hep-lat]
- [134] R. Critelli, J. Noronha, J. Noronha-Hostler, I. Portillo, C. Ratti, and R. Rougemont, *Critical point in the phase diagram of primordial quark-gluon matter from black hole physics*, Phys. Rev. D **96**, 096026 (2017), arXiv:1706.00455 [nucl-th]
- [135] H. A. Chamblin and H. S. Reall, *Dynamic dilatonic domain walls*, Nucl. Phys. B **562**, 133 (1999), arXiv:hep-th/9903225 [hep-th]

Acknowledgements

First and foremost I offer my sincerest gratitude to my supervisor, Prof. Dr. Burkhard Kämpfer, who has supported me throughout my thesis with his patience and knowledge. The author is also grateful to Prof. Dr. Dominik Stöckinger for the preparation of the second opinion. I thank Roman Yaresko[†] for collaboration in the early stage of this project. Discussions with Dr. Michal Heller, Rico Zöllner and Andreas Otto are gratefully acknowledged.

Erklärung

Hiermit erkläre ich, dass ich diese Arbeit im Rahmen der Betreuung am Institut für Theoretische Physik ohne unzulässige Hilfe Dritter verfasst und alle Quellen als solche gekennzeichnet habe.

Johannes Knaute

Dresden, Dezember 2017